
Electronic Thesis and Dissertation Repository

2-16-2021 3:00 PM

High-Pressure Studies of Flexible Metal-Organic Frameworks and Their Performance for CO₂ Adsorption using Infrared Spectroscopy

Boqing Li, *The University of Western Ontario*

Supervisor: Yining Huang, *The University of Western Ontario*

Joint Supervisor: Yang Song, *The University of Western Ontario*

A thesis submitted in partial fulfillment of the requirements for the Master of Science degree in Chemistry

© Boqing Li 2021

Follow this and additional works at: <https://ir.lib.uwo.ca/etd>

 Part of the [Analytical Chemistry Commons](#)

Recommended Citation

Li, Boqing, "High-Pressure Studies of Flexible Metal-Organic Frameworks and Their Performance for CO₂ Adsorption using Infrared Spectroscopy" (2021). *Electronic Thesis and Dissertation Repository*. 7665. <https://ir.lib.uwo.ca/etd/7665>

This Dissertation/Thesis is brought to you for free and open access by Scholarship@Western. It has been accepted for inclusion in Electronic Thesis and Dissertation Repository by an authorized administrator of Scholarship@Western. For more information, please contact wlsadmin@uwo.ca.

Abstract

Metal-organic frameworks (MOFs) are crystalline porous materials comprising metal ions/clusters and organic linkers. MOFs feature very large surface area and broad tunability, which distinguish them from traditional CO₂ adsorbents. High external pressure can significantly modify the framework structures and CO₂ adsorption properties of MOFs. MIL-53(Al) and NH₂-MIL-53(Al) exhibit excellent CO₂ affinity by forming hydrogen bonds between bridging OH groups and adsorbed CO₂. We used *in situ* infrared spectroscopy to investigate the high-pressure performance of their framework structures and CO₂ adsorption capacities. Diamond anvil cell was employed to apply high pressures in gigapascal level.

For as-made MIL-53(Al), pressures-induced inter-framework hydrogen bonds between OH groups and free H₂BDC molecules were observed. The IR spectra of activated MIL-53(Al) upon compression provided direct evidence of its extraordinary stability compared to as-made and CO₂-loaded MIL-53(Al). Pressure-induced intra-framework hydrogen bonding interactions between OH groups and octahedral [AlO₆] were observed in activated MIL-53(Al). Moreover, structural modifications of as-made and activated MIL-53(Al) were irreversible upon complete decompression. Pressure-enhanced CO₂ adsorption in MIL-53(Al) was demonstrated. Upon complete decompression, considerable CO₂ molecules remained in the framework. Activated NH₂-MIL-53(Al) exhibited reversible pressure-enhanced intra-framework interactions via two types of hydrogen bonding: one was between -NH₂ groups and octahedral [AlO₆], the other was between OH groups and octahedral [AlO₆]. For CO₂-loaded NH₂-MIL-53(Al), there were four different high-pressure adsorption sites co-existing upon compression: dimeric adsorption, large-pore adsorption, narrow-pore adsorption, and amino adsorption. We demonstrated that high pressures made the narrow-pore adsorption highly favored over the other three.

Keywords

Metal-organic frameworks, high pressure, infrared spectroscopy, diamond anvil cell, framework stability, pressure-induced phase transition, guest-host interaction, pressure-induced CO₂ adsorption, CO₂ adsorption form.

Summary for Lay Audience

As a rising class of porous crystalline materials, metal-organic frameworks (MOFs) are composed of metal centers connected through organic linkers to create open frameworks with channels or cages. MOFs have been well-studied as one of the most promising adsorbents for CO₂ capture, owing to their porous structure and high surface area. The framework structures and gas adsorption properties of MOFs could be altered vastly upon compression. Pressure-induced phase transitions, intra-framework and guest-host interactions are the most common phenomena of MOFs under high pressure. Previous studies have demonstrated that high external pressure can enhance CO₂ adsorption in many MOFs. This thesis focuses on two well-studied MOFs with excellent CO₂ affinity. Diamond anvil cell was employed to apply high pressures in gigapascal level on MIL-53(Al) and NH₂-MIL-53(Al) (MIL = Matériaux de l'Institut Lavoisier), coupled with infrared spectroscopy, we studied their framework structural modifications and CO₂-framework interactions in the pressure range of 0-10 GPa.

In this thesis, we found that activated frameworks of MIL-53(Al) and NH₂-MIL-53(Al) with empty channels exhibited remarkable structural stability. Also, pressure-induced intra-framework interactions between OH groups of their frameworks and octahedral [AlO₆] were observed. For the CO₂ adsorption performance, their adsorption sites are located around the OH groups of the frameworks forming hydrogen bonds with CO₂. In our case, pressure-enhanced guest-host interactions were demonstrated for both MOF systems. Upon compression, a well-enhanced CO₂ adsorption in MIL-53(Al) was demonstrated. Upon complete decompression, although some of the CO₂ molecules were released to the air, considerable CO₂ molecules remained in the framework. For CO₂-loaded NH₂-MIL-53(Al), there were four different CO₂-framework interactions co-existing upon compression: between one dimeric CO₂ species and two bridging OH groups (dimeric adsorption); between one CO₂ molecule and one bridging OH group (large-pore adsorption); between one CO₂ molecule and two bridging OH groups (narrow-pore adsorption); between CO₂ molecules and -NH₂ groups (amino adsorption). High pressures made the narrow-pore adsorption more favorable over the other three. When all the applied pressures released, the pressure-regulated CO₂ adsorption behaviors of NH₂-MIL-53(Al) were fully recovered.

Co-Authorship Statement

In *Chapter 3*, activated NH₂-MIL-53(Al) and the attached PXRD patterns in Appendix B were offered by Vinicius Martins. The other materials were prepared and then verified via PXRD by Boqing Li.

Boqing Li collected all the IR spectra and wrote the draft of this thesis. Dr. Yining Huang and Dr. Yang Song edited the content.

Acknowledgments

First of all, I would like to acknowledge my supervisors, Dr. Yining Huang and Dr. Yang Song, thank you for being such a great mentor, offering precious guidance all the time. Your patience and enthusiasm for teaching have made it easy to come to you when I was in trouble, and I have learned a lot from you throughout my study in Western University. Without your inspiring advice and constant encouragement, I would not have completed my master's study smoothly.

I appreciate all my lab colleagues in both Dr. Huang and Song's lab working with me. In a collaborative and supportive environment, I have worked efficiently and enjoyably. Thank you to Vinicius Martins and Heng Xiang, for tutoring me in our labs and offering helps at any time when I came to you. I have enjoyed working with you in the past years. I would also like to thank all my friends Shangyang Shang, Cecilia Garcia, Shu Yin, Xiji Zha, Wanying Li, Liyuan Wang, Jia Zhou, they have comforted my anxiety and encouraged me on my road of chasing dreams. Thank you to Liyuan Ye, Rongfeng Guan, Qi Qi, Long Ma, Yifan Wang, Cesar Simental, you gave me a wonderful experience in Canada.

Last but not least, I would like to thank my family for supporting me through this endeavor. Thank you to my parents, for raising me and supporting throughout my life. Thank you to my mom, for being someone who I can talk to about anything.

Table of Contents

Abstract.....	ii
Summary for Lay Audience.....	iv
Co-Authorship Statement.....	v
Acknowledgments.....	vi
Table of Contents.....	vii
List of Tables.....	x
List of Figures.....	xi
List of Abbreviations.....	xv
List of Appendices.....	xvii
Chapter 1	1
1 Introduction.....	1
1.1 Metal-organic frameworks.....	1
1.2 The flexibility of MOFs.....	2
1.2.1 Guest-induced phase transitions in MOFs.....	2
1.2.2 Pressure-induced phase transitions in MOFs.....	4
1.2.3 Temperature-induced phase transitions in MOFs.....	7
1.3 CO ₂ adsorption in MOFs.....	8
1.4 CO ₂ adsorption under high pressures in MOFs.....	9
1.4.1 CO ₂ adsorption under high loading pressure.....	9
1.4.2 CO ₂ adsorption under high external pressure.....	10
1.5 Methodologies of high-pressure studies.....	13
1.5.1 Diamond anvil cell (DAC).....	13
1.5.2 <i>In situ</i> vibrational spectroscopy of high-pressure studies.....	15
1.5.3 High-pressure IR spectra of CO ₂	16

1.6 Motivations of the thesis	17
1.7 Outline of the thesis	18
1.8 References	18
Chapter 2	22
2 Discovering the High-Pressure Stability of and Pressure-Enhanced CO ₂ Storage in MIL-53(Al) by <i>In Situ</i> Infrared Spectroscopy	22
2.1 Introduction.....	22
2.2 Experimental section.....	24
2.2.1 MOF preparation.....	24
2.2.2 Cryogenic CO ₂ loading.....	25
2.2.3 High-pressure <i>in situ</i> IR spectroscopy	25
2.3 Results and discussion	26
2.3.1 IR spectra of MIL-53(Al) at ambient pressure	26
2.3.2 High-pressure study of as-made MIL-53(Al)	28
2.3.3 High-pressure study of activated MIL-53(Al)	30
2.3.4 High-pressure study of CO ₂ -loaded MIL-53(Al).....	35
2.3.5 Comparison of high-pressure behaviors of as-made, activated, and CO ₂ - loaded MIL-53(Al).....	40
2.4 Conclusion	42
2.5 References.....	42
Chapter 3	44
3 Investigating the High-pressure Behaviors and CO ₂ -Framework Interactions of NH ₂ -MIL-53(Al) using <i>In Situ</i> Infrared Spectroscopy	44
3.1 Introduction.....	44
3.2 Experimental section.....	48
3.2.1 MOF preparation.....	48
3.2.2 CO ₂ loading.....	48

3.2.3	High-pressure apparatus.....	48
3.3	Results and discussion	49
3.3.1	IR spectra of NH ₂ -MIL-53(Al) at ambient pressure	49
3.3.2	High-pressure study of activated NH ₂ -MIL-53(Al).....	51
3.3.3	High-pressure study of CO ₂ -loaded NH ₂ -MIL-53(Al)	54
3.4	Conclusion	65
3.5	References.....	65
Chapter 4	67
4	Summary and Future Work.....	67
4.1	Summary.....	67
4.2	Future work suggestions	69
Appendices.....		70
Curriculum Vitae		72

List of Tables

Table 1.1 CO ₂ adsorption capacities of selected MOFs under various pressures.	10
Table 2.1 Assignments for the characteristic IR modes of activated, as-made and CO ₂ loaded MIL-53(Al).	27
Table 2.2 Pressure dependence (dv/dP, cm ⁻¹ /GPa) of IR modes of activated MIL-53(Al). ...	34
Table 2.3 Peak area of ν _{OH} and ν ₃ + ν ₁ modes under different pressures in CO ₂ -loaded MIL-53(Al).	38
Table 2.4 The comparison of pressure dependence (dv/dP, cm ⁻¹ /GPa) of selected IR modes of as-made, activated and CO ₂ loaded MIL-53(Al).	41
Table 3.1 Assignments for the majority IR modes of NH ₂ -MIL-53 spectra.	50
Table 3.2 Pressure dependence (dv/dP, cm ⁻¹ /GPa) of selected IR modes of activated NH ₂ -MIL-53(Al).	52
Table 3.3 Normalized peak area of CO ₂ ν ₃ mode at various pressures in NH ₂ -MIL-53(Al)..	77
Table 3.4 Pressure dependence (dv/dP, cm ⁻¹ /GPa) of ν ₃ of CO ₂ in NH ₂ -MIL53(Al).....	64

List of Figures

Figure 1.1 Building blocks, such as organic ligands, can be judiciously select to design various frameworks.	1
Figure 1.2 The structure of Cu-MOF (a); 2D sheet structure (b); the side view of 2D sheet (c) (Cu = orange; C = gray; N = blue; B = pink; F = yellow green; H = white).	2
Figure 1.3 The schematic diagram of gate-opening transition of Cu-MOF and its adsorption/desorption isotherms of CO ₂ at 273 K.	3
Figure 1.4 The wine rack structure of MIL-53 family (the octahedral [MO ₆] in purple and O = red, C = orange, H = white).	3
Figure 1.5 The diagram of reversible breathing effect of MIL-53(Al).	4
Figure 1.6 The framework of [NH ₄][Zn(HCOO) ₃] and its schematic NLC behavior under increased pressure (Zn= blue; O = red; C = gray; N = purple; H = white).	5
Figure 1.7 A: the changes of the a axis (blue) and c axis (red) as a function of pressure. B: the relationships between the unit cell volume and pressure (open squares = computational data; solid squares = experimental results).....	5
Figure 1.8 Top: the changes of unit cell volume of NH ₂ -MIL-53(Al) upon compression. Bottom: the lattice parameters of NH ₂ -MIL-53(Al) as a function of pressure (GPa) (using mineral oil as the pressure-transmitting media).	7
Figure 1.9 The phase transition hysteresis illustration of MIL-53(Al).	7
Figure 1.10 Three different processes of CCS technologies.	7
Figure 1.11 The structures of MOF-177 and NU-100.	8
Figure 1.12 The topologies of CdSDB (bottom) and PbSDB (top), and Cd = purple; C = gray; O = red; S = yellow; Pb = green.....	11

Figure 1.13 The locations (labelled as C1A/C1B) of saturated CO ₂ molecules adsorbed at two binding sites in CdSDB (a, c) and at the only site in PbSDB (b) under ambient pressure and high-pressure CO ₂ adsorption sites for PbSDB under high pressures (d).	12
Figure 1.14 A photo of a DAC and enlarged illustration of its inside.	13
Figure 1.15 An example of pressure-induced red-shift of ruby fluorescence spectra when increasing the pressure from 0 GPa (in black) to 5 GPa (in red).	14
Figure 1.16 The illustration of the customized mid-IR micro-spectroscopy system in our lab.	15
Figure 1.17 CO ₂ IR spectrum at 0.4 GPa.	17
Figure 2.1 The wine-rack topology of MIL-53 (Al) (Al = green, O = red, H = white, C = grey).	22
Figure 2.2 The reversible <i>lp</i> - <i>np</i> phase transition of MIL-53(Al) (octahedral [AlO ₆] = grey octahedra, O = red circles, C = grey circles) and adsorbed H ₂ O molecules locate in the center of the <i>np</i> channels.	23
Figure 2.3 IR spectra of as-made, activated and CO ₂ -loaded MIL-53(Al) at ambient pressure.	26
Figure 2.4 The selected IR spectra of as-made MIL-53(Al) upon compression (A) and decompression (B).	29
Figure 2.5 The selected IR spectra of activated MIL-53(Al) upon compression (A) and decompression (B) in the spectral region of 650 - 1800 and 3450 - 4000 cm ⁻¹	31
Figure 2.6 The comparison of the local structure of activated MIL-53(Al) at ambient pressure (A) and at high pressure (B) with intra-framework H-bonds labelled as dashed lines (Al = dark green, O = red, H = white, C = grey).	32
Figure 2.7 An illustrate of the ‘kneecap’ motion of activated MIL-53 (M = light blue, O = red, C = grey).	32

Figure 2.8 Frequency plots of selected IR modes of activated MIL-53(Al) (solid circles) and as-made MIL-53(Al) (the hollow circle) as a function of pressure in the spectral region of 950-1100, 1350-1650 cm^{-1} (A) and 3450-3750 cm^{-1} (B).	33
Figure 2.9 Illustrations of CO ₂ adsorption sites in MIL-53(Al) (Al = light blue, O = red, H = white, C = grey).	35
Figure 2.10 Selected IR spectra of CO ₂ -loaded MIL-53(Al) upon compression (A) and decompression (B) in the frequency region of 550-2450 cm^{-1}	35
Figure 2.11 IR spectra upon compression of pure CO ₂ (A) and CO ₂ -loaded ZIF-8 (B) in the spectral region of the CO ₂ combination modes.	36
Figure 2.12 IR spectra of CO ₂ -loaded MIL-53(Al) upon compression (A) and decompression (B) in the frequency region 3600 - 3780 cm^{-1}	37
Figure 2.13 Deconvoluted IR spectra of CO ₂ -loaded MIL-53(Al) at 1.60, 2.21, and 3.05 GPa in the spectral region of the CO ₂ combination modes.	38
Figure 2.14 The comparison of the frequency plots of selected IR modes of as-made (black), activated (red) and CO ₂ loaded (blue) MIL-53(Al) as a function of pressure in the spectral region of 1400-1625 cm^{-1} (A) and 3520-3700 cm^{-1} (B).	40
Figure 3.1 Structures of terephthalic acid, 2-aminoterephthalic acid and the topology of NH ₂ -MIL-53(Al) (Al = green, O = red, H = white, C = grey, N = blue).	44
Figure 3.2 CO ₂ adsorption and desorption isotherms of MIL-53(Al) and NH ₂ -MIL-53(Al) at 298 K (P ₀ = 1.0 atm).	45
Figure 3.3 The CO ₂ /CH ₄ separation performance of NH ₂ -MIL-53(Al) at 303k and ambient pressure.	45
Figure 3.4 (A) The illustration of large pore (<i>lp</i>) to narrow pore (<i>np</i>) phase transition of NH ₂ -MIL-53(Al); (B) The diagram of the intra-framework hydrogen bonds between amino groups and octahedral [AlO ₆] (O = red, H = white, C = grey, N = dark blue, H-bond = dashed line).	46

Figure 3.5 IR spectra of activated and CO ₂ -loaded NH ₂ -MIL-53(Al) as well as activated MIL-53(Al) at ambient pressure.	49
Figure 3.6 IR spectra of activated NH ₂ -MIL-53(Al) upon compression (A) and decompression (B).	51
Figure 3.7 Frequency plots of selected IR modes of activated NH ₂ -MIL-53(Al) as a function of pressure.	52
Figure 3.8 The comparison of the local structure of activated NH ₂ -MIL-53(Al) at ambient pressure (A) and at high pressure (B) with intra-framework H-bonds labelled as dashed lines (Al = dark green, O = red, H = white, C = grey).	54
Figure 3.9 Optimized structures of NH ₂ -MIL-53(Al) with adsorbed CO ₂ (O = red, H = white, C = grey, N = dark blue, hydrogen bond = dashed line).	54
Figure 3.10 (A): Schematic diagram of dimeric CO ₂ species located in the pores of MIL-53(Al); (B): An IR tool for differentiating between monomeric and dimeric CO ₂ species in MOFs.	55
Figure 3.11 IR spectra of CO ₂ loaded ZIF-8 upon compression in the spectral region of CO ₂ combination modes.	56
Figure 3.12 IR spectra of CO ₂ loaded NH ₂ -MIL-53(Al) on compression (A) and decompression (B) at room temperature.	57
Figure 3.13 Frequency plots of $\nu_3 + \nu_1$ modes as a function of pressure.	58
Figure 3.14 Enlarged ν_3 of CO ₂ in NH ₂ -MIL-53(Al).	59
Figure 3.15 Deconvoluted ν_3 at 0.01 GPa (A), 1.52 GPa (B), 2.91 GPa (C), and 10.21 GPa (D).	60
Figure 3.16 Comparisons of spectra of activated NH ₂ -MIL-53(Al) and CO ₂ loaded NH ₂ -MIL-53(Al) under different pressures.	61
Figure 3.17 Frequency plots of ν_3 as a function of pressure.	63

List of Abbreviations

BDC 1,4-benzenedicarboxylate

BET Brunauer-Emmett-Teller

CCS carbon capture and storage

DAC diamond anvil cell

DFT density functional theory

DMF *N, N*-dimethylformamide

FTIR Fourier transform infrared

GPa gigapascal

H₂BDC 1,4-benzenedicarboxylate

HT high temperature

IR infrared

lp large pore

LP large pore

LT low temperature

MCT mercury cadmium telluride

MIL Matériaux de l'Institut Lavoisier

MOF metal-organic framework

NLC negative linear compressibility

np narrow pore

NP narrow pore

NTE negative thermal expansion

PTE positive thermal expansion

PTM pressure transmitting medium

PXRD powder X-ray diffraction

SBU secondary building unit

SDB 4,4'-sulfonyldibenzoate

SSNMR solid-state NMR

List of Appendices

Appendix A: The PXRD patterns of MIL-53(Al)- <i>as</i> , MIL-53(Al)- <i>np</i> , as well as simulated MIL-53(Al)- <i>as</i> and MIL-53(Al)- <i>np</i>	70
Appendix B: The PXRD patterns of activated NH ₂ -MIL-53(Al) and simulated NH ₂ -MIL-53(Fe).	71

Chapter 1

1 Introduction

1.1 Metal-organic frameworks

Metal-organic frameworks (MOFs) are constructed from metal-containing centers interconnected by organic linkers forming three-dimensional crystalline porous structures. Since Yaghi and Hailian prepared the first crystalline metal-organic frameworks with extended channels in 1995, MOFs, as one of the most rapidly growing classes of versatile porous materials, have been well-studied by many scholars.¹ Nowadays, MOFs are increasingly built by selecting different building blocks (Figure 1.1) and/or post-synthetic modifications. MOFs feature enormous surface area, large pore volume, high thermal stability and amazing tunability, which give them a tremendous potential for applications in diverse areas, such as gas adsorption and gas separation,^{2,3,4} drug delivery⁵ and catalysis⁶.

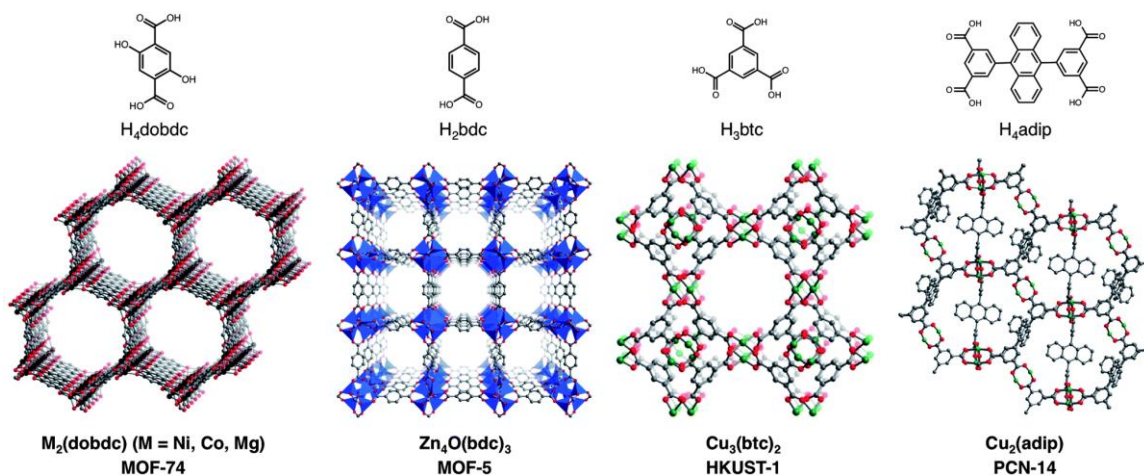


Figure 1.1 Building blocks, such as organic ligands, can be judiciously select to design various frameworks.⁴

1.2 The flexibility of MOFs

The past decade has witnessed an increased research effort focused on the flexibility of their frameworks. MOFs can respond to various physical stimulations such as guest molecules, pressure, or temperature.⁷ These interesting phenomena will be presented below by giving typical examples.

1.2.1 Guest-induced phase transitions in MOFs

MOFs are often synthesized using hydrothermal or solvothermal processes during which solvent molecules are trapped inside the framework. To activate the as-made MOFs, solvent exchange and/or solvent evacuation are used to empty the framework.⁸ In order to measure the surface area and adsorption capacity of MOFs, adsorption of N₂ and CO₂ are used respectively.⁹ Thus, guest evacuation and adsorption behaviors of MOFs have been well-studied and documented. Among these, various fascinating guest-induced phase transitions of MOFs have been reported, such as gate-opening transitions¹⁰ and breathing effects¹¹.

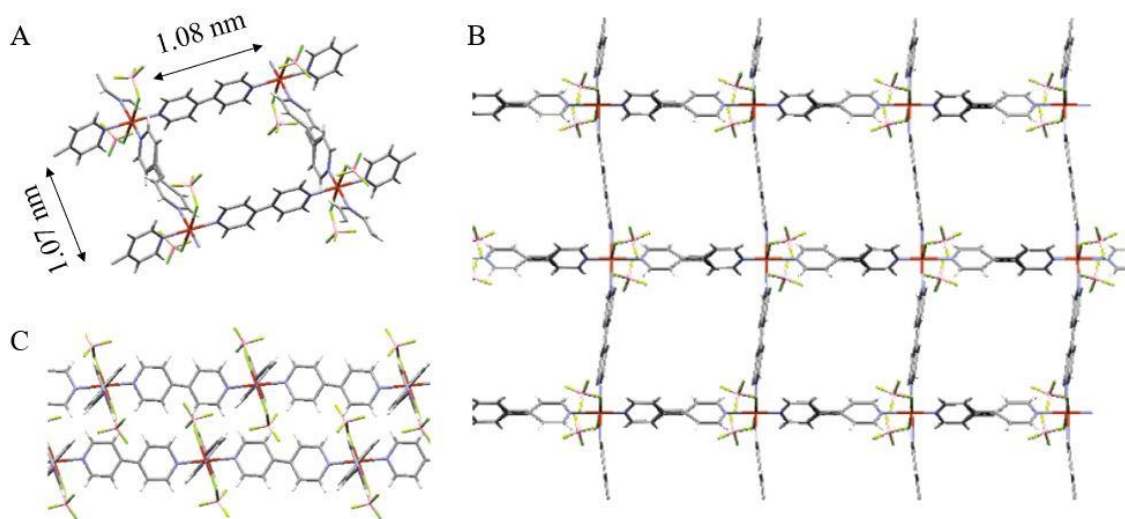


Figure 1.2 The structure of Cu-MOF (A); 2D sheet structure (B); the side view of 2D sheet (C) (Cu = orange; C = gray; N = blue; B = pink; F = yellow green; H = white).¹²

One of the most interesting gate-opening transitions was reported in a 2D layered stacking Cu-MOF, [Cu(BF₄)₂-(bpy)₂] (bpy = 4,4'-Bipyridine).¹² The details of this

square-grid-type Cu-MOF are presented in Figure 1.2. The framework is built with the Cu(II) ion and bpy in a $1.07 \times 1.08 \text{ nm}^2$ square grid sheet, the location of BF_4^- anions is axial. The interlayer distance between the adjacent sheets is 0.46 nm. A synchrotron powder X-ray diffraction pattern was collected at 273 K to characterize its CO_2 adsorption behavior. After adsorbing CO_2 gas, the interlayer distance expanded to 0.68 nm, in a so-called ‘gate-opening’ transition (Figure 1.3). The authors indicated that this reversible expansion/contraction transition of Cu-MOF is triggered by interactions between the framework and gas molecules, resulting from the clathrate structure.

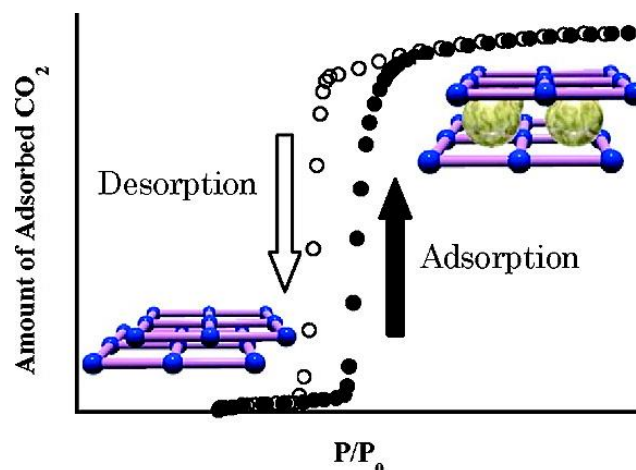


Figure 1.3 The schematic diagram of gate-opening transition of Cu-MOF and its adsorption/desorption isotherms of CO_2 at 273 K.¹²

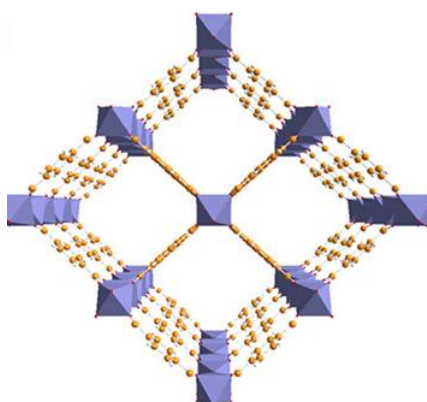


Figure 1.4 The wine rack structure of MIL-53 family (the octahedral $[\text{MO}_6]$ in purple and O = red, C = orange, H = white).¹¹

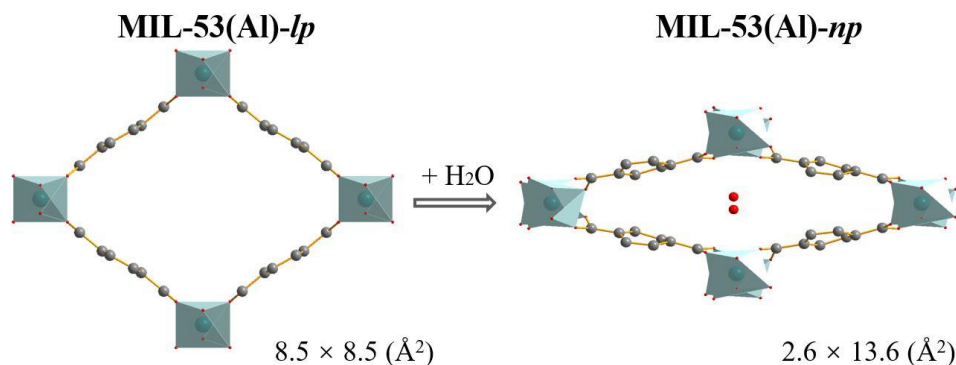


Figure 1.5 The diagram of reversible breathing effect of MIL-53(Al).

MIL-53 (MIL = Matériaux de l'Institut Lavoisier) family is one of the most famous flexible MOFs. Owing to its wine-rack structure, it exhibits the most typical breathing effect.¹¹ MIL-53(Cr) was first synthesised by Millange *et al.* in 2002¹³ and its very large breathing effect triggered by adsorption of H₂O was reported several months later by Serre *et al.*¹⁴ The activated MIL-53 consists of octahedral [MO₆] (M = Cr³⁺, Al³⁺, Fe³⁺, Sc³⁺, Ga³⁺, In³⁺) metal clusters interconnected by BDC linkers (BDC = benzenedicarboxylic acid) forming a wine rack framework in a large pore (*lp*) phase as shown in Figure 1.4. At 273 K, MIL-53-*lp* adsorbs H₂O molecules from the atmosphere and transitions to a narrow pore (*np*) phase. Both structures, in *lp* and *np* phases, were determined using powder X-ray diffraction (PXRD). Moreover, the framework recovered from the *np* to *lp* by emptying the channels under vacuum. This reversible shrinkage/expansion transition is called breathing effect (Figure 1.5). A growing number of publications about the MIL-53 (M = Cr,¹⁴ Al,⁸ Fe,¹⁵ Sc,¹⁶ Ga,¹⁷) family has shown that their breathing effect transition can be driven by various guest molecules, such as H₂O, CO₂ and CH₄.

1.2.2 Pressure-induced phase transitions in MOFs

The most common pressure-induced phenomenon in MOFs is the crystalline to amorphous transformation. Pressure-induced amorphization was observed on the family of zeolitic imidazolate frameworks (ZIFs), which have been deeply studied.^{18,19,20} An increasing number of crystal-to-crystal transitions in MOFs induced by pressure have been discovered. One of the most typical types of crystal-to-crystal transitions in MOFs is negative linear compressibility (NLC), in which the framework expands along one or two

directions under high pressure, while reducing its unit cell volume. The NLC phenomenon in MOFs was first observed by Li *et al.* in a zinc formate framework, $[\text{NH}_4][\text{Zn}(\text{HCOO})_3]$, due to its ‘wine rack’ framework topology (Figure 1.6 A).²¹ Figure 1.6 B illustrates the behavior of the framework under high pressure. Confirmed by high-pressure single crystal X-ray diffraction and DFT calculations, $[\text{NH}_4][\text{Zn}(\text{HCOO})_3]$ underwent a pressure-induced NLC along its *c* axis with the reduction of the *a* and *b* axes, resulting in the shrinkage of its pore volume (Figure 1.7).

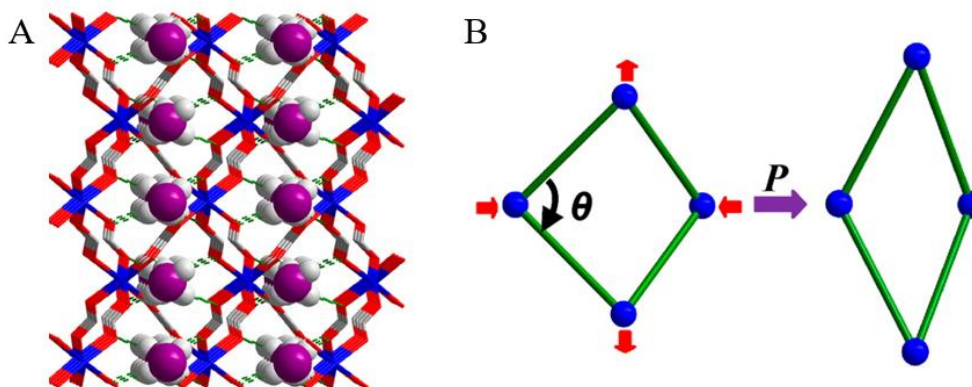


Figure 1.6 The framework of $[\text{NH}_4][\text{Zn}(\text{HCOO})_3]$ and its schematic NLC behavior under increased pressure (Zn= blue; O = red; C = gray; N = purple; H = white).²¹

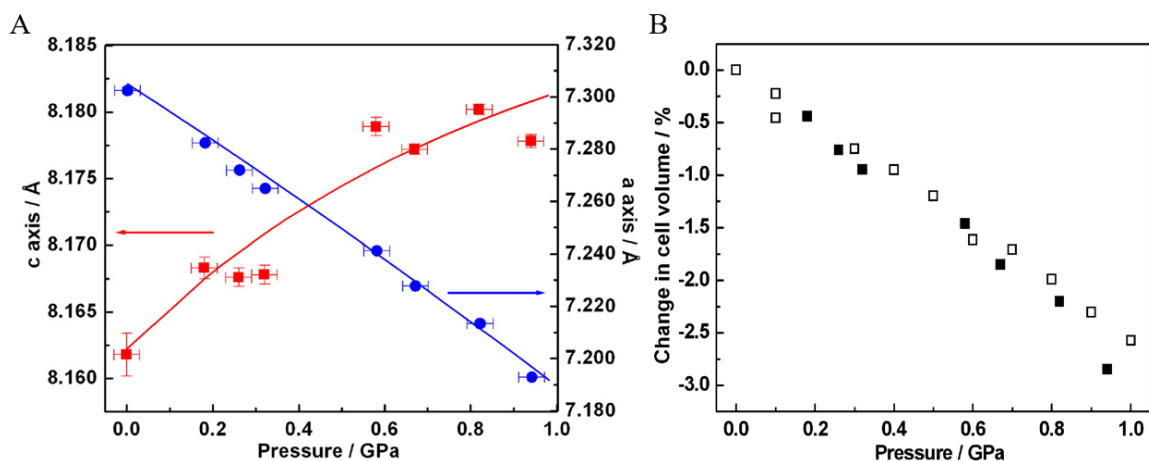


Figure 1.7 A: the changes of the *a* axis (blue) and *c* axis (red) as a function of pressure. B: the relationships between the unit cell volume and pressure (open squares = computational data; solid squares = experimental results).²¹

The MIL-53 family also exhibits a typical wine rack structure. Unsurprisingly, Serra-Crespo *et al.* demonstrated that MIL-53(Al) and NH₂-MIL-53(Al) experienced NLC upon increased pressure via *in situ* PXRD.²² Figure 1.8 below shows the changes of the unit cell volume and the lattice parameters of NH₂-MIL-53(Al) as a function of pressure up to 11 GPa. The framework expanded in the b axis while reducing along a and c axes from 0 to 2 GPa, causing a reduction of its unit cell volume from 1433 Å³ to ~1000 Å³ and confirming NLC. However, when the pressure exceeded 2 GPa, pressure-induced contraction occurred in all three axes of its framework, no longer showing NLC. In this experiment, the pressure-induced phase transition includes two different stages: from 0-2 GPa the framework underwent a *lp* to *np* transition (crystal-to-crystal transition), and from 2-11 GPa the framework gradually became amorphous (pressure-induced amorphization). Its framework remains crystalline up to 6 GPa, exhibiting similar pressure resistance as most MOFs.²³ It is also worth noting that they compared the high-pressure behavior of NH₂-MIL-53(Al) using different pressure-transmitting media (mineral oil and ethanol). It has been well-demonstrated that pressure-induced transitions in MOFs vary with the pressure transmitting medium (PTM) used, and NH₂-MIL-53(Al) is no exception. Compared with ethanol, mineral oil has lower affinity with the framework. With increased pressure, the mineral oil is evicted from the framework, resulting in a *lp* to *np* transition (at ~2 GPa). In contrast, the strong interactions between ethanol and the framework make it unable to undergo the *lp* to *np* transition.

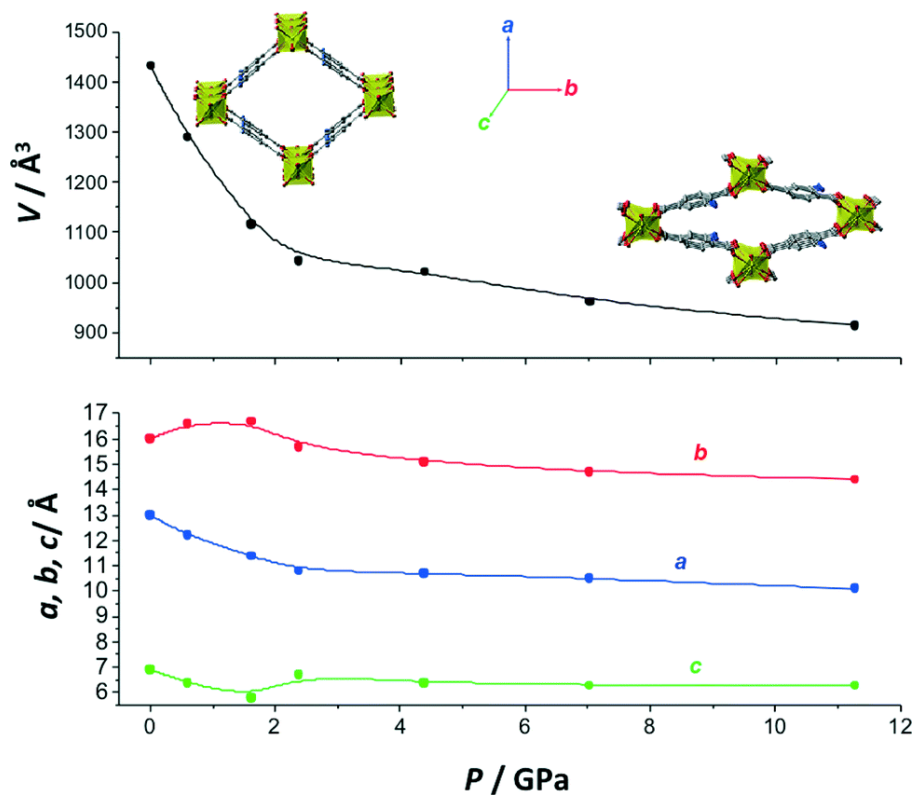


Figure 1.8 Top: the changes of unit cell volume of NH₂-MIL-53(Al) upon compression. Bottom: the lattice parameters of NH₂-MIL-53(Al) as a function of pressure (GPa) (using mineral oil as the pressure-transmitting media).²²

1.2.3 Temperature-induced phase transitions in MOFs

Even though positive thermal expansion (PTE) is a feature of most materials, negative thermal expansion (NTE) is commonly found in MOFs.²⁴ Instead of expansion, many MOFs undergo a shrinkage of the framework with increased temperature, such as MOF-5²⁵, MOF-C22²⁶, and the majority of ZIF family²⁷. Along with NTE, these MOFs exhibit temperature-induced reversible crystal-crystal phase transitions with hysteresis. A representative thermo-responsive phase transition with a wide hysteresis was first observed in MIL-53(Al).²⁸ As we can see from Figure 1.9, MIL-53(Al) underwent a transition from HT (high temperature) phase to LT (low temperature) phase from 125 to 150 K, whereas the LT to HT phase transition occurs from 325 to 375 K. DFT calculations were carried out and the results demonstrated that the driving force of the

temperature-induced phase transitions of MIL-53(Al) is the low-energy vibrational motion of the benzene ring located in the organic linkers of the framework.

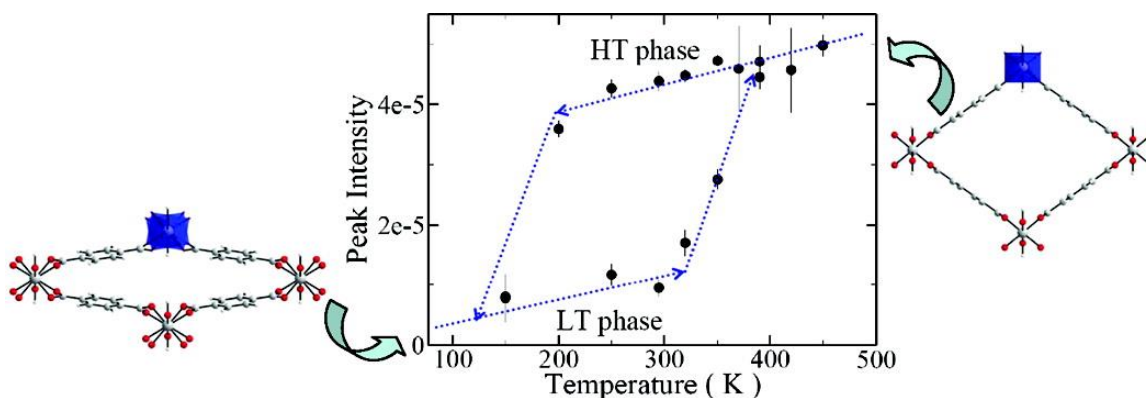


Figure 1.9 The phase transition hysteresis illustration of MIL-53(Al).²⁸

1.3 CO₂ adsorption in MOFs

Global warming is a major concern since the early 21st century and is mainly attributed to the consumption of various fuels.²⁹ Carbon capture and storage (CCS) technologies have been developed to tackle this issue.³⁰ This is a process in which CO₂ is captured and recycled to use in different industries, such as chemical production facilities and the food industry.³¹ CCS can be implemented in three different processes (Figure 1.10), pre-combustion, oxyfuel combustion and post-combustion. Post-combustion is the most efficient and cheapest method involving the adsorption of CO₂ from flue gas. Given their unique features, MOFs became one of the most promising candidates of gas adsorption and have received widespread attention from researchers.

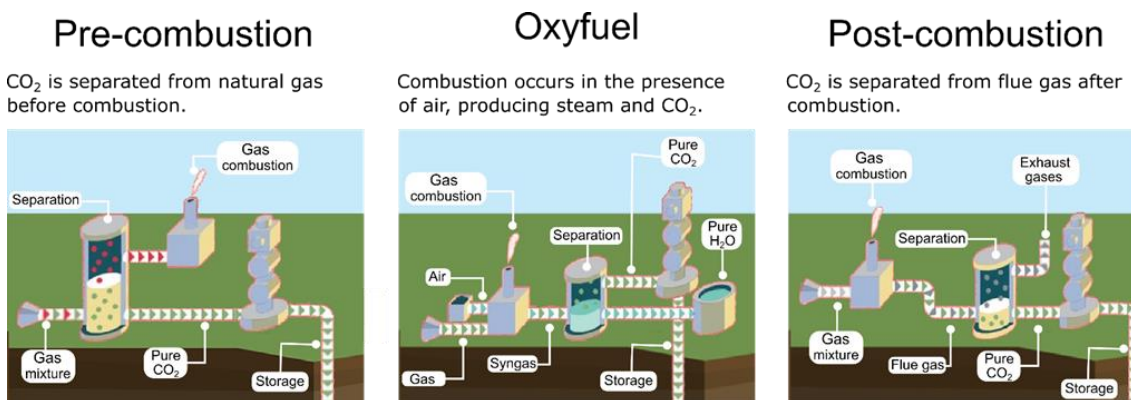


Figure 1.10 Three different processes of CCS technologies.³¹

Owing to their high porosity and high surface area, MOFs exhibit excellent CO₂ affinity.³² There are two different adsorption mechanisms in MOFs.³³ Physisorption involves weak chemical bonding between CO₂ and MOFs, which usually occurs at high loading pressure. Chemisorption takes place at low pressure by forming covalent bonds between CO₂ and the framework. To quantify the CO₂ adsorption capacity of MOFs, a method called gravimetric CO₂ uptake is used. For instance, MOF-177 features an ultra-high surface area (4,508 m²/g) at 35 bar and 298 K, and it displays a considerable CO₂ adsorption capacity of 1656 mg/g (Figure 1.11).³⁴ Remarkably, NU-100 exhibits an even higher surface area (6,143 m²/g), at 40 bar and 298 K, it can adsorb 2315 mg/g of CO₂.³⁵

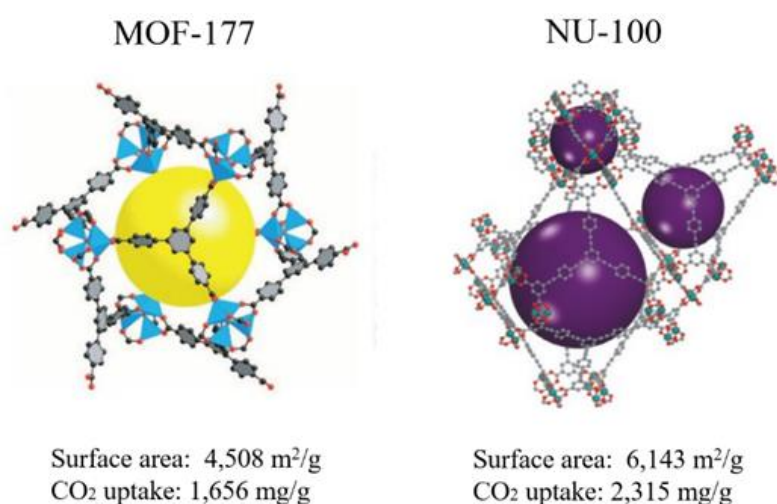


Figure 1.11 The structures of MOF-177 and NU-100.^{34, 35}

1.4 CO₂ adsorption under high pressures in MOFs

1.4.1 CO₂ adsorption under high loading pressure

According to previous studies, the maximum CO₂ uptake by MOFs is commonly obtained under high loading pressure.³⁶ The table below list MOFs whose CO₂ adsorption capacities are improved by increased loading pressure.^{37,38,39} For example, under high CO₂ pressure of 25 bar, USO-2-Ni captures 60 wt% of CO₂, while under 1 bar its CO₂ uptake is 10 wt%.

Table 1.1 CO₂ adsorption capacities of selected MOFs under various pressures

MOF	Temperature (K)	CO ₂ uptake at 1 bar	CO ₂ uptake at high pressure	Loading pressure (bar)	Ref
Ni-STA-12	304	2.5 mmol/g	6.0 mmol/g	15	37
Zn ₂ (tcom)(dabco)-Lon.	298	4.6 wt%	14 wt%	25	38
Zn ₂ (tcom)(pz)-Ad.	298	6.4 wt%	24 wt%	25	38
USO-2-Ni	298	10 wt%	60 wt%	25	39
USO-1-Al	298	10.6 wt%	35 wt%	25	39

1.4.2 CO₂ adsorption under high external pressure

Based on the discussion above, the extraordinary flexibility of MOFs distinguishes them from traditional porous materials. An increasing number of studies demonstrate that the flexibility of MOFs could play an important role in guest adsorption performance not only in ambient conditions, but also under extremely high external pressure in the gigapascal range. One of the most well-studied MOFs is ZIF-8, usually loaded with small molecules, including CO₂,⁴⁰ methanol and ethanol, CH₄ and N₂.⁴¹ The flexibility of the organic linker of ZIF-8 facilitates its structural modifications upon compression and its CO₂ adsorption capacity is enhanced with increased pressure.⁴⁰ It has been well-demonstrated that high external compression can be used to enhance the CO₂ adsorption capacity of MOFs.^{40,42,43,44}

One of the most interesting cases of pressure-enhanced CO₂ adsorption in MOFs was reported by Jiang *et al.*, who compared the different CO₂ adsorption behaviors of two structurally related SDB-based (SDB = 4,4'-sulfonyldibenzoate) MOFs: CdSDB and PbSDB. Pressure-enhanced CO₂ adsorption was evidenced in CdSDB and a new CO₂ adsorption site was identified in PbSDB.⁴⁵ CdSDB and PbSDB are built with the same SDB linker, however, different metal ions lead to different coordination with SDB,

resulting in different framework structures (Figure 1.12). Compared with CdSDB with a pore size of 8.8×8.5 (\AA^2), PbSDB features a relatively smaller pore size of 7.4×7.5 (\AA^2). Moreover, their CO_2 adsorption behaviors at ambient conditions have been reported by previous studies.^{46,47} Chen *et al.* demonstrated via ^{13}C Solid-state NMR (SSNMR) results that CdSDB displays two non-equivalent CO_2 adsorption sites in its channels (Figure 1.13 a, c), whereas only one CO_2 binding site is observed in the framework of PbSDB (Figure 1.13 b).⁴⁷ Under high pressure, the two CO_2 binding sites in CdSDB basically remain the same and equally favored, while a new binding site appears in PbSDB. The authors also indicated that upon compression, CO_2 molecules gradually migrate from the

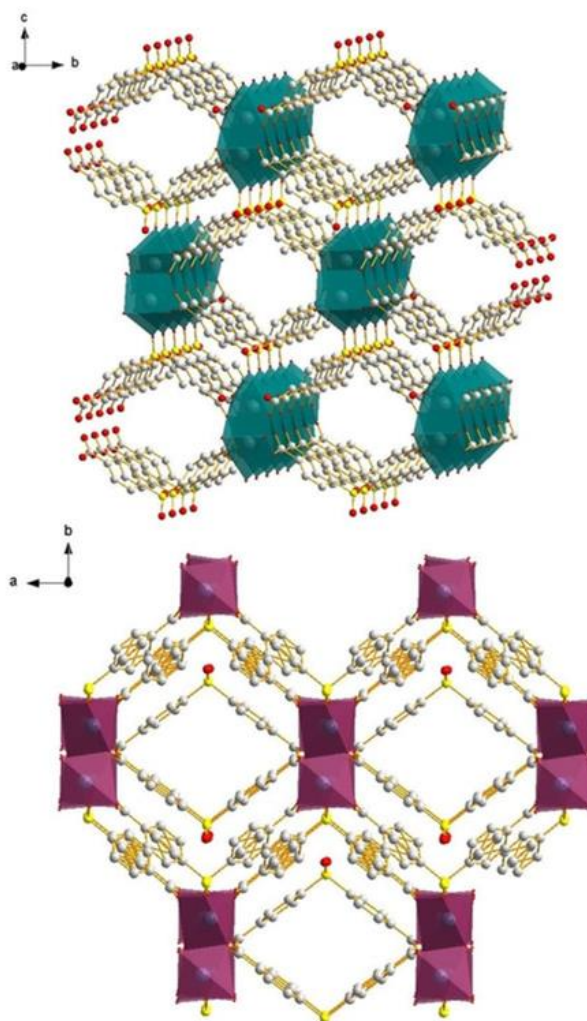


Figure 1.12 The topologies of CdSDB (bottom) and PbSDB (top), and Cd = purple; C = gray; O = red; S = yellow; Pb = green.⁴⁵

original site to the new site, which becomes the dominating site when pressure goes higher than 1.68 GPa.

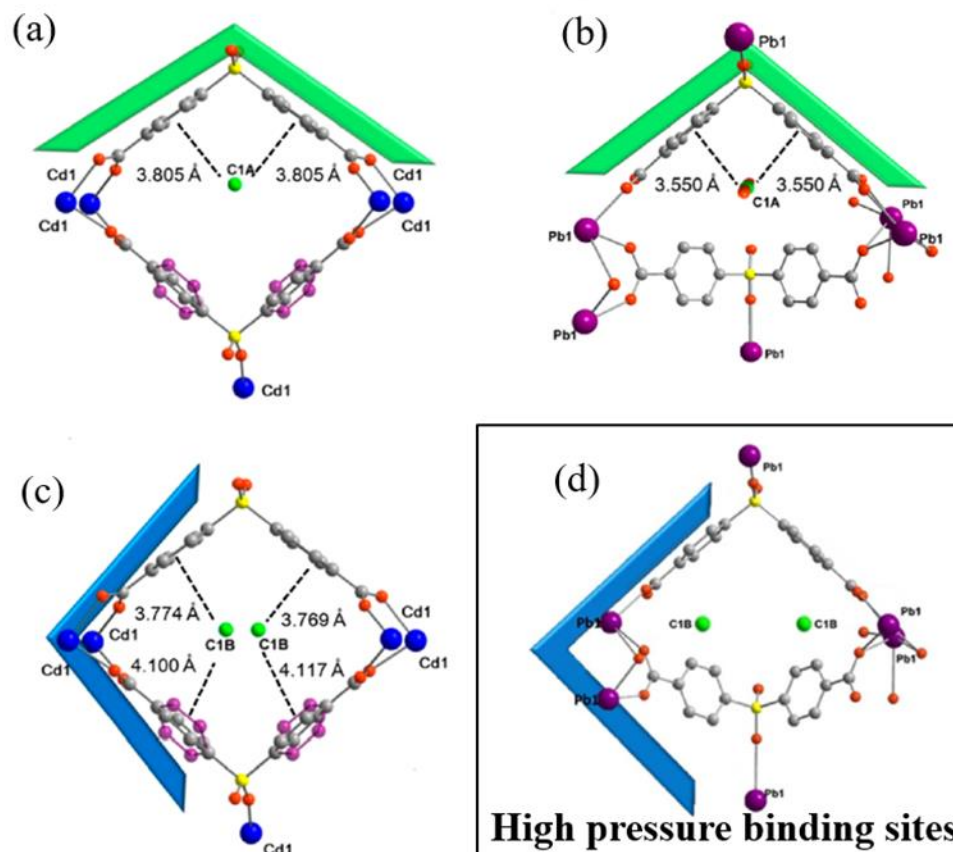


Figure 1.13 The locations (labelled as C1A/C1B) of saturated CO₂ molecules adsorbed at two binding sites in CdSDB (a, c) and at the only site in PbSDB (b) under ambient pressure and high-pressure CO₂ adsorption sites for PbSDB under high pressures (d).^{45, 46, 47}

1.5 Methodologies of high-pressure studies

1.5.1 Diamond anvil cell (DAC)

Pressure (P) equals to the perpendicular force (F) over the area (A) of the surface of an object, that is $P = \frac{F}{A}$. To generate high static pressure reaching gigapascal range (1 GPa = 10^9 Pa = 10^4 bar) in scientific laboratories, one of the most efficient devices is the diamond anvil cell (DAC).^{48,49,50} As illustrated in Figure 1.14, two identical diamonds aligned with face-to-face tiny tips (also called culets). The diameter of the culets typically varies from tens to hundreds of microns depending on the target pressure of the experiment. By tightening the four screws of the anvil manually, pressures in gigapascal range can be generated easily between these two diamonds. For example, 1 N can generate 35 bar on a 600 μm culet. What distinguishes the DAC from other high-pressure apparatus is the transparency of diamonds to a wide spectral range of electromagnetic radiation, making various *in situ* characterisation techniques feasible, including vibrational spectroscopy and X-ray diffraction.⁵¹ Different probes require different diamonds, types I and II diamonds are used for Raman and infrared (IR) spectroscopies, respectively. Compared with Type I diamonds with two strong absorption regions at $1000\text{--}1350\text{ cm}^{-1}$ and $\sim 2000\text{ cm}^{-1}$, type II diamonds have a quite low absorption region below 2000 cm^{-1} , making IR measurements feasible using DAC.

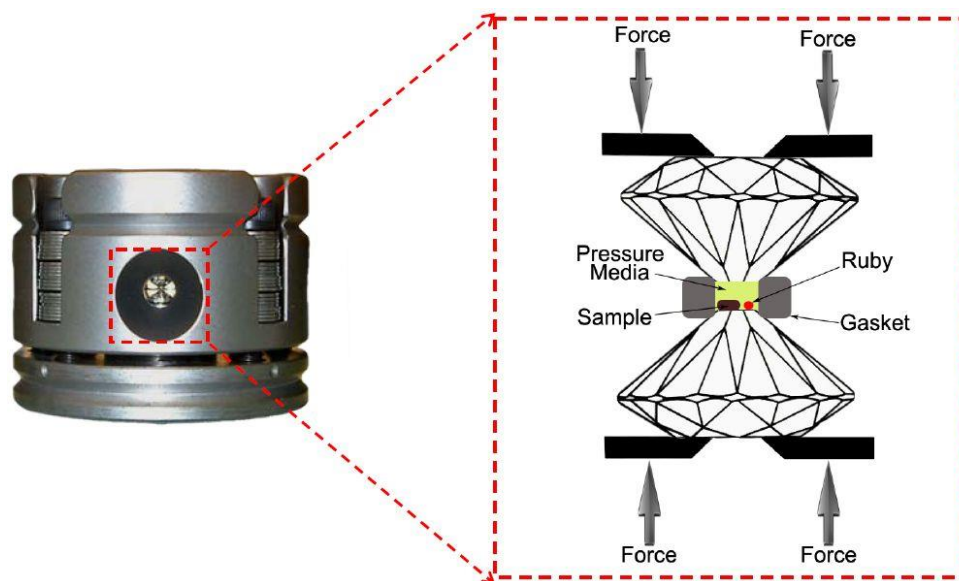


Figure 1.14 A photo of a DAC and enlarged illustration of its inside.⁵⁰

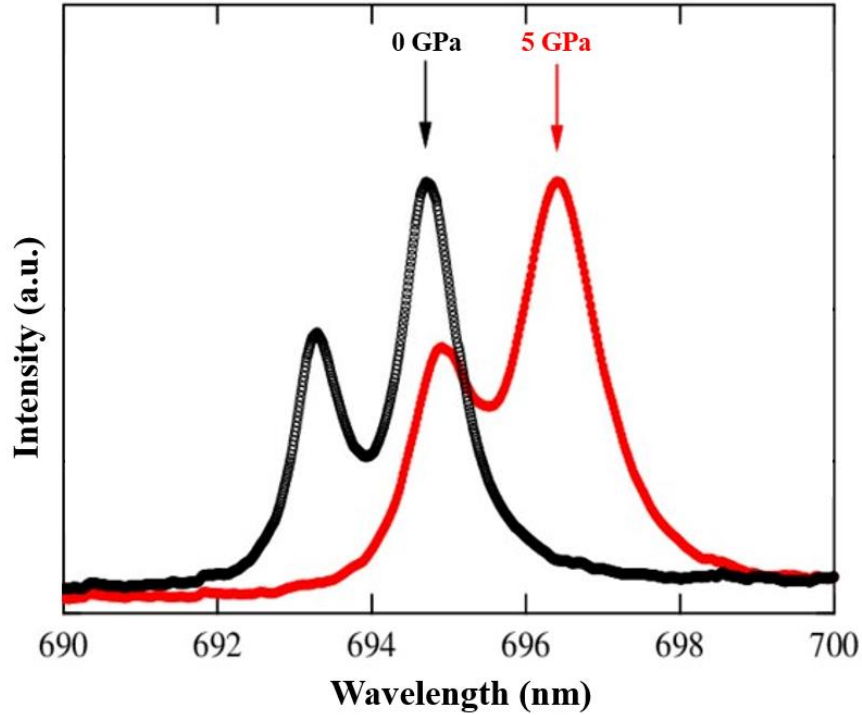


Figure 1.15 An example of pressure-induced red-shift of ruby fluorescence spectra when increasing the pressure from 0 GPa (in black) to 5 GPa (in red).

A stainless-steel gasket with a thickness of hundreds of μm is pre-indented to a thickness of tens of μm , and in the center of the pre-indented mark, a hole will be drilled about 1/3 - 1/2 of the mark in diameter. The sample will be loaded inside this hole with ruby chips ($\alpha\text{-Al}_2\text{O}_3$ doped with Cr^{3+}) in order to monitor the pressure applied on the sample, whose behavior under pressure is known. The gasket is placed in between the diamond tips. Ruby fluorescence has been widely used for decades. When ruby chips are excited by a laser, Cr^{3+} emits pressure-sensitive Raman peaks R_1 and R_2 . As shown in Figure 1.15, peaks R_1 and R_2 will undergo a predictable and quantizable red shift upon compression. Equation 1.1 depicts the pressure (P , in GPa) as a function of the wavelength difference ($\Delta\lambda$) of ruby R-line emission.⁵² In the equation, B is a constant equal to 7.665 or 5, referring to quasi- or non-hydrostatic conditions, respectively. Using this method high resolution (± 0.05 GPa) of applied pressure can be achieved.

$$P = \frac{1904}{B} \left[\left(1 + \frac{\Delta\lambda}{694.24} \right)^B - 1 \right] \quad \text{Equation 1.1}$$

1.5.2 *In situ* vibrational spectroscopy of high-pressure studies

All atoms of a molecule are constantly in motion. Typically, molecules have one type of external motion (translations) and two types of internal motions (rotations and vibrations). Vibrational spectroscopy is a powerful characterization method that measures the distinct vibrational energy of each chemical bond in a compound. When a molecule interacts with an electromagnetic field, the energy at the vibrational level (1-1000 μm) transfers from the electromagnetic field to the molecule, which is captured by the vibrational spectrometer, revealing information regarding chemical bonding, short-range molecular structures and changes of molecular configurations of a compound. One of the most well-established techniques of vibrational spectroscopy is infrared (IR) spectroscopy, where infrared lights with wavelengths of 2.5 μm to 25 μm are used as the electromagnetic radiation. If the vibration alters the dipole moment of a molecule, the vibrational mode is considered as IR active. Complementary to IR spectroscopy, Raman

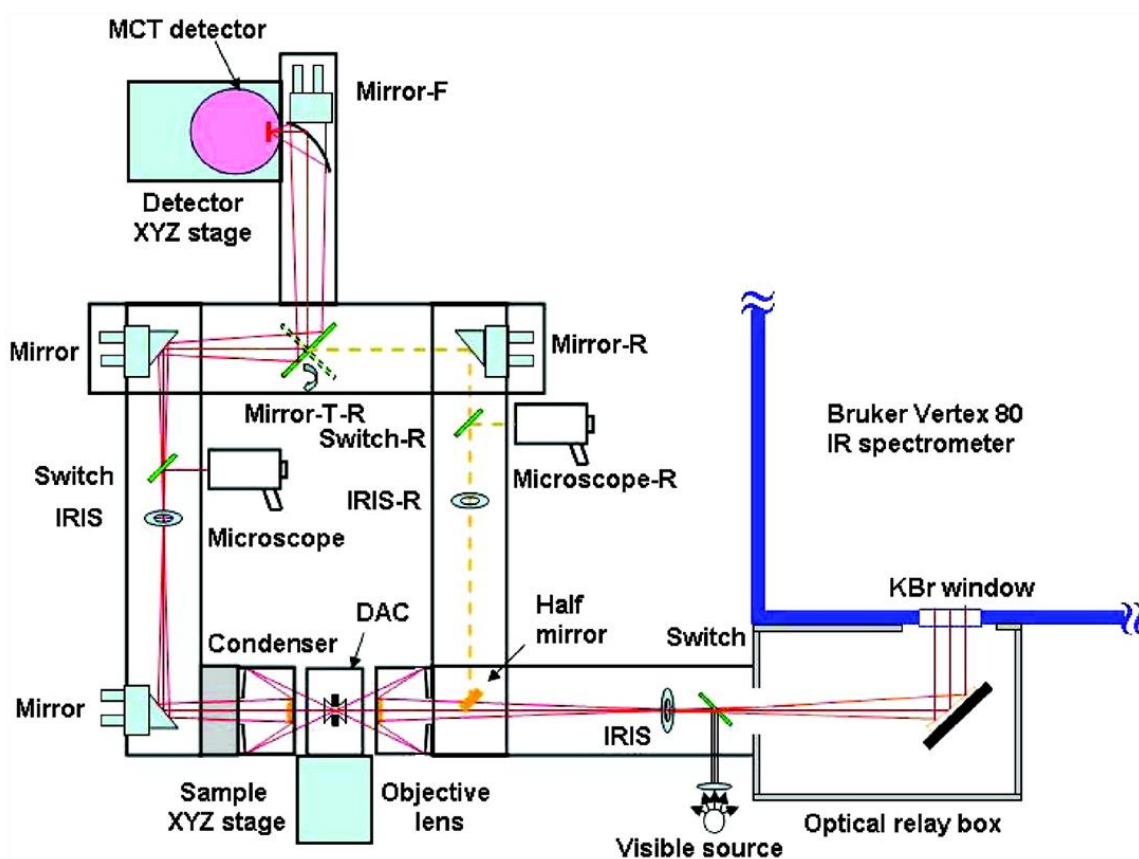


Figure 1.16 The illustration of the customized mid-IR micro-spectroscopy system in our lab.⁵³

spectroscopy is another method that uses molecular vibrational modes to provide a structural fingerprint of a compound by detecting the change of molecular polarizability. To understand the structural changes and host-guest interactions of MOFs upon compression, *in situ* vibrational spectroscopy is the most powerful technique. In order to interface with DAC, highly customized spectrometers are employed. In our laboratory, a customized IR spectroscope is used with microscopes (IR micro-spectroscopy system) to allow optical observations through the diamond window of the DAC.⁵³ More details are presented in Figure 1.16. The major optical components are a Fourier transform infrared (FTIR) spectrometer and a Globar mid-IR light source purchased directly from Bruker Optics Inc. (Model Vertex 80v), and then operated under vacuum (has to be less than 5 mbar) to prevent the air impurities (e.g. water and CO₂) from obstructing the measurements. The optical path is marked as solid red lines in Figure 1.16. Through a KBr window, the collimated mid-IR beam is guided by an optical relay box passing an IRIS optics to a 15× reflective objective lens. Focused on the aligned sample chamber of the DAC, the IR beam is regulated by a series of iris apertures to match the size of the sample. Another identical reflective objective is used as a condenser to collect the transmitted IR beam and then guided by a series of mirrors to a mid-band mercury cadmium telluride (MCT) detector. In the spectral range of 600 to 4500 cm⁻¹, the detector measures the signal through a ZnSe window. The other optical path illustrated as dashed yellow lines in Figure 1.16 shows IR measurements in the absorption mode of the customized IR spectrometer.

1.5.3 High-pressure IR spectra of CO₂

CO₂ is the focal point of this thesis. Thus, it is of great significance to understand its IR spectra and high-pressure behaviors. Given that all the IR measurements of this thesis were carried at room temperature (~298 K), all the high-pressure behaviors of CO₂ discussed below are limited to 298 K. CO₂ is a centrosymmetric linear molecule. It has three fundamental vibrational modes: the symmetric stretching mode (ν_1), the bending mode (ν_2), and the asymmetric stretching mode (ν_3). Since the ν_1 mode is silent in IR, the IR profile of CO₂ only shows two fundamental peaks (ν_2 and ν_3). Under the CO₂ loading conditions of high-pressure studies, the quantities of loaded CO₂ are barely controllable,

and extremely saturated fundamental modes of CO₂ are observed (Figure 1.17). Moreover, the other two high-frequency weak bands at ~3600 cm⁻¹ ($\nu_3 + 2\nu_2$) and ~3700 cm⁻¹ ($\nu_3 + \nu_1$) are assigned to CO₂ combination modes (Figure 1.17). Many previous studies have verified that the CO₂ combination modes resulting from the strong Fermi resonance effect⁵⁴ are potent tools to investigate the interactions between CO₂ and MOFs.
40,43,44,45

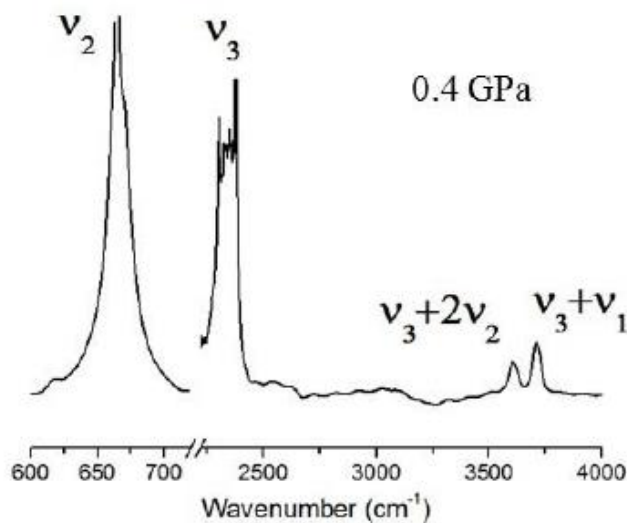


Figure 1.17 CO₂ IR spectrum at 0.4 GPa.⁵⁴

1.6 Motivations of the thesis

As discussed above, MIL-53(Al) and NH₂-MIL-53(Al) feature wine-rack structures and at ~2 GPa their flexible frameworks enable them to undergo the pressure-induced *lp* to *np* transition.²² Secondly, many previous studies have demonstrated that high external compression is one of the most effective methods to enhance the CO₂ adsorption capacities of MOFs.^{40,43,44,45} Under near ambient pressures, MIL-53 family exhibits excellent CO₂ affinity attributed to the interactions between CO₂ and the bridging OH groups of the frameworks.¹⁴ Given that pressures could easily shorten distances between OH groups and CO₂, it highly expected that MIL-53(Al) and NH₂-MIL-53(Al) can exhibit pressure-enhanced CO₂ storage upon compression. Furthermore, compared to the substantial investigations of MOFs under near ambient pressures, the studies of MOFs under high pressures in gigapascal level are much less reported.

Therefore, it is of great significance to carry out high-pressure studies in gigapascal range on MIL-53(Al) and NH₂-MIL-53(Al).

1.7 Outline of the thesis

We basically laid emphasis on high-pressure structural stabilities and CO₂-framework interactions of two well-known flexible MOFs, MIL-53(Al) and NH₂-MIL-53(Al). We also tried to shed light on how the flexibilities of their frameworks influence their high-pressure CO₂ adsorption capacities.

Chapter 2 verified the excellent high-pressure stability of activated MIL-53(Al), and pressure-induced intra-framework hydrogen bonds between OH groups and octahedral [AlO₆] were observed using *in situ* IR spectroscopy. Pressure-enhanced CO₂ storage of MIL-53(Al) was also demonstrated. It turned out that the flexibility of the framework (*lp* - *np* transition) played a significant role in the pressure-induced intra-framework interactions and CO₂ adsorption capacity. *Chapter 3* focused on high-pressure performance of the activated and CO₂-loaded NH₂-MIL-53(Al) systems. Activated NH₂-MIL-53(Al) exhibited pressure-enhanced intra-framework interactions via two kinds of hydrogen bonding. Pressure-induced additional CO₂ adsorption sites of NH₂-MIL-53(Al) were also observed. A discussion on the similarities and differences between MIL-53(Al) and NH₂-MIL-53(Al) was also included in *Chapter 3*. Finally, *Chapter 4* provides a summary of the thesis and some suggestions for future work.

1.8 References

1. Yaghi, O. M.; Li, H. *J. Am. Chem. Soc.* **1995**, *117*, 10401-10402.
2. Sumida, K.; Rogow, D. L.; Mason, J. A.; McDonald, T. M.; Bloch, E. D.; Herm, Z. R.; Bae, T. H.; Long, J. R. *Chem. Rev.* **2012**, *112*, 724-781.
3. Bae, Y. S.; Snurr, R. Q. *Angew. Chem. Int. Ed.* **2011**, *50*, 11586-11596.
4. Mason, J. A.; Veenstra, M.; Long, J. R. *Chem. Sci.* **2014**, *5*, 32-51.
5. Horcajada, P.; Gref, R.; Baati, T.; Allan, P. K.; Maurin, G.; Couvreur, P.; Ferey, G.; Morris, R. E.; Serre, C. *Chem. Rev.* **2012**, *112*, 1232-1268.
6. Ranocchiari, M.; Bokhoven, J. A. *Phys. Chem. Chem. Phys.* **2011**, *13*, 6388-6396.

7. Coudert, F.X. *Chem. Mater.* **2015**, *27*, 1905-1916.
8. Loiseau, T.; Serre, C.; Huguenard, C.; Fink, G.; Taulelle, F.; Henry, M.; Bataille, T.; Férey, G. *Chem. Eur. J.* **2004**, *10*, 1373-1382.
9. Camacho, B. C. R.; Ribeiro, R. P. P. L.; Esteves, I. A. A. C.; Mota, J. P. B. *Sep. Purif. Technol.* **2015**, *141*, 150-159.
10. Cheng, Y.; Kondo, A.; Noguchi, H.; Kajiro, H.; Urita, K.; Ohba, T.; Kaneko, K.; Kanoh, H. *Langmuir* **2009**, *25*, 4510-4513.
11. Millange, F.; Walton, R. I. *Isr. J. Chem.* **2018**, *58*, 1019-1035.
12. Kondo, A.; Ohnishi, S.; Kajiro, H. *Nano Lett.* **2006**, *6*, 2581-2584.
13. Millange, F.; Serre, C.; Férey, G. *Chem. Commun.* **2002**, 822-823.
14. Serre, C.; Thouvenot, C. *J. Am. Chem. Soc.* **2002**, *124*, 13519-13526.
15. Devautour-Vinot, S.; Maurin, G.; Henn, F.; Serre, C.; Férey, G. *Phys. Chem. Chem. Phys.* **2010**, *12*, 12478-12485.
16. Yot, P. G.; Yang, K.; Guillerm, V.; Ragon, F.; Dmitriev, V.; Parisiades, P.; Elkaim, E.; Devic, T.; Horcajada, P.; Serre, C.; Stock, N.; Mowat, J. P. S.; Wright, P. A.; Férey, G.; Maurin, G. *Fluid Phase Equilib.* **2016**, *2016*, 4424-4429.
17. Volkringer, C.; Loiseau, T.; Guillou, N.; Férey, G.; Elkaim, E.; Vimont, A. *Dalton Trans.* **2009**, 2241-2249.
18. Chapman, K. W. *J. Am. Chem. Soc.* **2006**, *131*, 17546-17547.
19. Bennett, T. D.; Simoncic, P.; Moggach, S. A.; Gozzo, F.; Macchi, P.; Keen, D. A.; Tan, J. C.; Cheetham, A. K. *Chem. Commun.* **2011**, 47, 7983-7985.
20. Cao, S.; Bennett, T. D.; Keen, D. A.; Goodwin, A. L.; Cheetham, A. K. *Chem. Commun.* **2012**, 48, 7805-7807.
21. Li, W.; Probert, M. R.; Kosa, M.; Bennett, T. D.; Thirumurugan, A.; Burwood, R. P.; Parinello, M.; Howard, J. A.; Cheetham, A. K. *J. Am. Chem. Soc.* **2012**, *134*, 11940-11943.
22. Serra-Crespo, P.; Dikhtiarenko, A.; Stavitski, E.; Juan-Alcaniz, J.; Kapteijn, F.; Coudert, F. X.; Gascon, J. R. *Soc. Chem.* **2015**, *17*, 276-280.
23. Hu, Y. H.; Zhang, L. *Phys. Rev. B* **2010**, *81*.
24. Fan, W. W.; Cheng, Y.; Zheng, L. Y.; Cao, Q. E. *Chem. Eur. J.* **2020**, *26*, 2766-2779.

25. Zhou, W.; Wu, H.; Yildirim, T.; Simpson, J. R.; Walker, A. R. H. *Phys. Rev. B* **2008**, *78*.
26. Han, S. S.; Goddard, W. J. *Phys. Chem. C* **2017**, *111*, 15185-15191.
27. Bourg, L. B. *APL Mater.* **2014**, *2*, 124110.
28. Liu, Y. *J. Am. Chem. Soc.* **2008**, *130*, 11813-11818
29. Quadrelli, R.; Peterson, S. *Energy Policy* **2007**, *35*, 5938-5952.
30. Figueroa, J. D.; Fout, T.; Plasynski, S.; McIlvried, H.; Srivastava, R. D. *Int. J. Greenhouse Gas Control* **2008**, *2*, 9-20.
31. Bui, M.; Adjiman, C. S.; Bardow, A.; Anthony, E. J.; Boston, A.; Brown, S. *Energy Environ. Sci.* **2018**, *11*, 1062-1176.
32. Liu, J.; Thallapally, P. K.; McGrail, B. P.; Brown, D. R.; Liu, J. *Chem. Soc. Rev.* **2012**, *41*, 2308-2322.
33. Rehman, A.; Farrukh, S.; Hussain, A.; Pervaiz, E. *Energy Environ. Sci.* **2019**, *31*, 367-388.
34. Millward, A. R. *J. Am. Chem. Soc.* **2005**, *127*, 17998.
35. Farha, O. K.; Yazaydin, A. O.; Eryazici, I.; Malliakas, C. D.; Hauser, B. G.; Kanatzidis, M. G.; Nguyen, S. T.; Snurr, R. Q.; Hupp, J. T. *Nat. Chem.* **2010**, *2*, 944-948.
36. Li, J.; Ma, Y.; McCarthy, M. C.; Sculley, J.; Yu, J.; Jeong, H.; Balbuena, P. B.; Zhou, H. *Coord. Chem. Rev.* **2011**, *255*, 1791-1823.
37. Miller, S. R. *J. Am. Chem. Soc.* **2008**, *130*, 15967-15981.
38. Kishan, M. R.; Tian, J.; Thallapally, P. K.; Fernandez, C. A.; Dalgarno, S. J.; Warren, J. E.; McGrail, B. P.; Atwood, J. L. *Chem. Commun.* **2010**, *46*, 538-540.
39. Arstad, B.; Fjellvag, H.; Kongshaug, K. O.; Swang, O.; Blom, R. *Adsorpt. Sci. Technol.* **2008**, *14*, 755-762.
40. Hu, Y.; Liu, Z.; Xu, J.; Huang, Y.; Song, Y. *J. Am. Chem. Soc.* **2013**, *135*, 9287-9290.
41. Hobday, C. L.; Woodall, C. H.; Lennox, M. J.; Frost, M.; Kamenev, K.; Duren, T.; Morrison, C. A.; Moggach, S. A. *Nat. Commun.* **2018**, *9*, 1429.
42. Hu, Y.; Kazemian, H.; Rohani, S.; Huang, Y.; Song, Y. *Chem. Commun.* **2011**, *47*, 12694-12696.

43. Hu, Y.; Lin, B.; He, P.; Li, Y.; Huang, Y.; Song, Y. *Chem. Eur. J.* **2015**, *21*, 18739-18748.
44. Mao, H.; Xu, J.; Hu, Y.; Huang, Y.; Song, Y. *J. Mater. Chem. A* **2015**, *3*, 11976-11984.
45. Jiang, S.; Hu, Y.; Chen, S.; Huang, Y.; Song, Y. *Chem. Eur. J.* **2018**, *24*, 19280-19288.
46. Zhang, Y.; Wang, J.; Yan, X.; Liu, X.; Zhou, H.; Yuan, A. *Microporous Mesoporous Mater.* **2014**, *184*, 15-20.
47. Chen, S.; Lucier, B. E. G.; Boyle, P. D.; Huang, Y. *Chem. Mater.* **2016**, *28*, 5829-5846.
48. Liebermann, R. C. *High Pressure Res.* **2011**, *31*, 493-532.
49. Schettino, V.; Bini, R. *Chem. Soc. Rev.* **2007**, *36*, 869-880.
50. Song, Y.; Dong, Z. *Nanowires - Fundamental Research.* **2011**. Novel Pressure-Induced Structural Transformations of Inorganic Nanowires.
51. Walker, J. *Rep. Prog. Phys.* **1979**, *42*, 1605.
52. Mao, H. K. *J. Geophys. Res.* **1986**, *91*, 4673-4676.
53. Song, Z. D. *J. Phys. Chem. C* **2010**, *114*, 1782-1788.
54. Barthelet, K.; Marrot, J.; Ferey, G.; Riou, D. *Chem. Commun.* **2004**, 520-521.

Chapter 2

2 Discovering the High-Pressure Stability of and Pressure-Enhanced CO₂ Storage in MIL-53(Al) by *In Situ* Infrared Spectroscopy

2.1 Introduction

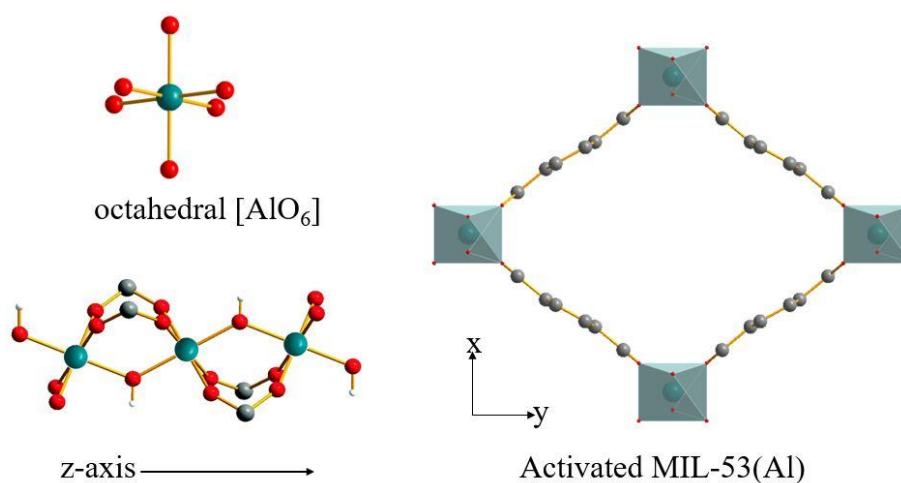


Figure 2.1 The wine-rack topology of MIL-53 (Al) (Al = green, O = red, H = white, C = grey).

As a rising class of porous crystalline materials, metal-organic frameworks (MOFs) are composed of metal ions/clusters connected through organic linkers to create open frameworks with channels or cages.¹ Attributed to their high surface area and larger pore volume, MOFs are now considered as the most promising gas adsorbent, including the primary greenhouse gases CO₂, CH₄, and so on.^{2,3} Nowadays, those MOFs featuring wine-rack topology draw increasing attention from chemists, such as MIL-53 (MIL = Matériaux de l'Institut Lavoisier) family.^{4,5} The topology of MIL-53 is depicted in Figure 2.1.⁶ The framework consists of octahedral MO₄(OH)₂ (M = Cr³⁺, Al³⁺, Fe³⁺, Sc³⁺, Ga³⁺, In³⁺) as secondary building units (SBUs), which are built up from a metal center (M) connected with two bridging OH groups and four oxygen atoms from four

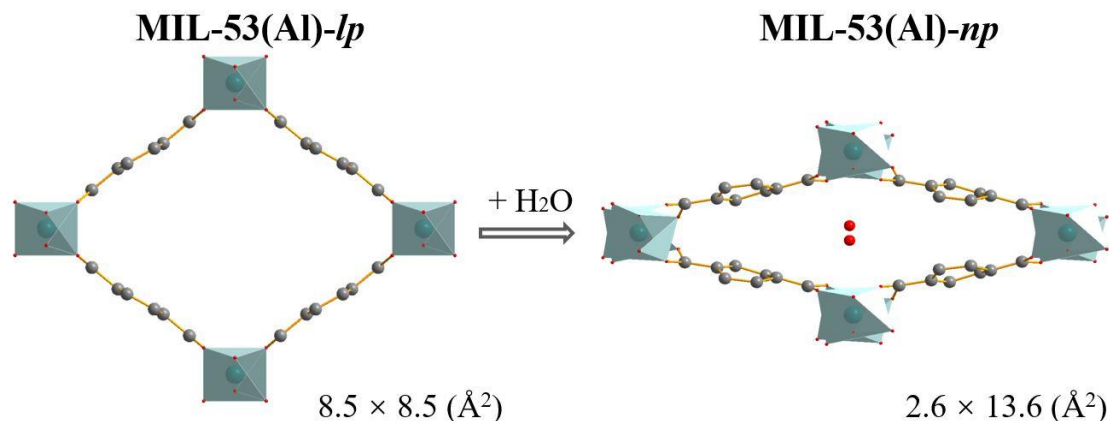


Figure 2.2 The reversible *lp* - *np* phase transition of MIL-53(Al) (octahedral $[\text{AlO}_6]$ = grey octahedra, O = red circles, C = grey circles) and adsorbed H_2O molecules locate in the center of the *np* channels.

benzenedicarboxylate (BDC) linkers. By sharing with two adjacent SBUs, these bridging hydroxyl oxygen atoms join metal-containing octahedra forming an infinite chain along z-axis of its crystalline structure.⁷ The MIL-53 family is well-known because of a crystal-to-crystal phase transition known as ‘breathing effect’, where the framework undergoes a reversible large pore (*lp*) to narrow pore (*np*) phase transition induced by guest molecules (such as H_2O , CO_2 , CH_4), pressure or temperature (see *Chapter 1.2* for more details).^{5,8,9,10} The as-made MIL-53(Al) has rhombic pores measuring $7.3 \times 7.7 \text{ (\AA}^2\text{)}$ and are filled with unreacted H_2BDC (benzenedicarboxylic acid) from the MOF preparation. After activation, the excess H_2BDC molecules are expelled out of the pores to form the *lp* phase MIL-53-*lp*, which features $8.5 \times 8.5 \text{ (\AA}^2\text{)}$ larger pores. MIL-53-*lp* captures H_2O molecules easily from open air at room temperature to create the *np* phase MIL-53-*np*, featuring $2.6 \times 13.6 \text{ (\AA}^2\text{)}$ narrow pores (Figure 2.2).⁹ This *lp* - *np* phase transition results in a decrease in its unit cell volume up to *ca.* 40%.¹¹ Most importantly, MIL-53(Al) shows an excellent CO_2 affinity: at 25 bar and 304 K, MIL-53(Al)-*lp* can adsorb 30.6 wt% of CO_2 ,¹² together with the high natural abundance of aluminum metal, MIL-53(Al) becomes the most practical CO_2 adsorbent among MIL-53 family. Additionally, most of the adsorption capacities of MIL-53 family were carried out under near ambient loading pressures (e.g. tens of bar).^{13,14,15} For example, Rallapalli *et al.* reported that methane storage capacity of MIL-53(Al) at 303 K and 35 bar is $186 \text{ cm}^3/\text{cm}^3$. Adsorption forms of

CO₂ on MIL-53(Al) at up to 100 mbar were studied by FTIR spectroscopy that shows CO₂ dimeric species are formed under high loading pressures.^{16,17} Moreover, many prior studies have demonstrated that high external compression in gigapascal level is one of the promising methods to improve the CO₂ adsorption performance of MOFs.^{18,19,20} Given that high-pressure behaviors of CO₂-loaded MIL-53(Al) remain unknown, we thus decided to apply high external compressions in gigapascal level on as-made, activated, and CO₂-loaded MIL-53(Al). Moreover, previous studies have demonstrated that MIL-53(Al) undergoes a *lp* to *np* phase transition at ~2 GPa.⁹ It is expected that high external pressures and the above-mentioned *lp* to *np* phase transition could trigger interesting intra- and/or inter-framework interactions in as-made, activated, and CO₂-loaded MIL-53(Al).

2.2 Experimental section

2.2.1 MOF preparation

As-made MIL-53(Al) was prepared through hydrothermal synthesis using a 23 mL Teflon-lined stainless-steel Parr autoclave as described in the literature.⁹ The starting chemicals aluminum nitrate nonahydrate ($\geq 98\%$) and terephthalic acid ($\geq 98\%$) were purchased from Sigma-Aldrich then used without purification. Aluminum nitrate nonahydrate (1.30 g, 6.10 mmol) and terephthalic acid (0.288 g, 1.73 mmol) were mixed in 5.0 mL of deionized water. After stirring for 30 minutes, the autoclave was sealed and heated up in an oven at 493 K for 3 days. The product was filtered and washed with deionized water for 3 times. The yielding white powdered solid was as-made MIL-53(Al). To activate MIL-53(Al), solvent exchange method was used to remove trapped terephthalic acid molecules. As-made MIL-53(Al) (0.5 g) was soaked in 10 mL of *N,N*-dimethylformamide (DMF) in the autoclave and then heated up at 423 K overnight (e.g., 12 h). The same procedure was repeated twice. Filtered sample was dried by heating at 472 K under dynamic vacuum (≤ 1 mbar) for 6-8 h to remove DMF molecules from the framework. The phase purities and identities of the samples were confirmed using PXRD (see *Appendix A* for the details of the instrument we used and plotted PXRD patterns). Then the activated MIL-53(Al) was transferred to a Micromeritics ASAP 2020 porosity

analyzer to measure its N₂ surface area isotherm at a temperature of 77 K. Compared to literature (1300 m²/g),¹² the BET (Brunauer-Emmett-Teller) surface area of my sample is 1124.5 m²/g, which is acceptable.

2.2.2 Cryogenic CO₂ loading

Cryogenic loading was used to load CO₂ into a diamond anvil cell (DAC) containing activated MIL-53(Al). The activated MIL-53(Al) with some ruby chips was pre-loaded to the sample chamber of the DAC, and then we cooled down the cell in liquid N₂ (L-N₂) bath. To make sure the temperature of the DAC is below the melting point of dry ice, DAC was soaked in the L-N₂ bath for 4 min before CO₂ loading. Then we condensed gaseous CO₂ on the top of the loaded sample. To trap CO₂ inside the sample chamber, we sealed the DAC right away and applied a minimum pressure (i.e., 0.1 - 0.5 GPa) on it. In the end, the DAC was placed on the bench for ~1 h to warm up to room temperature.

2.2.3 High-pressure *in situ* IR spectroscopy

To generate high pressures, we used a DAC with type II diamonds for *in situ* IR spectroscopy. The culet size of the diamonds is 600 μm. The gasket was pre-indented to a thickness of 40 - 50 μm and then a sample chamber in the diameter of 260 μm was drilled in the center of the pre-indented mark.

The customized IR micro-spectroscopy system (see *Chapter 1.5.2.* for details) was employed. The background spectrum of the diamonds was recorded and subtracted for calibration purposes. Therefore, all the IR spectra presented in this thesis were recorded and calibrated at room temperature.

2.3 Results and discussion

2.3.1 IR spectra of MIL-53(Al) at ambient pressure

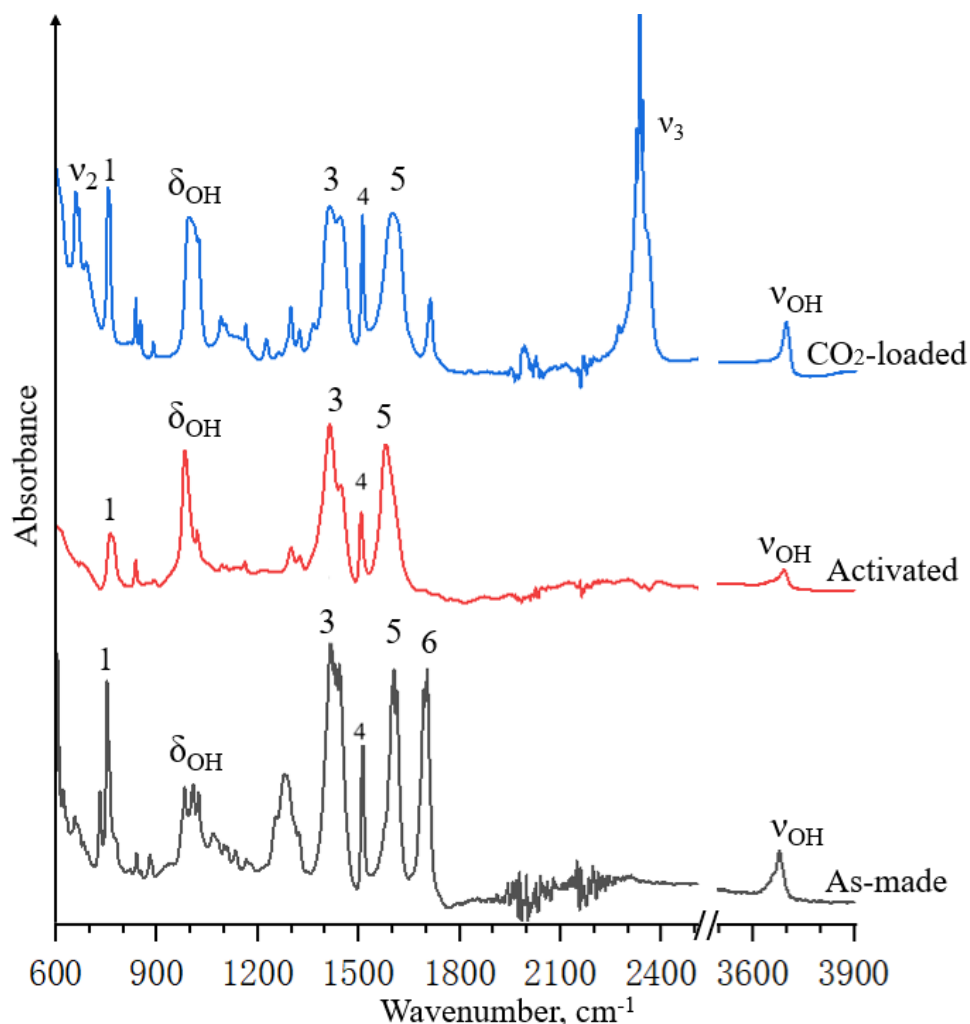


Figure 2.3 IR spectra of as-made, activated and CO₂-loaded MIL-53(Al) at ambient pressure.

The IR spectra of as-made, activated and CO₂-loaded MIL-53(Al) under near ambient pressure are presented in Figure 2.3. Basically, most of the absorption peaks for all the samples are attributed to the vibrations of the organic linkers. The spectra of as-made, activated, and CO₂-loaded MIL-53(Al) samples highly agree with prior studies.^{16,17} The complex nature of the MOF framework makes the complete assignment of its IR bands difficult. Nevertheless, the majority absorption peaks of the spectra are assigned as shown in Table 2.1 below. Specifically, the band at 753 cm⁻¹ (labelled as peak 1) is

Table 2.1 Assignments for the characteristic IR modes of activated, as-made and CO₂-loaded MIL-53(Al)

IR modes	Frequencies (cm ⁻¹)				Assignments
	Activated MIL-53(Al)	As-made MIL-53(Al)	CO ₂ -loaded MIL-53(Al)	Ref 16,17	
1	753	750	758	735	C-COO out-of-plane bending
δ_{OH}	982	990	993	977	Al-OH-Al deformation modes
3	1417	1420	1418	1424	O-C-O symmetric stretching
4	1507	1515	1509	1509	C=C stretching and CCH bending
5	1597	1600	1604	1576	O-C-O asymmetric stretching
6	-	1695	-	1684	C=O stretching Of free H ₂ BDC
ν_{OH}	3692	3677	3692	3665	O-H stretching
ν_2	-	-	664	667	CO ₂ bending
ν_3	-	-	2340	2349	CO ₂ asymmetric stretching

attributed to the C-COO out-of-plane bending. Mode δ_{OH} at 982 cm⁻¹ is assigned as deformation vibrations of bridging hydroxyl (Al-OH-Al) groups. Those peaks between 1000 - 1200 cm⁻¹ are associated with benzene ring (C-C-H) in-plane bending. And peak 3 and 5 at around 1417 and 1597 cm⁻¹ are owing to symmetric and asymmetric stretching of the carboxylate (O-C-O) groups connected to aluminium atoms. Peak 4 at 1507 cm⁻¹ is attributed to the C=C stretching and CCH bending of benzene rings. For as-made sample, peak 6 shows at 1695 cm⁻¹, owing to C=O stretching of free H₂BDC (terephthalic acid) molecules inside the pores of the framework. Also, three spectra all show a peak ν_{OH} at ~3700 cm⁻¹ characteristic of the bridging hydroxyl groups. As for CO₂-loaded MIL-

53(Al), the two extra sharp peaks at 670 and 2335 cm^{-1} are associated with the CO_2 bending mode (ν_2) and CO_2 asymmetric stretching mode (ν_3), respectively, indicating the successful CO_2 loading, while the CO_2 symmetric stretching mode (ν_1) is not IR active.

2.3.2 High-pressure study of as-made MIL-53(Al)

As presented in Figure 2.4 (A), the IR spectra of the as-made MIL-53(Al) were recorded upon compression all the way to 10.07 GPa. Compared to the activated MOFs, the IR spectra of as-made MOFs are always more complicated, owing to the trapped free H_2BDC molecules inside the channels, in this particular case, resulting in three multiple peaks assigned to H_2BDC and labelled as peak 3, 5 and 6 in Figure 2.4 with their assignments listed in Table 2.1. In addition, the ν_{OH} mode shows at 3677 cm^{-1} under ambient pressure. Upon compression, it significantly red shifts to 3640 cm^{-1} at 8.43 GPa and then completely disappears at highest pressure 10.07 GPa. Given that red-shifted ν_{OH} mode of MIL-53 is often attributed to the formation of hydrogen bonds,¹⁷ the significantly red-shifted ν_{OH} upon compression can be interpreted as that pressures enhance inter-framework hydrogen bonding interactions between the OH groups of the framework and free H_2BDC molecules. Also, increasing pressure leads to gradual broadening of all IR peaks, attributed to the pressure-induced amorphization. Compared with ambient spectrum, the IR spectrum at 9.22 GPa significantly broadened, but most of the characteristic peaks remain, indicating that the framework is still intact. However, at the highest pressure of 10.07 GPa, the IR profile is barely recognizable, at this point, the framework becomes completely amorphous.

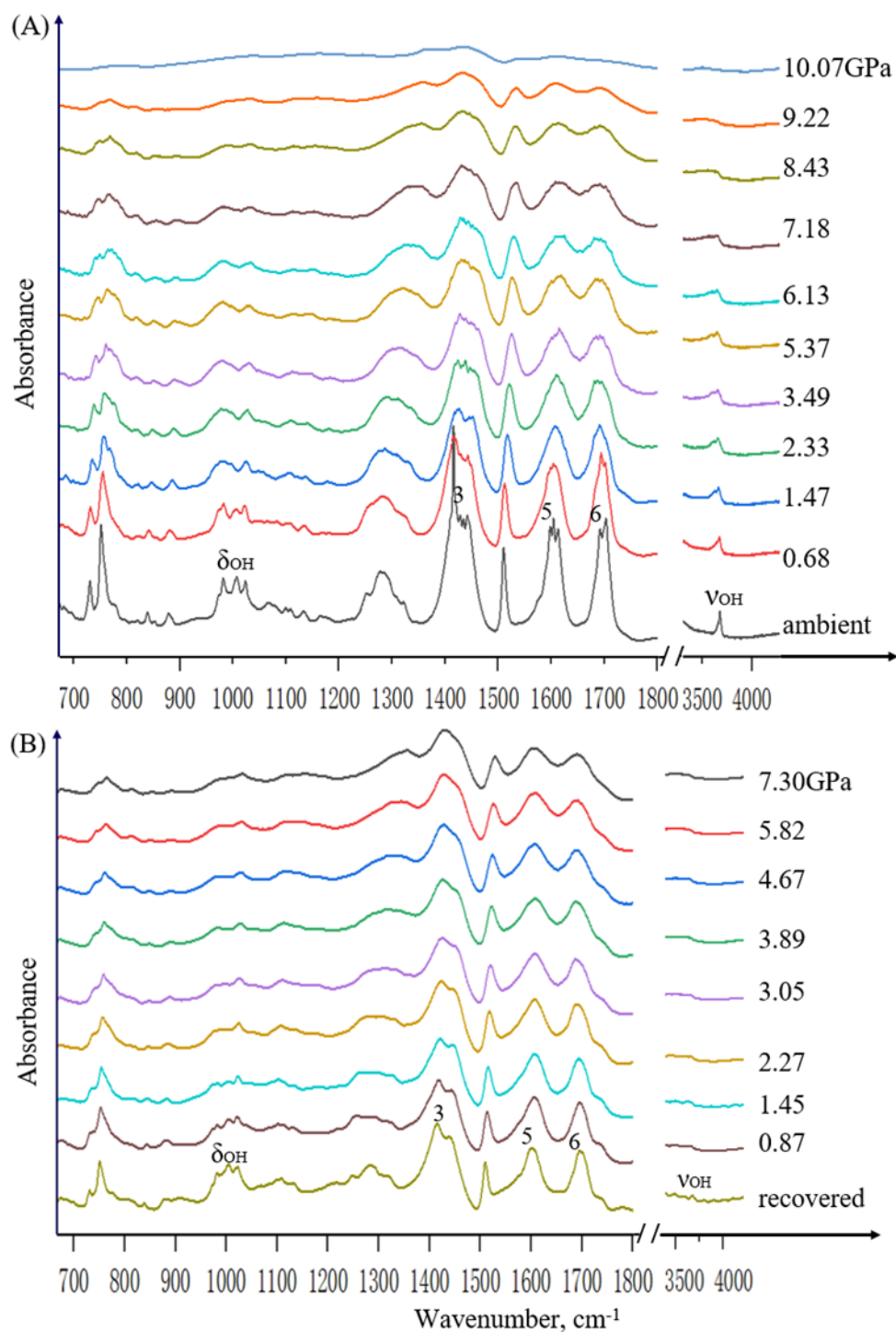


Figure 2.4 The selected IR spectra of as-made MIL-53(Al) upon compression (A) and decompression (B).

As for decompression, the IR spectra of as-made MIL-53(Al) were recorded by releasing the pressure gradually to ambient conditions. Upon complete decompression,

most of the IR peaks are recovered but less resolved compared with the modes in the ambient profile, which could result from that sample in the chamber becomes thinner under high pressures. Also, we noticed that while ν_{OH} , the mode that underwent remarkable changes upon compression, are barely recovered, merely a very weak band reappears at 3677 cm^{-1} , indicating that the bridging OH groups are much more sensitive to pressure than other parts of the framework. Given that the recovered IR profile remains characteristic of MIL-53, it is believed that this framework has survived the compression up to 10.07 GPa with minor modifications of local structures.

2.3.3 High-pressure study of activated MIL-53(AI)

It has been demonstrated by PXRD that the empty wine-rack framework of activated MIL-53(AI) exhibits remarkable flexibility under high pressures ($\sim 2\text{ GPa}$) by undergoing the lp to np phase transition.⁵ Therefore, it is worthwhile to explore the intrinsic pressure behavior of activated MIL-53(AI) by IR spectroscopy with the selected spectra shown in Figure 2.5. Upon compression, most of the changes occur when the pressure increased from 1.06 to 2.39 GPa, which is attributed to the above-mentioned lp to np transition. According to previous studies, when the hydroxyl groups are involved in hydrogen bonding, its deformation mode (δ_{OH}) at around 980 cm^{-1} undergoes a shift to higher frequency ($+40\text{ cm}^{-1}$) while its stretching mode (ν_{OH}) at $\sim 3700\text{ cm}^{-1}$ exhibits a red shift (-38 cm^{-1}).¹⁷ In our case, there are no guest molecules in the channels of the framework and the δ_{OH} appears as a doublet (labelled as $\delta_{\text{OH-1}}$ and $\delta_{\text{OH-2}}$) at 0.23 GPa. Thus, the mode $\delta_{\text{OH-1}}$ at lower frequency (982 cm^{-1}) represents normal OH groups while the $\delta_{\text{OH-2}}$ (at 1018 cm^{-1}) is assigned to OH units upon intra-framework hydrogen bonding (Figure 2.6). With increasing pressure, the intensity of mode $\delta_{\text{OH-1}}$ decreases suddenly, whereas the intensity of $\delta_{\text{OH-2}}$ increases, indicating that high pressure facilitates the formation of hydrogen bonds within the framework. Secondly, with increasing pressure to 2.39 GPa, the ν_{OH} modes split into two peaks: $\nu_{\text{OH-1}}$ (at 3660 cm^{-1}) and $\nu_{\text{OH-2}}$ (at 3616 cm^{-1}) in Figure 2.5. Thus, $\nu_{\text{OH-2}}$ is assigned to OH groups forming hydrogen bonding with neighboring carboxylate oxygen. Then $\nu_{\text{OH-2}}$ significantly red shifts upon further compression, suggesting that some of the O-H bond are further weakened, arising from

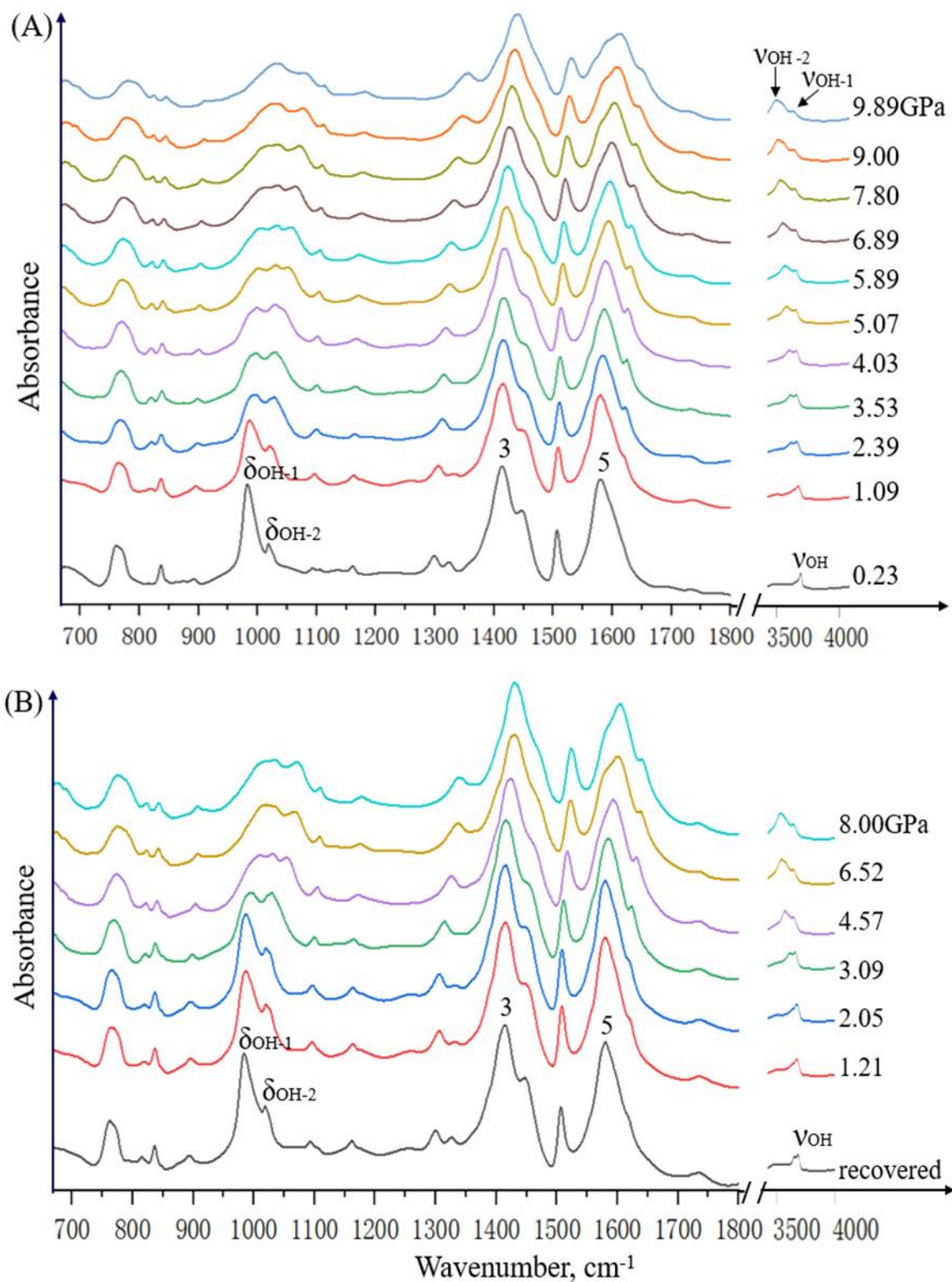


Figure 2.5 The selected IR spectra of activated MIL-53(Al) upon compression (A) and decompression (B) in the spectral region of 650 - 1800 and 3450 - 4000 cm^{-1} .

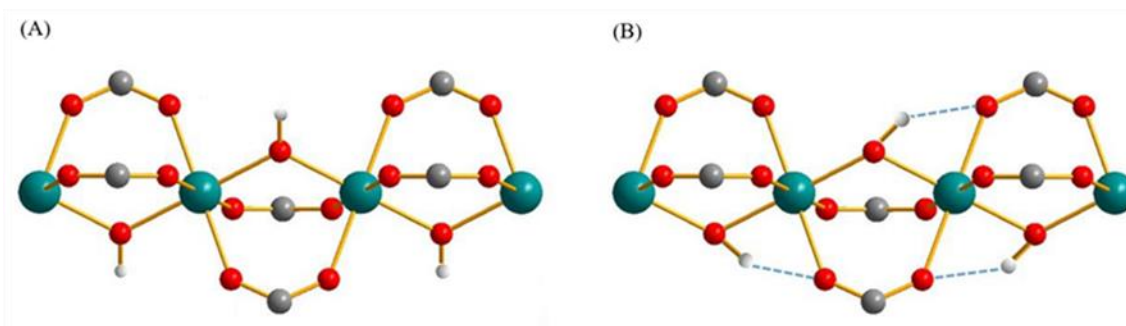


Figure 2.6 The comparison of the local structure of activated MIL-53(Al) at ambient pressure (A) and at high pressure (B) with intra-framework H-bonds labelled as dashed lines (Al = dark green, O = red, H = white, C = grey).

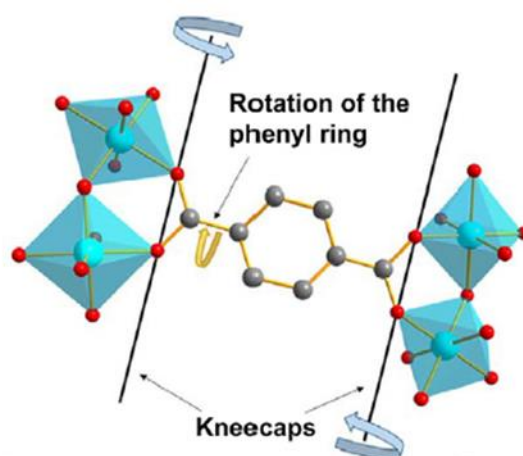


Figure 2.7 An illustrate of the 'kneecap' motion of activated MIL-53 (M = light blue, O = red, C = grey).^{6, 21}

shortened hydrogen bonds. That is, pressure-induced intra-framework hydrogen bonds are enhanced and shortened upon compression. The *lp* to *np* phase transition of the framework and weakening of the OH groups make this possible (shown in Figure 2.6). The changes of bonds length of Al-O and O-H upon compression would be necessary to support the speculation. However, previous high-pressure *in situ* PXRD studies of MIL-53(Al) merely discussed the changes of the pore size and unit cell volume. Further compression leads to further broadening of all the IR modes, but within 9.89 GPa, the IR profiles remain characteristic of MIL-53(Al). Compared with the spectrum of as-made sample at 10.07 GPa which is significantly broadened, activated MIL-53(Al) is more

stable than as-made MIL-53(Al) in a broad pressure region. However, in general, as-made MOFs always exhibit higher stability than activated MOFs, since occupied channels can resist higher pressures than empty ones. The reason behind this unusual phenomenon could be that the flexibility of the framework makes the activated MIL-53(Al) more tolerable to pressures. Previous studies have demonstrated that the flexibility of the framework is attributed to the ‘kneecap-like’ motion of the O-O axis with rotation of the phenyl ring as illustrated in Figure 2.7.^{6,21}

Moreover, we noticed that the OH groups exhibit higher pressure-sensitivity than other parts of the framework. The frequency plots of selected IR modes upon compression are depicted in Figure 2.8, along with their pressure dependencies listed in Table 2.2. The O-C-O modes (modes 3 and 5) exhibit regular pressure-induced blue shifts and slightly stiffening. Consequently, their pressure dependencies are small in magnitude ($\sim 3 \text{ cm}^{-1}/\text{GPa}$). In contrast, because of the formation of intra-framework hydrogen bonds, δ_{OH} blue shifts with the pressure dependence greater than $6 \text{ cm}^{-1}/\text{GPa}$. Also, at 2 - 10 GPa, $\nu_{\text{OH-2}}$ red shifts greatly ($-16.0 \text{ cm}^{-1}/\text{GPa}$) compared with the O-C-O

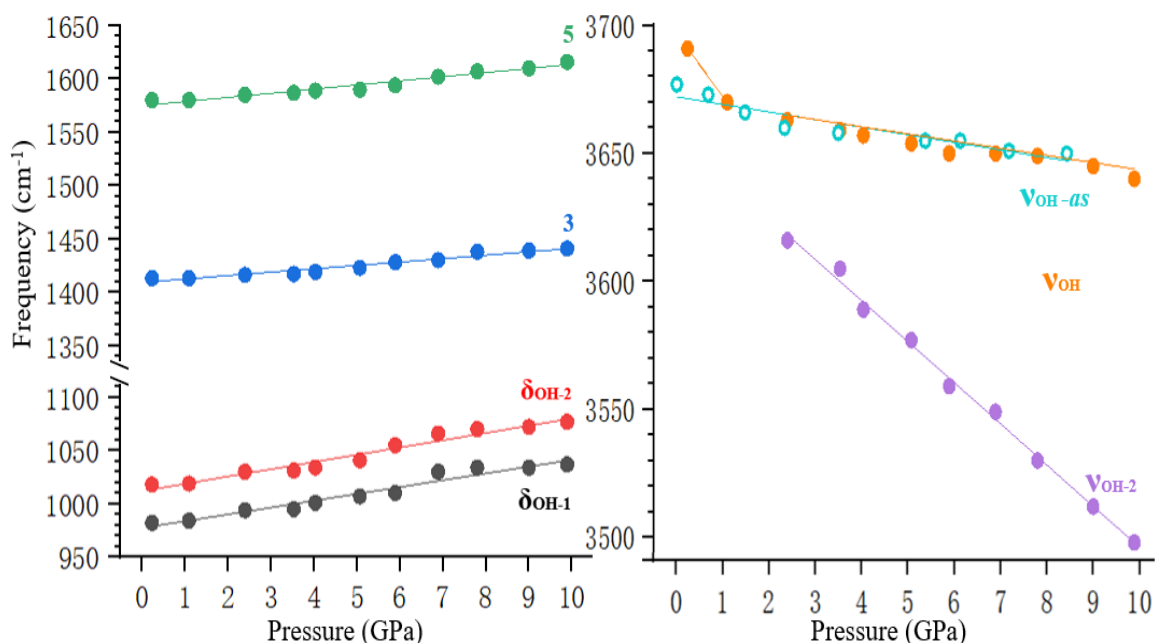


Figure 2.8 Frequency plots of selected IR modes of activated MIL-53(Al) (solid circles) and as-made MIL-53(Al) (the hollow circle) as a function of pressure in the spectral region of 950-1100, 1350-1650 cm⁻¹(A) and 3450-3750 cm⁻¹(B).

Table 2.2 Pressure dependence (dv/dP , $\text{cm}^{-1}/\text{GPa}$) of IR modes of activated MIL-53(Al).

Mode	Frequency (cm^{-1})	Pressure dependence ($\text{cm}^{-1}/\text{GPa}$)	
$\delta_{\text{OH-1}}$	982	6.4	
$\delta_{\text{OH-2}}$	1018	6.8	
3	1417	3.2	
5	1597	3.9	
$\nu_{\text{OH-2}}$	3616	-16.0 (2 - 10 GPa)	
ν_{OH}	3692	-24.0 (0 - 1 GPa)	-2.8 (2 - 10 GPa)
$\nu_{\text{OH-as}}$	3677	-2.9	

modes of its framework and OH stretching mode of as-made MIL-53(Al) (labelled as $\nu_{\text{OH-as}}$), indicating that *np* phase (> 2 GPa) of MIL-53(Al) facilitates the pressure-enhanced intra-framework interactions.

Upon decompression, compared to as-made MIL-53(Al), almost all the bands recovered with only the ν_{OH} modes remaining slightly split. Overall, *in situ* high-pressure study of activated MIL-53(Al) unveils the outstanding stability of the framework and pressure-induced intra-framework hydrogen bonds.

2.3.4 High-pressure study of CO₂-loaded MIL-53(Al)

MOFs is the most promising adsorbents for greenhouse gases. The dynamic motion of CO₂ inside the framework of MIL-53(Al) has been investigated by Zhang *et al.*,⁶ which demonstrated that the CO₂ binding sites in MIL-53(Al) are positioned around the bridging OH units (shown in Figure 2.9). Here, we presented the first high-pressure (in gigapascal range) studies of CO₂ adsorption behaviors of MIL-53(Al).

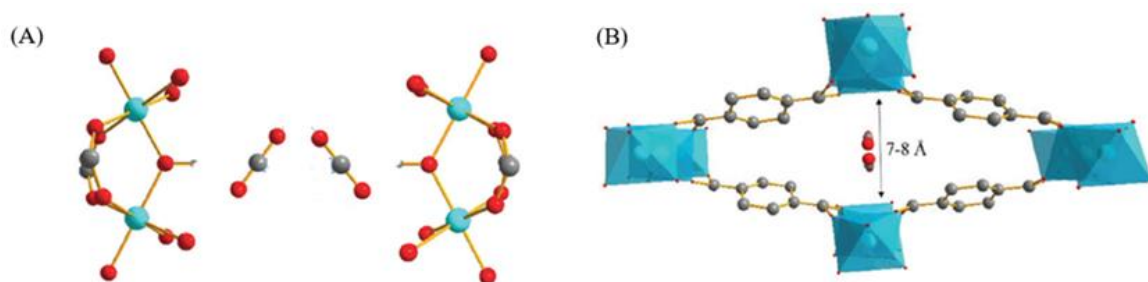


Figure 2.9 Illustrations of CO₂ adsorption sites in MIL-53(Al) (Al = light blue, O = red, H = white, C = grey).⁶

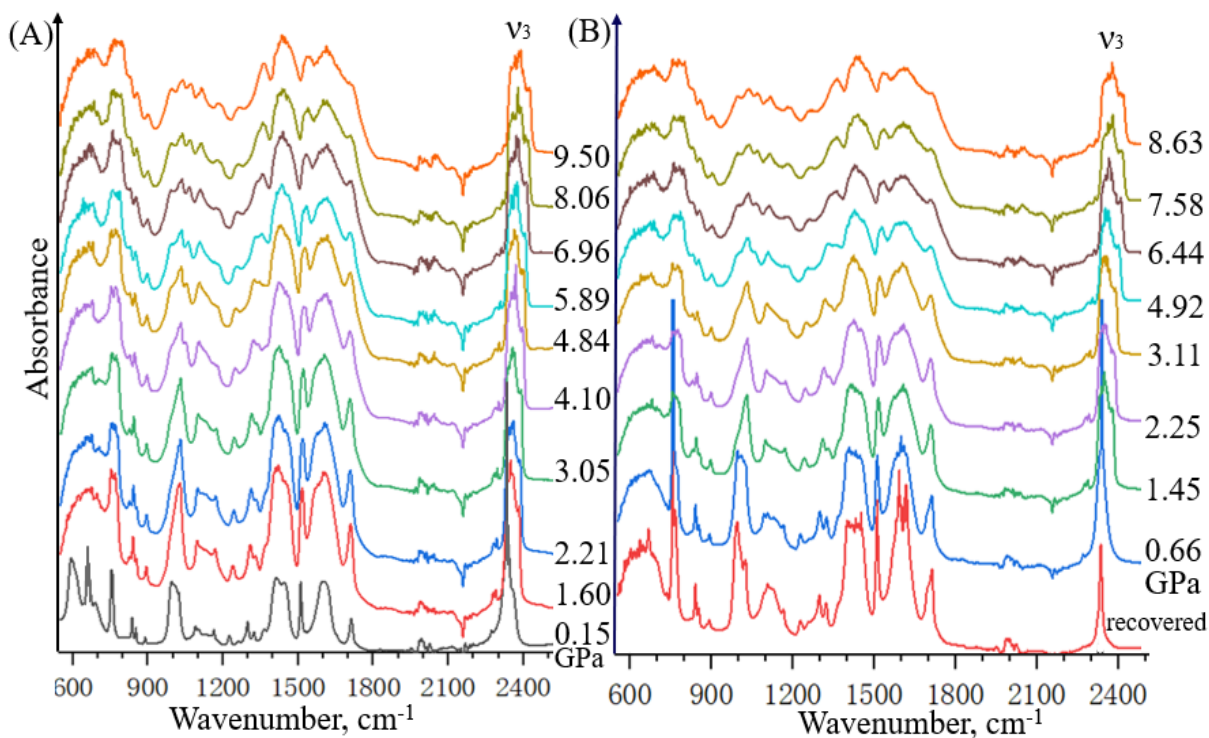


Figure 2.10 Selected IR spectra of CO₂-loaded MIL-53(Al) upon compression (A) and decompression (B) in the frequency region of 550-2450 cm⁻¹.

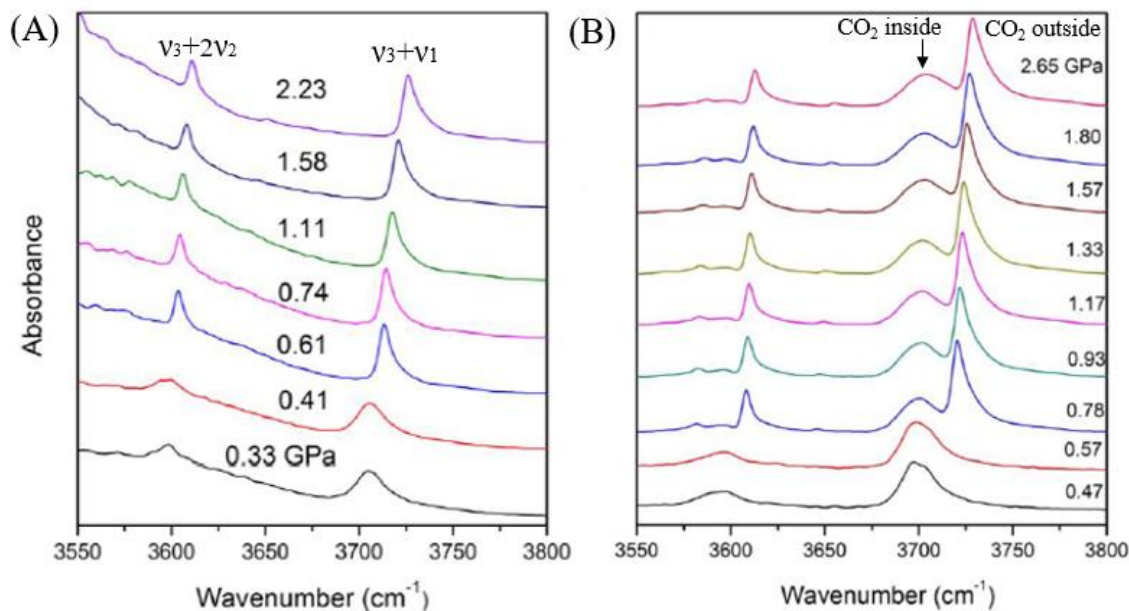


Figure 2.11 IR spectra upon compression of pure CO₂ (A) and CO₂-loaded ZIF-8 (B) in the spectral region of the CO₂ combination modes.¹³

Figure 2.10 shows the IR spectra of CO₂-loaded MIL-53(Al) upon compression up to 9.50 GPa and then decompressed to ambient pressure. Owing to the saturated IR absorption of ν_3 mode of CO₂, it is difficult to analyze its adsorption performance directly. Many previous work has shown that the CO₂ combination modes ($\nu_3 + 2\nu_2$ at ~ 3600 cm⁻¹ and $\nu_3 + \nu_1$ at ~ 3700 cm⁻¹) are useful for investigating the interactions between CO₂ and MOFs.^{18,19,20} For instant, Figure 2.11 (A) shows the combination modes of pure CO₂.¹⁵ As we can see, the combination modes sharpen and blue shift suddenly when pressure increased from 0.41 to 0.61 GPa, because CO₂ undergoes a phase transition from liquid to solid at 0.6 GPa and room temperature. As for CO₂-loaded ZIF-8 illustrated in Figure 2.11 (B), the $\nu_3 + \nu_1$ mode splits into two peaks when pressure > 0.6 GPa, suggesting that there are two types of CO₂: the lower-frequency component represents adsorbed CO₂ inside the framework, while the higher-frequency peak is attributed to the solid CO₂ outside the framework.¹⁸ However, in our case, the situation is more complicated, since there is a ν_{OH} main peak appearing at ~ 3700 cm⁻¹ overlapping with the $\nu_3 + \nu_1$ modes. We observed the significant changes at the spectral region of 3600 - 3780 cm⁻¹ upon compression. To assist in analysis, the selected IR spectra in this frequency region were enlarged and are shown in Figure 2.12.

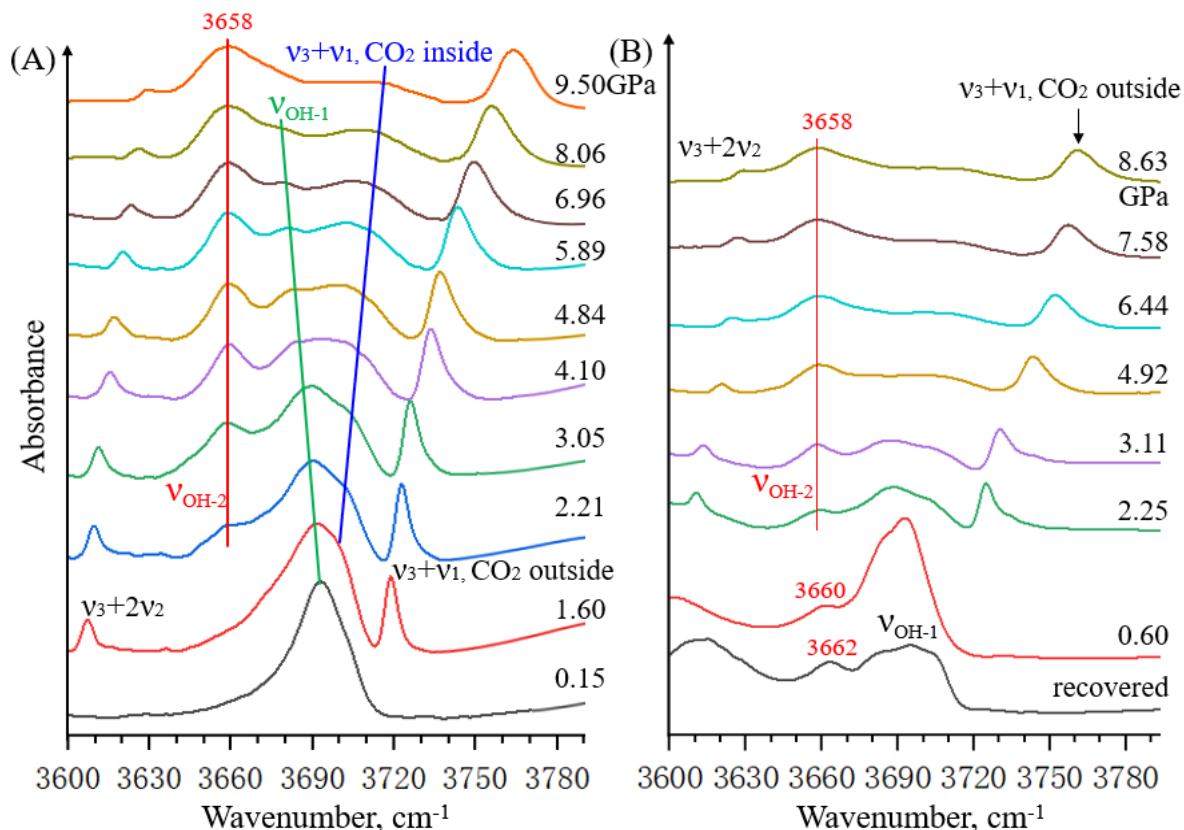


Figure 2.12 IR spectra of CO₂-loaded MIL-53(Al) upon compression (A) and decompression (B) in the frequency region 3600 - 3780 cm⁻¹.

For compression, only one asymmetric peak is observed at 3690 cm⁻¹ under 0.15 GPa. According to previous studies, it is highly possible that the asymmetric peak results from overlapped ν_{OH} of the framework and $\nu_3 + \nu_1$ mode of CO₂.^{16,18} Given that there is no solid CO₂ existing at 0.15 GPa and room temperature, the shoulder on the right-hand side of the peak at 3690 cm⁻¹ in Figure 2.12 represents $\nu_3 + \nu_1$ mode of CO₂ (including the adsorbed CO₂, if any, and the CO₂ outside the framework). At 1.60 GPa, $\nu_3 + \nu_1$ mode of adsorbed CO₂ appears as the lower-frequency component (labelled as ' $\nu_3 + \nu_1$, CO₂ inside') and still overlaps with ν_{OH} , while CO₂ outside the framework becomes solid and results in the appearance of the new peak in higher frequency at ~3720 cm⁻¹ ($\nu_3 + \nu_1$, CO₂ outside). In another word, at 1.60 GPa, the asymmetric peak at ~3690 cm⁻¹ represents ν_{OH} mode and $\nu_3 + \nu_1$ mode of CO₂ inside the framework. With increasing pressures ($P > 1.60$ GPa), in Figure 2.12, the asymmetric peak at ~3690 cm⁻¹ broadens significantly and splits

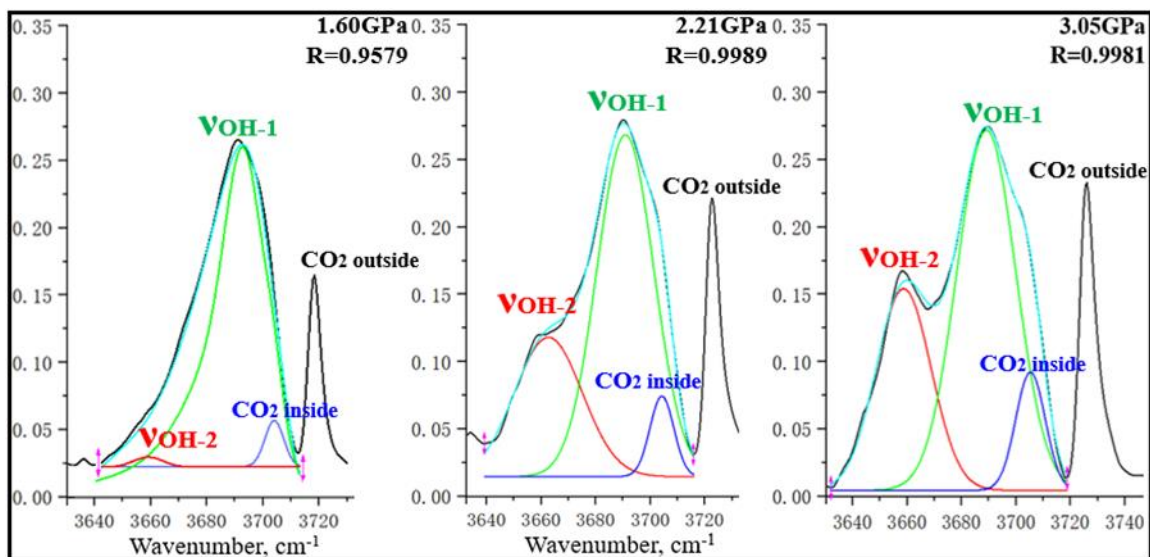


Figure 2.13 Deconvoluted IR spectra of CO₂-loaded MIL-53(Al) at 1.60, 2.21, and 3.05 GPa in the spectral region of the CO₂ combination modes.

Table 2.3 Peak area of ν_{OH} and $\nu_3 + \nu_1$ modes under different pressures in CO₂-loaded MIL-53(Al).

Mode \ Pressure	1.60 GPa	2.21 GPa	3.05 GPa
ν_{OH-2}	0.90	3.85	3.98
$\nu_3 + \nu_1$, CO ₂ inside	0.52	0.78	1.18

once again, attributed to the red-shifted ν_{OH} (labelled as green line) and blue-shifted $\nu_3 + \nu_1$ mode of CO₂ inside (blue line). Moreover, we noticed that another peak appears at 3658 cm⁻¹ ($P \geq 2.21$ GPa) and remains in constant wavenumber with increasing pressures (red line). Because of the above-mentioned lp to np transition at ~ 2 GPa,⁵ CO₂ molecules are adsorbed in np of the framework when $P \geq 2.21$ GPa. Given that the CO₂-occupied np phase of MIL-53(Al) features much less compressibility and flexibility,²² this new peak with constant wavenumber (3658 cm⁻¹) can be interpreted as that the rigid framework protects the adsorbed CO₂ from pressure-induced stiffening. Therefore, it is believed that this new peak at 3658 cm⁻¹ represents some OH units upon hydrogen

bonding with adsorbed CO₂ and thus is labelled as $\nu_{\text{OH-2}}$ in Figure 2.12. Also, the intensity of $\nu_{\text{OH-2}}$ mode increases with pressure increasing from 1.60 to 3.05 GPa, indicating the pressure-enhanced CO₂ adsorption of MIL-53(Al). The second evidence of pressure-enhanced CO₂ adsorption presents via deconvoluted IR spectra of CO₂-loaded MIL-53(Al) at 1.60 GPa, 2.21 GPa and 3.05 GPa shown in Figure 2.13. The deconvoluted peaks at $\sim 3690 \text{ cm}^{-1}$ (blue peaks) represent the $\nu_3 + \nu_1$ mode of CO₂ inside the framework. The adsorption quantity of CO₂ under selected pressures is determined by the integration of peak areas and listed in Table 2.3. It is obvious that the pressures enhance the migration of CO₂ into the framework by comparing the peak area of mode $\nu_3 + \nu_1$ of CO₂ inside (blue peak) with increasing pressure. Specifically, its peak area is doubled (from 0.52 to 1.18) upon compression. In addition, the deconvoluted peaks at $\sim 3660 \text{ cm}^{-1}$ (red peaks) are attributed to $\nu_{\text{OH-2}}$ (OH groups upon hydrogen bonding with adsorbed CO₂). The significantly increased peak area of $\nu_{\text{OH-2}}$ demonstrates the pressure-enhanced CO₂-framework interactions via hydrogen bonding. Moreover, all the peaks significantly broaden with further compression (Figure 2.10 (A)). At the highest pressure of 9.50 GPa, the spectrum remains recognized, indicating the extraordinary stability of CO₂-loaded MIL-53(Al).

Upon decompression from 8.63 GPa to 2.25 GPa, all bands are found to be reversible, as shown in Figure 2.10 (B). When releasing the pressure from 2.25 GPa to 0.60 GPa, significant changes were observed, which can be interpreted as that the solid CO₂ outside the framework melted, causing that the split $\nu_3 + \nu_1$ mode merged into one peak and then overlapped with the ν_{OH} mode. Therefore, in Figure 2.12 (B) the ν_{OH} mode of the framework and $\nu_3 + \nu_1$ mode of CO₂ (including the CO₂ inside and CO₂ outside the framework) overlap together and appear as an asymmetric peak at $\sim 3700 \text{ cm}^{-1}$ under 0.6 GPa. When the pressure is completely released, the intensity of the asymmetric peak at $\sim 3700 \text{ cm}^{-1}$ drops significantly, indicating that most CO₂ outside the framework was released to the air. However, the $\nu_{\text{OH-2}}$ mode remains at 3662 cm^{-1} , along with the ν_3 of CO₂ in the recovered spectrum of Figure 2.10 (B), suggesting that some of CO₂ molecules are still adsorbed in the framework. Overall, high pressures (up to 9.50 GPa)

enhanced the interactions between CO₂ and the bridging OH groups of the framework and pressure-induced CO₂ storage was observed upon compression.

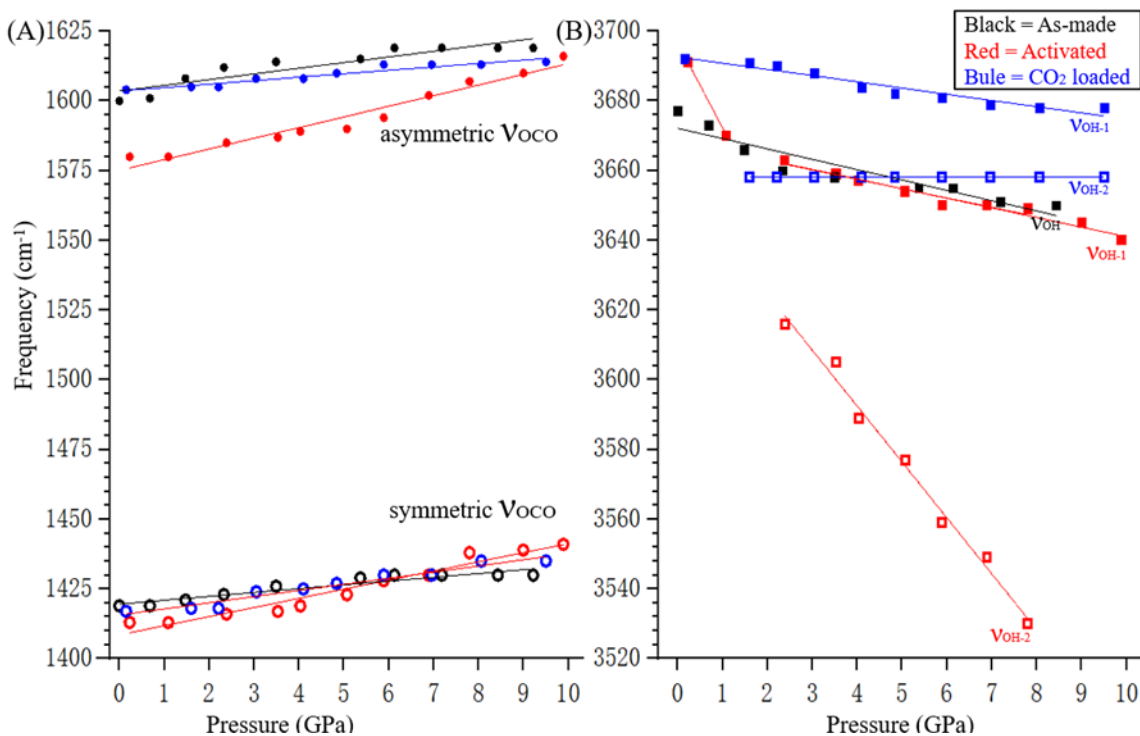


Figure 2.14 The comparison of the frequency plots of selected IR modes of as-made (black), activated (red) and CO₂ loaded (blue) MIL-53(Al) as a function of pressure in the spectral region of 1400-1625 cm⁻¹(A) and 3520-3700 cm⁻¹(B).

2.3.5 Comparison of high-pressure behaviors of as-made, activated, and CO₂ -loaded MIL-53(Al)

To compare the high-pressure behaviors of the three MOF systems in the pressure region of 0 - 10 GPa, the frequency plots of selected IR modes of as-made, activated and CO₂ loaded MIL-53(Al) as a function of pressure are presented in Figure 2.14, along with their pressure dependences (dv/dP , cm⁻¹/GPa) listed in Table 2.4. Firstly, compared to as-made and CO₂ loaded MIL-53(Al), symmetric and asymmetric v_{OCO} modes of activated MIL-53(Al) feature highest pressure-sensitivity, evidenced by their largest pressure dependences (> 3 cm⁻¹/GPa). That is because activated MIL-53(Al) with empty channels features more compressibility and flexibility. In contrast, both as-made and CO₂ loaded MIL-53(Al) feature occupied-channels. As a result, their frameworks are less

compressible (1 - 2 $\text{cm}^{-1}/\text{GPa}$). Secondly, OH unit of as-made MOF (black) shows less complex pressure-induced behavior, which does not split but exhibit slight red shift ($-2.97 \text{ cm}^{-1}/\text{GPa}$) upon compression, indicating the relatively weak interactions between OH groups and free H_2BDC molecules. In contrast, OH units of both activated and CO_2 loaded MIL-53(Al) split, which can be attributed to the pressure-enhanced hydrogen bonding interactions. To be specific, the pressure-induced intra-framework hydrogen bonds are formed in activated MOF between OH groups and octahedral $[\text{AlO}_6]$, results in the split of its ν_{OH} . Thus, its $\nu_{\text{OH-2}}$ assigned to those OH groups upon hydrogen bonding greatly red shifts ($-16.04 \text{ cm}^{-1}/\text{GPa}$) upon compression. For OH groups of CO_2 -loaded MOF, some of them interacts strongly with adsorbed CO_2 ($\nu_{\text{OH-2}}$), while the rest of them might be engaged in weak inter-/intra-framework interactions ($\nu_{\text{OH-1}}$). As a result, the ν_{OH} of CO_2 -loaded MIL-53(Al) split but slightly influenced by increasing pressures.

Table 2.4 The comparison of pressure dependence (dv/dP , $\text{cm}^{-1}/\text{GPa}$) of selected IR modes of as-made, activated and CO_2 loaded MIL-53(Al).

Mode		Frequency (cm^{-1})	Pressure dependence ($\text{cm}^{-1}/\text{GPa}$)		
symmetric ν_{CO}	as-made	1420	1.36		
	activated	1417	3.28		
	CO_2 loaded	1418	2.20		
asymmetric ν_{CO}	as-made	1600	2.04		
	activated	1597	3.82		
	CO_2 loaded	1604	1.23		
ν_{OH}	as-made		3677		-2.97
	activated	$\nu_{\text{OH-1}}$	3692	-24.42 (0 - 1 GPa)	-2.75 (2 - 3 GPa)
		$\nu_{\text{OH-2}}$	3616	-16.04	
	CO_2 loaded	$\nu_{\text{OH-1}}$	3692	-1.78	
		$\nu_{\text{OH-2}}$	3658	0	

2.4 Conclusion

In conclusion, the high-pressure behaviors of as-made and activated MIL-53(Al) as well as the interactions between CO₂ molecules and the framework were revealed by *in situ* IR spectroscopy. Pressures-induced inter-framework hydrogen bonds between the OH groups of as-made MIL-53(Al) and free H₂BDC molecules were observed. Secondly, activated MIL-53(Al) exhibited remarkable stability in a broad range of pressure, resulting from the flexibility of its empty wine-rack channels. Also, pressure-induced intra-framework hydrogen bonds were developed between OH groups and octahedral [AlO₆]. Thirdly, structural modifications of as-made and activated MIL-53(Al) were irreversible in the pressure range of 0 - 10 GPa. That is because their OH groups remained involved in hydrogen bonding interactions without applied pressures, suggesting the high pressure-sensitivity of the bridging OH units. Finally, for CO₂-loaded MIL-53(Al), pressure-enhanced CO₂ adsorption was observed. When the pressure recovered to ambient condition, although some of CO₂ molecules were released to the air, there were considerable CO₂ molecules remaining in the framework.

2.5 References

1. Furukawa, H.; Cordova, K. E.; O'Keeffe, M.; Yaghi, O. M. *Science* **2013**, *341*, 1230444.
2. Sumida, K.; Rogow, D. L.; Mason, J. A.; McDonald, T. M.; Bloch, E. D.; Herm, Z. R.; Bae, T. H.; Long, J. R. *Chem. Rev.* **2012**, *112*, 724-781.
3. He, Y.; Zhou, W.; Qian, G.; Chen, B. *Chem. Soc. Rev.* **2014**, *43*, 5657-5678.
4. Millange, F.; Walton, R. I. *Isr. J. Chem.* **2018**, *58*, 1019-1035.
5. Serra-Crespo, P.; Dikhtiarenko, A.; Stavitski, E.; Juan-Alcaniz, J.; Kapteijn, F.; Coudert, F. X.; Gascon, J. R. *Soc. Chem.* **2015**, *17*, 276-280.
6. Zhang, Y.; Lucier, B. E.; Huang, Y. *Phys. Chem. Chem. Phys.* **2016**, *18*, 8327-8341.
7. Millange, F.; Serre, C.; Ferey, G. *Chem. Commun.* **2002**, 822-823.
8. Christian Serre, F. M., Christelle Thouvenot. *J. Am. Chem. Soc.* **2002**, *124*, 13519-13526.

9. Loiseau, T.; Serre, C.; Huguenard, C.; Fink, G.; Taulelle, F.; Henry, M.; Bataille, T.; Ferey, G. *Chem. Eur. J.* **2004**, *10*, 1373-1382.
10. Liu, Y. *J. Am. Chem. Soc.* **2008**, *130*, 11813–11818
11. Volklinger, C.; Loiseau, T.; Guillou, N.; Ferey, G.; Elkaim, E.; Vimont, A. *Dalton Trans.* **2009**, 2241-2249.
12. Arstad, B.; Fjellvåg, H.; Kongshaug, K. O.; Swang, O.; Blom, R. *Adsorpt. Sci. Technol.* **2008**, *14*, 755-762.
13. Camacho, B. C. R.; Ribeiro, R. P. P. L.; Esteves, I. A. A. C.; Mota, J. P. B. *Sep. Purif. Technol.* **2015**, *141*, 150-159.
14. Rallapalli, P.; Prasanth, K. P.; Patil, D.; Somani, R. S.; Jasra, R. V.; Bajaj, H. *C. J. Porous Mater.* **2010**, *18*, 205-210.
15. Rallapalli, P.; Patil, D.; Prasanth, K. P.; Somani, R. S.; Jasra, R. V.; Bajaj, H. *C. J. Porous Mater.* **2009**, *17*, 523-528.
16. Mihaylov, M.; Chakarova, K.; Andonova, S.; Drenchev, N.; Ivanova, E.; Sabetghadam, A.; Seoane, B.; Gascon, J.; Kapteijn, F.; Hadjiivanov, K. *J. Phys. Chem. C* **2016**, *120*, 23584-23595.
17. Mihaylov, M.; Chakarova, K.; Andonova, S.; Drenchev, N.; Ivanova, E.; Pidko, E. A.; Sabetghadam, A.; Seoane, B.; Gascon, J.; Kapteijn, F.; Hadjiivanov, K. *Chem. Commun.* **2016**, *52*, 1494-1497.
18. Hu, Y.; Liu, Z.; Xu, J.; Huang, Y.; Song, Y. *J. Am. Chem. Soc.* **2013**, *135*, 9287-9290.
19. Hu, Y.; Lin, B.; He, P.; Li, Y.; Huang, Y.; Song, Y. *Chem. Eur. J.* **2015**, *21*, 18739-18748.
20. Jiang, S.; Hu, Y.; Chen, S.; Huang, Y.; Song, Y. *Chem. Eur. J.* **2018**, *24*, 19280-19288.
21. Lee, J. H.; Jeoung, S.; Chung, Y. G.; Moon, H. R. *Coord. Chem. Rev.* **2019**, *389*, 161-188.
22. Stavitski, E.; Pidko, E. A.; Couck, S.; Remy, T.; Hensen, E. J.; Weckhuysen, B. M.; Denayer, J.; Gascon, J.; Kapteijn, F. *Langmuir* **2011**, *27*, 3970-3976.

Chapter 3

3 Investigating the High-pressure Behaviors and CO₂-Framework Interactions of NH₂-MIL-53(Al) using *In Situ* Infrared Spectroscopy

3.1 Introduction

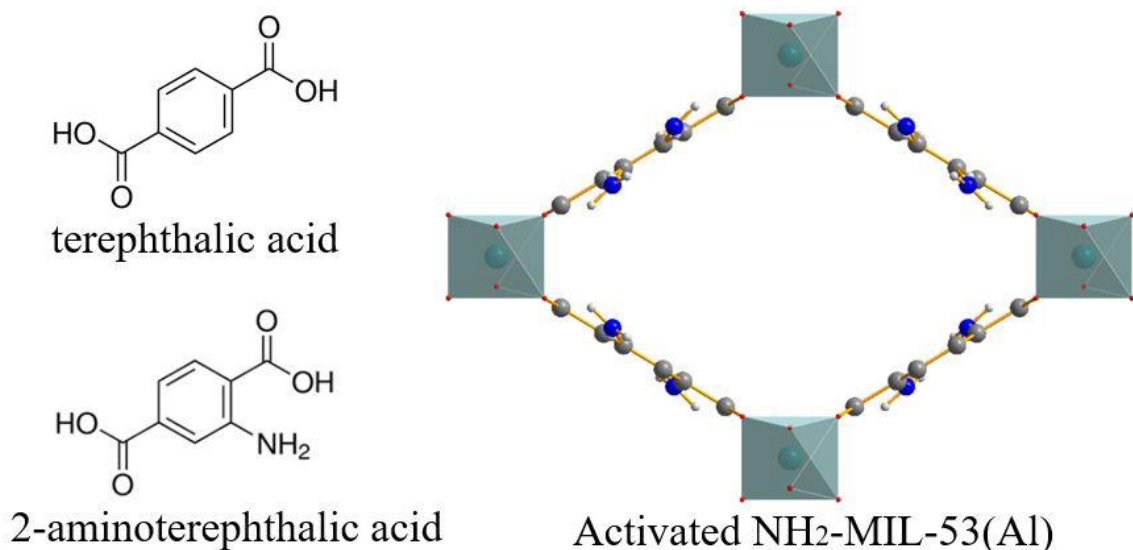


Figure 3.1 Structures of terephthalic acid, 2-aminoterephthalic acid and the topology of NH₂-MIL-53(Al) (Al = green, O = red, H = white, C = grey, N = blue).

Metal organic frameworks (MOFs) are crystalline materials comprised of metal centers joined by organic ligands through strong coordination bonds.¹ MOFs have been well-studied as one of the most promising adsorbents for CO₂ capture, owing to their porous structure and high surface area.² In general, MOFs with open metal sites are considered more suitable for gas adsorption, such as Mg-MOF-74. However, for MOFs without open metal sites, it has been demonstrated that CO₂ affinity of these MOFs can be improved efficiently by incorporating specific polar functional groups such as -OH, -NH₂, -COOH and so forth.³ For example, MIL-53 (MIL = Matériaux de l'Institut Lavoisier) family is one of the representative MOFs without open metal sites but

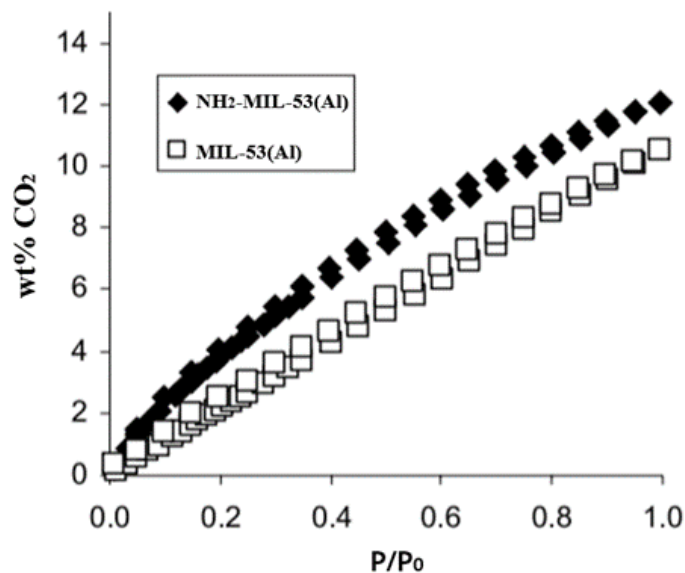


Figure 3.2 CO₂ adsorption and desorption isotherms of MIL-53(Al) and NH₂-MIL-53(Al) at 298 K ($P_0 = 1.0$ atm).⁴

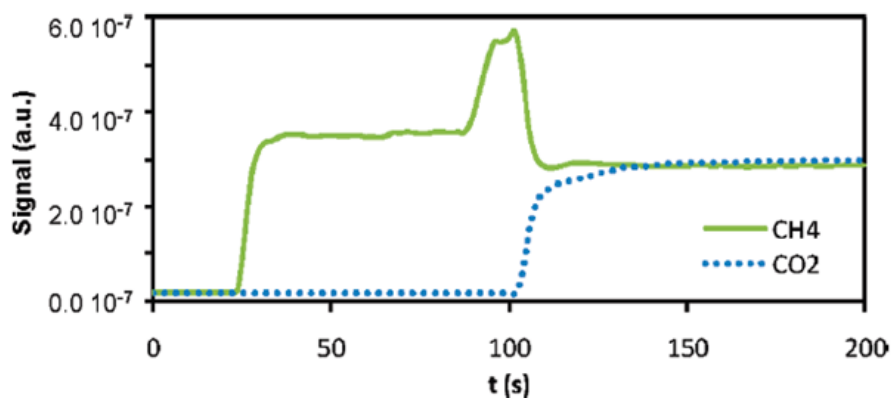


Figure 3.3 The CO₂/CH₄ separation performance of NH₂-MIL-53(Al) at 303 K and ambient pressure.⁵

featuring bridging OH groups in their framework, thus it exhibits excellent CO₂ adsorption capacity. To introduce -NH₂ functional groups in MIL-53, 2-aminoterephthalic acid was used as the organic linker instead of terephthalic acid. Figure 3.1 shows the structures of terephthalic acid and 2-aminoterephthalic acid, as well as the

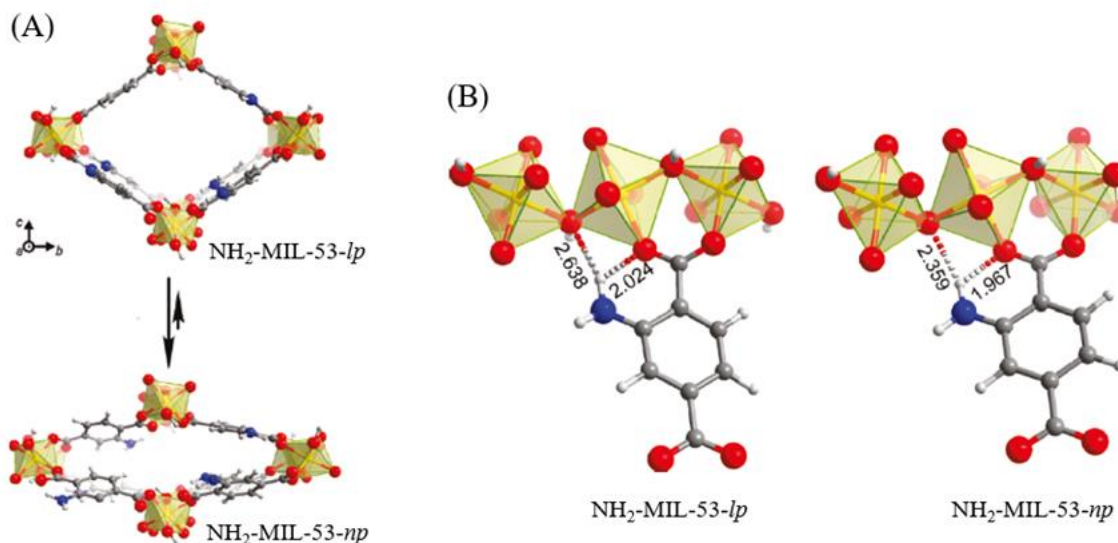


Figure 3.4 (A) The illustration of the large pore (*lp*) to narrow pore (*np*) phase transition of NH₂-MIL-53(Al); (B) The diagram of the intra-framework hydrogen bonds between amino groups and octahedral [AlO₆] (O = red, H = white, C = grey, N = dark blue, H-bond = dashed line).⁶

framework of NH₂-MIL-53. Figure 3.2 presents the comparison of CO₂ adsorption capacity of MIL-53(Al) and NH₂-MIL-53(Al). Specifically, at 1 atm and 298 K, MIL-53(Al) can adsorb 10 wt% of CO₂, whereas NH₂-MIL-53 adsorbed 12 wt% of CO₂. Although, the introducing of -NH₂ groups barely enhances the CO₂ affinity of MIL-53(Al),⁴ however, Couck *et al.* reported that -NH₂ groups increase selectively adsorption of CO₂ over N₂, H₂, and CH₄.⁵ As shown in Figure 3.3, equimolar CO₂/CH₄ was used to test the separation capacity of NH₂-MIL-53(Al). Because of the strong interactions between CO₂ and the framework, CO₂ adsorbs strongly in the open pores and gradually replaces weakly adsorbed CH₄ molecules. At atmospheric pressure and 303 K, one gram of NH₂-MIL-53(Al) can adsorb 0.83 mmol of CO₂, whereas no CH₄ is adsorbed. For most of amino-functionalized CO₂ sorbents, such an enhancement in CO₂ capture and separation is credited to the formation of hydrogen bonds between -NH₂ groups and CO₂. However, Stavitski *et al.* unveiled that -NH₂ groups only play an indirect role when it comes to CO₂ capture and separation capacity of NH₂-MIL-53(Al).⁶ They demonstrated that amino groups regulate the ‘breathing’ behavior of NH₂-MIL-53(Al), and thus

enhanced the performance CO₂ selective adsorption. As discussed in *Chapter 1.3*, activated MIL-53(Al) exhibits a remarkable flexibility by undergoing the large pore (*lp*) to narrow pore (*np*) phase transition in response to guest adsorption, pressure, or temperature, which is so-called ‘breathing effect’.⁷ However, in the case of the NH₂-MIL-53(Al), the formation of intermolecular hydrogen bonds between amino groups and octahedral [AlO₆] (Figure 3.4(B)) makes the *np* phase more favorable than *lp* (Figure 3.4(A)), and thus other gases (e.g., N₂, H₂, and CH₄) can hardly interact with the framework and are incapable of penetrating the initially *np*, while CO₂ interacts with the OH groups and even causes the *np* to *lp* transition at 13 bar and 30 °C.⁵

Apart from incorporating functional groups, another efficient method to improve adsorption performance of MOFs is the application of high pressures (e.g., in gigapascal range). Many high-pressure studies have demonstrated that pore sizes and shapes, even binding sites of MOFs can be fine-tuned, which eventually leads to better adsorption capacities.^{8,9,10,11,12} For example, pressure-enhanced CO₂ storage in MIL-68(In) has been revealed by Hu *et al* using FTIR spectroscopy. High pressures facilitate the CO₂-framework interactions, and thus enhance the CO₂ storage capacity of MIL-68(In).⁸ Moreover, activated NH₂-MIL-53(Al) exhibits a remarkable flexibility by undergoing the *lp* to *np* phase transition (Figure 3.4 (A)) under high pressures (~2 GPa) proved by PXRD.¹³

With this knowledge in mind, we applied high pressures in gigapascal level on NH₂-MIL-53(Al) to investigate the stability and phase transitions of activated NH₂-MIL-53(Al) using *in situ* infrared (IR) spectroscopy. Most importantly, even though there are no direct interactions between CO₂ and -NH₂ groups under near ambient pressures, it is expected that high-pressure could modify the framework and thus makes the direct interactions between CO₂ and -NH₂ groups possible. Therefore, compared to non-functionalized MIL-53(Al), there could be more interesting pressure-induced guest-host interactions in CO₂-loaded NH₂-MIL-53(Al).

3.2 Experimental section

3.2.1 MOF preparation

As described in the previous study, as-made $\text{NH}_2\text{-MIL-53(Al)}$ was synthesized under mild hydrothermal conditions using a 23 mL Teflon-lined stainless-steel autoclave.⁵ The starting chemicals were aluminum chloride hexahydrate (99%) and 2-amino terephthalic acid (98%), which were purchased from Sigma-Aldrich then used without purification. Aluminum chloride hexahydrate (1.28 g, 5.30 mmol) and 2-amino terephthalic acid (1.50 g, 8.30 mmol) were mixed in 20 mL of deionized water, followed by heating in an oven at 423 K for 3 days. The obtained mixture was filtered and washed with deionized water for 3 times.

To activate $\text{NH}_2\text{-MIL-53(Al)}$, we used solvent exchange method to remove the excess 2-amino terephthalic acid molecules. As-made $\text{NH}_2\text{-MIL-53(Al)}$ (0.5 g) was merged in 10 mL of *N, N*-dimethylformamide (DMF) in a 23 mL autoclave and then heated at 423 K overnight. The DMF exchange was carried out twice. Then the mixture was heating at 473 K under dynamic vacuum (≤ 1 mbar) for 8 h to remove DMF molecules inside the framework and then its topology and phase purity were verified with PXRD (Appendix B). Following the N_2 isotherm measurements for its surface area, the BET surface area of our sample is 895 m^2/g (960 m^2/g for activated $\text{NH}_2\text{-MIL-53(Al)}$ in the reference).

3.2.2 CO_2 loading

The same CO_2 loading procedures were used as described in *chapter 2.2.2*.

3.2.3 High-pressure apparatus

The same high-pressure equipment was employed as described in *chapter 2.2.3*.

3.3 Results and discussion

3.3.1 IR spectra of NH₂-MIL-53(Al) at ambient pressure

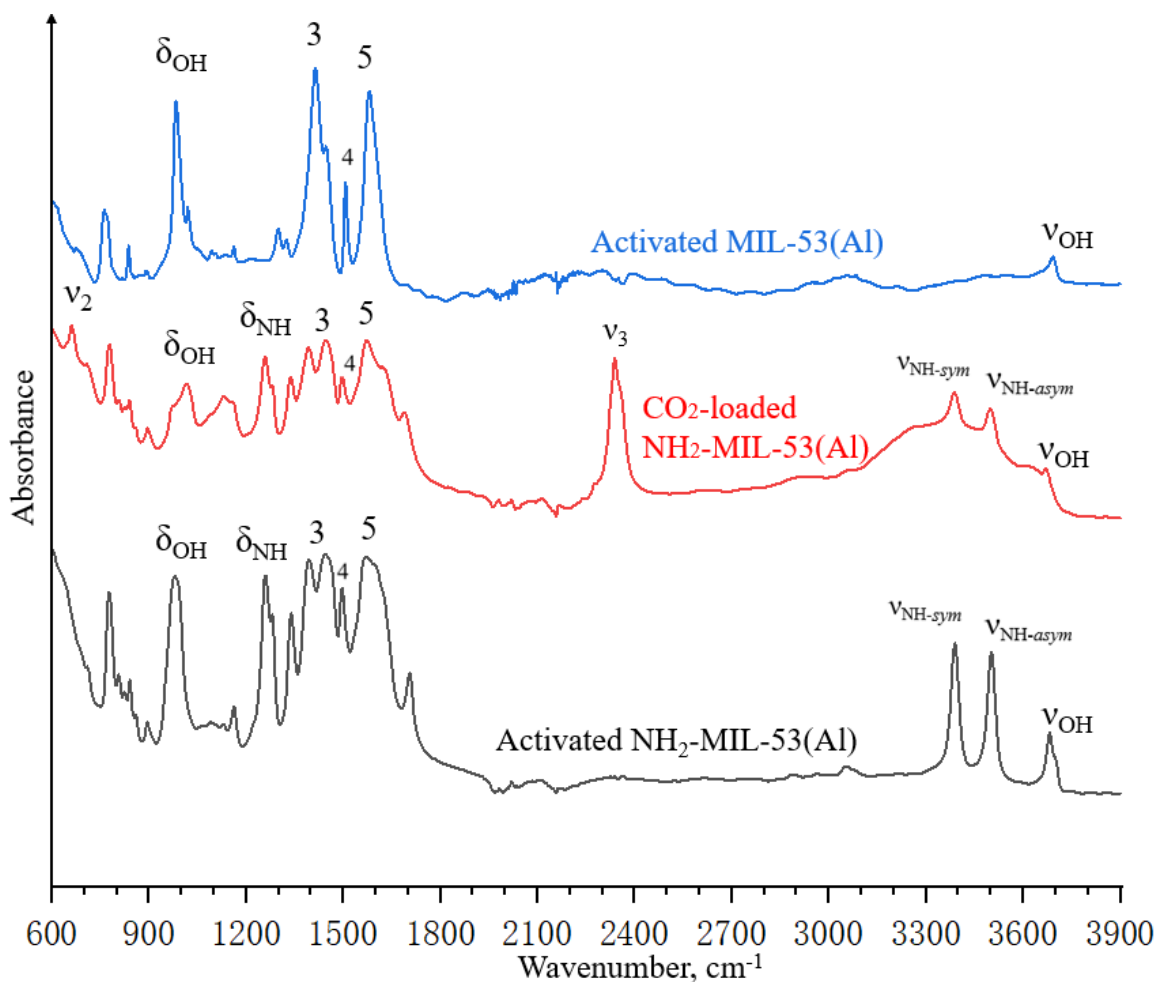


Figure 3.5 IR spectra of activated and CO₂-loaded NH₂-MIL-53(Al) as well as activated MIL-53(Al) at ambient pressure.

Figure 3.5 shows the IR spectra of NH₂-MIL-53(Al) and MIL-53(Al) at atmospheric pressure and room temperature. The spectra of NH₂-MIL-53(Al) samples highly agree with the previous studies and the majority of the peaks in the spectra are assigned and listed in Table 3.1^{4,14}. In addition, the activated amino-functionalized MIL-53(Al) is similar to the spectrum of non-functionalized MIL-53(Al) with additional bands characterizing the amino groups. In particular, the peak at 1260 cm⁻¹ (labelled as δ_{NH}) is

Table 3.1 Assignments for the majority IR modes of NH₂-MIL-53 spectra.

IR modes	Frequencies (cm ⁻¹)			Assignments
	Activated NH ₂ -MIL-53(Al)	CO ₂ -loaded NH ₂ -MIL-53(Al)	Ref 4, 14	
1	776	776	775	C-COO out-of-plane bending
δ_{OH}	980	1013	992	Al-OH-Al deformation modes
δ_{NH}	1258	1256	1257	-NH ₂ deformation modes
3	1394 - 1447	1393 - 1450	1392 - 1445	O-C-O symmetric stretching
4	1496	1500	1492	C-C ring vibrations
5	1573 - 1597	1573 - 1633	1577 - 1596	O-C-O asymmetric stretching
ν_{NH-sym}	3389	3389	3388	-NH ₂ symmetric stretching
$\nu_{NH-asym}$	3500	3497	3500	-NH ₂ asymmetric stretching
ν_{OH}	3681	3672	3701	O-H stretching
ν_2	-	661	661	CO ₂ bending
ν_3	-	2337	2337	CO ₂ asymmetric stretching

assigned as the deformation modes of -NH₂ groups. The other two peaks, at 3386 and 3500 cm⁻¹ (ν_{NH-sym} and $\nu_{NH-asym}$), are associated with the -NH₂ symmetric and asymmetric stretching, respectively. In addition, the modes at 980 and 3683 cm⁻¹ (δ_{OH} and ν_{OH}), are due to the bridging OH units, respectively, assigned as bending and stretching vibrations. Moreover, the peak 1 at 776 cm⁻¹ arises from the C-COO out-of-plane bending. Those bands in the region of 1394 - 1447 and 1573 - 1597 cm⁻¹ (peak 3 and 5) are due to the symmetric and asymmetric stretching of carboxylate groups, respectively, whereas the band in the middle (peak 4) is due to the C-C ring vibration. As for the profile of CO₂-loaded NH₂-MIL-53(Al), modes ν_2 (at 663 cm⁻¹) and ν_3 (at 2337cm⁻¹) are assigned to the CO₂ bending and asymmetric stretching, respectively, indicating the successful CO₂ loading.

3.3.2 High-pressure study of activated NH₂-MIL-53(Al)

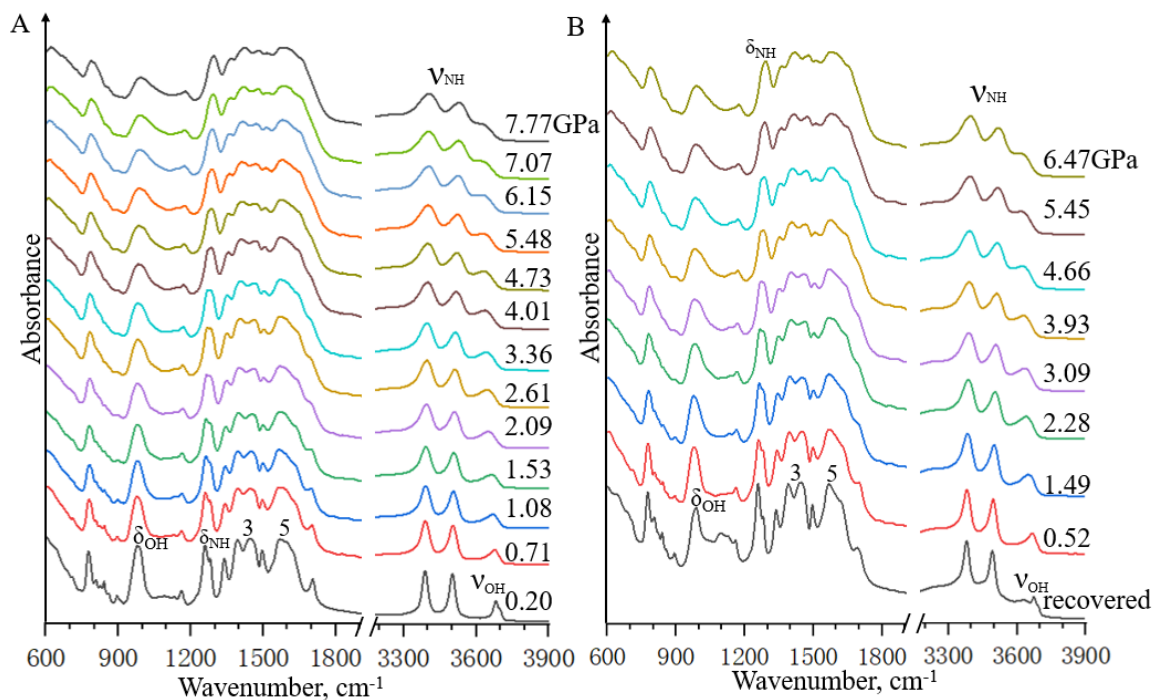


Figure 3.6 IR spectra of activated NH₂-MIL-53(Al) upon compression (A) and decompression (B).

In contrast to non-functionalized MIL-53(Al), Stavitski *et al.* demonstrated using FTIR spectroscopy that there are intra-framework hydrogen bonds between amino groups and octahedral [AlO₆] (Figure 3.4 (B)) in activated NH₂-MIL-53(Al).⁶ Specifically, they claimed that when hydrogen bonding only involving one of the two hydrogen atoms of -NH₂ groups, the degeneracy of the two N-H local oscillators is lifted. As a result, the splitting between the two N-H peaks is increased. Also, they carried out theoretical studies (atomistic density functional theory (DFT) simulations) of this MOF and demonstrated that the length of the hydrogen bonds (N-H···O) shortens because of the *lp* to *np* phase transition. We have also mentioned in *Chapter 1.3.2* that pressure-induced *lp* to *np* transition occurs at ~2 GPa in the case of NH₂-MIL-53(Al).¹³ Thus, it is of great interest to explore the high-pressure stability and intra-framework interactions of activated NH₂-MIL-53(Al). The IR spectra of activated NH₂-MIL-53(Al) presented in Figure 3.6 were recorded at room temperature upon compression from 0.20 to 7.77 GPa and then decompression to ambient pressure.

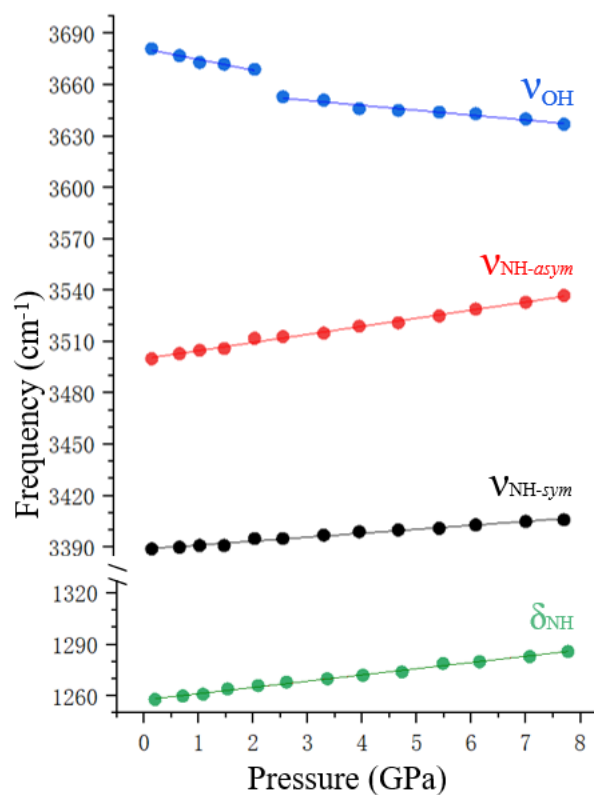


Figure 3.7 Frequency plots of selected IR modes of activated NH₂-MIL-53(Al) as a function of pressure.

Table 3.2 Pressure dependence (dv/dP, cm⁻¹/GPa) of selected IR modes of activated NH₂-MIL-53(Al).

Mode	Frequency (cm ⁻¹)	Pressure dependence (cm ⁻¹ /GPa)	
δ _{NH}	1258	3.6	
V _{NH-sym}	3389	2.3	
V _{NH-asy}	3500	4.7	
V _{OH}	3681	-6.26 (1 - 2.5 GPa)	-2.85 (2.5 - 8 GPa)

As presented in Figure 3.6 (A), with increasing pressure, all the bands broaden and then flatten gradually, indicating the pressure-induced amorphization of NH₂-MIL-

53(Al). Except the ν_{OH} mode, the rest of the bands exhibit the regular pressure-induced blue shifts, due to the stiffening of the bonds. In particular, the most noticeable changes of the IR bands upon compression are attributed to $-\text{NH}_2$ and OH groups, to be specific, bending and stretching modes of the $-\text{NH}_2$ groups (labelled as δ_{NH} and ν_{NH} , respectively) as well as O-H stretching (ν_{OH}). First of all, at 0.20 GPa, the frequencies of $\nu_{\text{NH-sym}}$ and $\nu_{\text{NH-asym}}$ modes match with previous studies about $\text{NH}_2\text{-MIL-53(Al)}$, indicating the existence of the above-mentioned hydrogen bonds between amino groups and octahedral $[\text{AlO}_6]$.⁶ Upon compression, although both $\nu_{\text{NH-sym}}$ and $\nu_{\text{NH-asym}}$ exhibit the pressure-induced blue shift, the splitting between the two ν_{NH} modes increase from 111 cm^{-1} (at 0.20 GPa) to 131 cm^{-1} (at 7.77 GPa), suggesting that high pressures enhance the hydrogen bonding interactions between $-\text{NH}_2$ groups and octahedral $[\text{AlO}_6]$. Figure 3.7 depicted the IR frequencies of these modes as a function of pressure, along their pressure dependence (dv/dP , $\text{cm}^{-1}/\text{GPa}$) listed in Table 3.2. Specifically, pressure dependences of $\nu_{\text{NH-sym}}$ and $\nu_{\text{NH-as}}$ modes are 2.3 and 4.7, which is consistent with the above discussion on the increased splitting of doublet ν_{NH} as well. Secondly, as discussed in *Chapter 2.3.3*, the stretching mode of OH group (ν_{OH}) exhibits a red shift upon hydrogen bonding.¹⁵ Given that there are no guest molecules inside the channels of the framework, the ν_{OH} mode red shifts greatly upon compression, suggesting the formation of intra-framework hydrogen bonds. Given the structural similarity between MIL-53(Al) and $\text{NH}_2\text{-MIL-53(Al)}$, it is reasonable to assume that the intra-framework hydrogen bonds regarding OH groups are formed in the same way as in the activated MIL-53(Al) , as depicted in Figure 3.8. With further compression, the ν_{OH} mode broadens and gradually flattens at highest pressure 7.77 GPa, indicating that high pressures enhance intra-framework interactions between OH groups and octahedral $[\text{AlO}_6]$. As for frequency plot of ν_{OH} , a great red shift occurs at ~ 2 GPa, along with the sudden change of its pressure dependence (from -6.26 to $-2.85\text{ cm}^{-1}/\text{GPa}$), which indicates that *np* phase is less compressibility and more stable.⁶

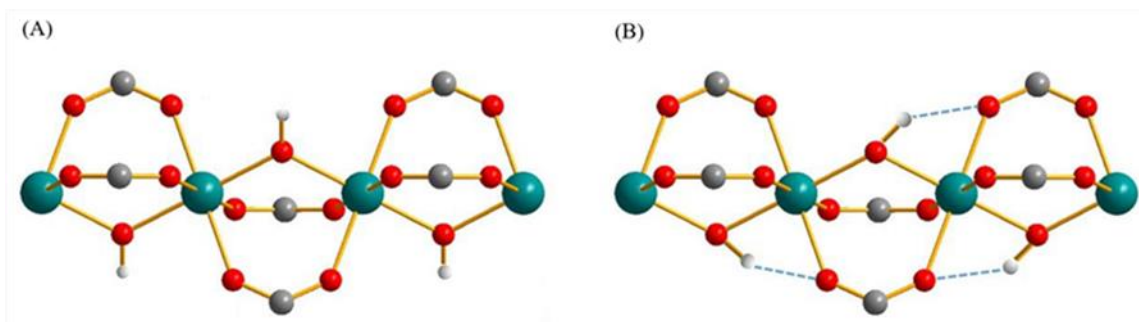


Figure 3.8 The comparison of the local structure of activated NH₂-MIL-53(Al) at ambient pressure (A) and at high pressure (B) with intra-framework H-bonds labelled as dashed lines (Al = dark green, O = red, H = white, C = grey).

Upon decompression, in Figure 3.6 (B), the recovered the spectrum at ambient conditions is almost identical to the initial profile at 0.20 GPa, suggesting that the pressure-induced amorphization of NH₂-MIL-53(Al) is reversible in the pressure region of 0 - 7.77 GPa, indicating the high stability of the activated NH₂-MIL-53(Al) framework.

3.3.3 High-pressure study of CO₂-loaded NH₂-MIL-53(Al)

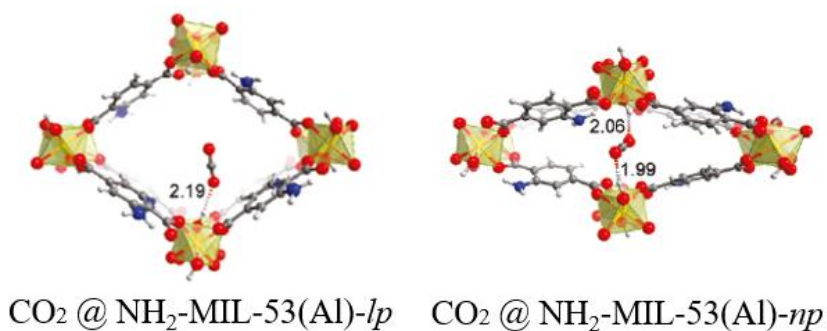


Figure 3.9 Optimized structures of NH₂-MIL-53(Al) with adsorbed CO₂ (O = red, H = white, C = grey, N = dark blue, hydrogen bond = dashed line).⁶

As discussed above, unlike other amino-functionalized CO₂ sorbents, there is no direct interaction between CO₂ molecules and the amino groups of NH₂-MIL-53(Al).⁶ Instead, the CO₂ binding sites of NH₂-MIL-53(Al) is the same as MIL-53(Al), that is,

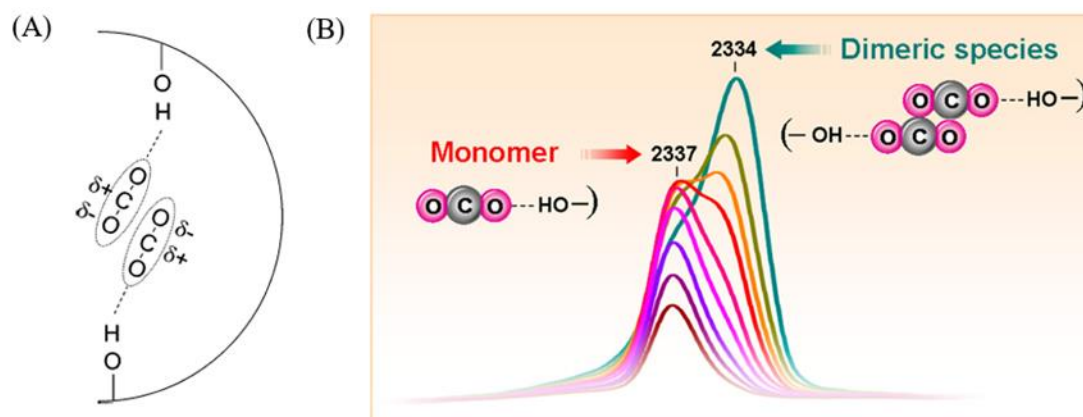


Figure 3.10 (A): Schematic diagram of dimeric CO₂ species located in the pores of MIL-53(Al); (B): An IR tool for differentiating between monomeric and dimeric CO₂ species in MOFs.¹⁶

adsorbed CO₂ molecules interact with the bridging OH groups inside the channels of the framework. Theoretical studies of its CO₂ binding sites were carried out and depicted in Figure 3.9.⁶ Specifically, there are two kinds of CO₂ adsorption forms co-existing under near ambient conditions: one is CO₂ adsorbed in large pore NH₂-MIL-53(Al) (CO₂@NH₂-MIL-53(Al)-*lp* or LP adsorption site). One intermolecular hydrogen bond is formed between one CO₂ molecule and the bridging OH unit. The second site is CO₂ adsorbed in narrow pore NH₂-MIL-53(Al) (CO₂@NH₂-MIL-53(Al)-*np* or NP adsorption site). One adsorbed CO₂ molecule interacts with two OH groups by forming two hydrogen bonds, causing the change in CO₂ adsorption orientation and the reduction of the bond lengths of the hydrogen bonds. It is the indirect and weak interactions between CO₂ and amino groups that makes MOF regeneration feasible readily under quite mild conditions.⁶ In addition, another study of CO₂ adsorption on NH₂-MIL-53(Al) has demonstrated via FTIR spectroscopy that CO₂ dimeric species ([CO₂]₂@NH₂-MIL-53(Al) or dimeric adsorption site) are formed and depicted in Figure 3.10 (A).¹⁶ More importantly, they proposed that a red-shift of the ν_3 (CO₂) frequency by 2–4 cm⁻¹ (Figure 3.10 (B)) can be used widely as an evidence for the existing of dimeric CO₂ species in MOFs. Thus, as one of the most promising CO₂ adsorbents, it is of great interest to elucidate its CO₂ adsorption behaviors under high pressures. In general, for *in situ* high-pressure study of CO₂ loaded MOFs, the amount of loaded CO₂ is barely controllable,

causing saturated CO₂ fundamental modes (especially ν_3). Therefore, CO₂ combination modes ($\nu_3 + 2\nu_2$) at $\sim 3600\text{ cm}^{-1}$ and ($\nu_3 + \nu_1$) at $\sim 3700\text{ cm}^{-1}$ have been used extensively as a powerful tool for analyzing CO₂-MOF interactions.^{8,10,11,12} For instance, CO₂-loaded ZIF-8 depicted in Figure 3.11, the $\nu_3 + \nu_1$ mode splits into two peaks when pressure > 0.6 GPa, suggesting that there are two types of CO₂: the lower-frequency component represents adsorbed CO₂ inside the framework, while the higher-frequency peak is attributed to the solid CO₂ outside the framework (see more details in *Chapter 2.3.4*).¹⁰

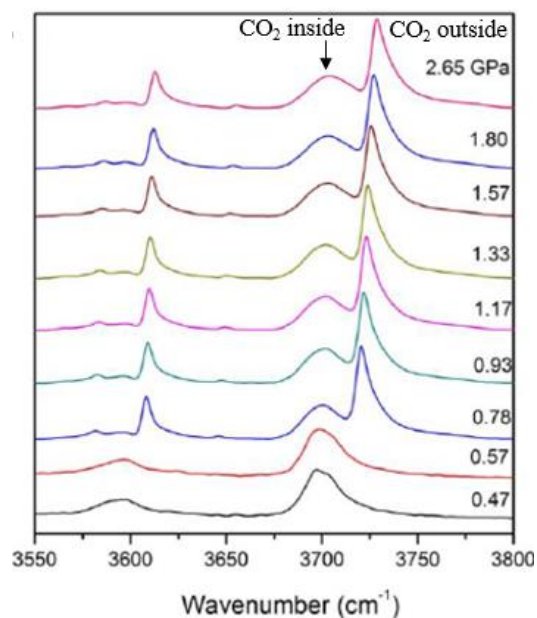


Figure 3.11 IR spectra of CO₂ loaded ZIF-8 upon compression in the spectral region of CO₂ combination modes.¹⁰

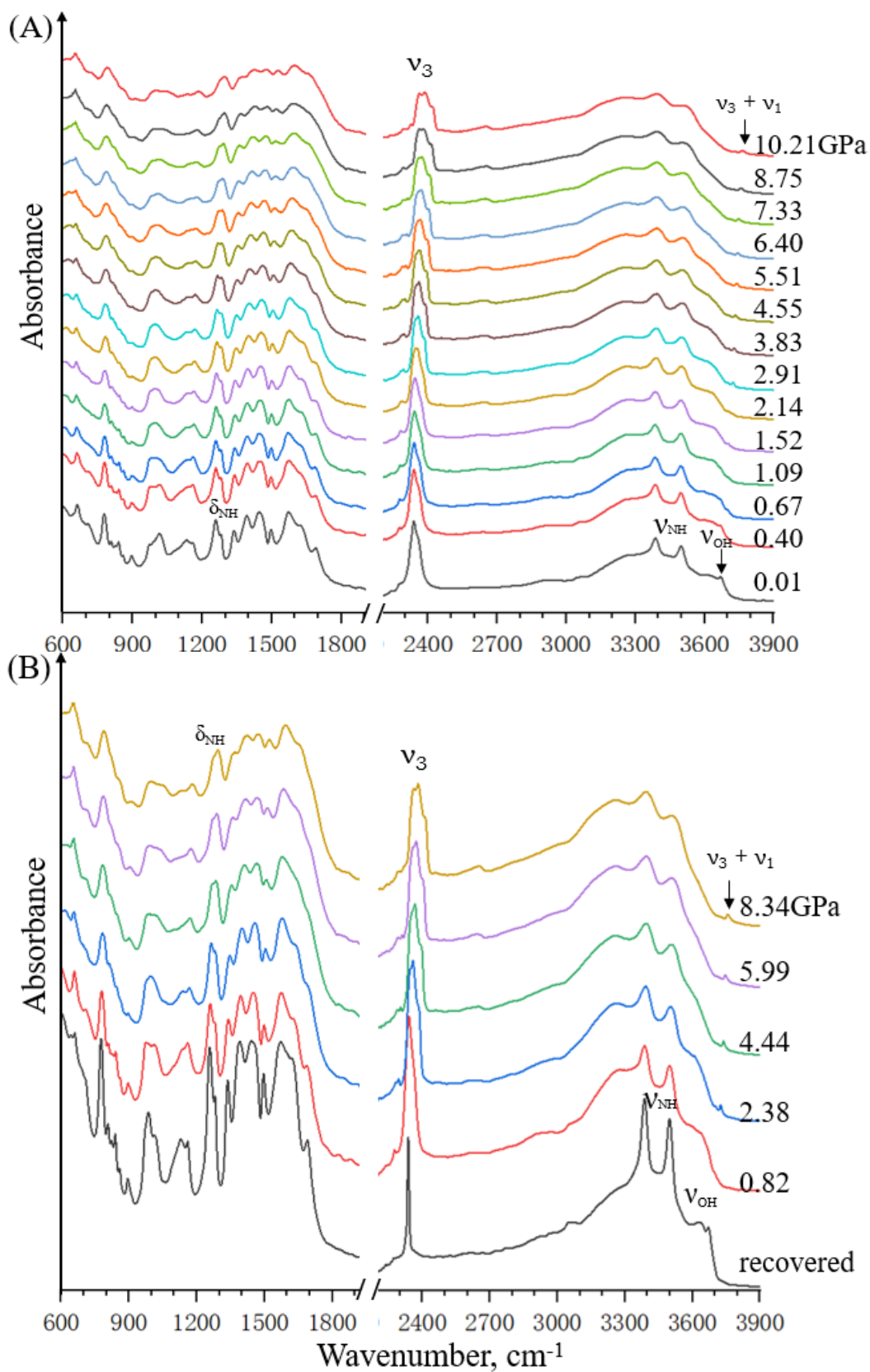


Figure 3.12 IR spectra of CO₂ loaded NH₂-MIL-53(Al) on compression (A) and decompression (B) at room temperature.

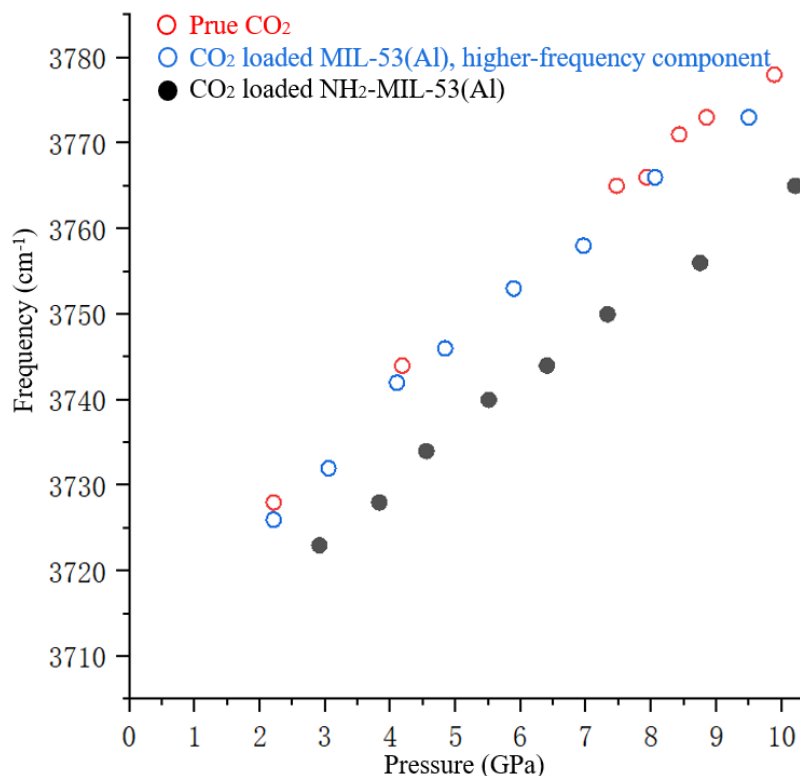


Figure 3.13 Frequency plots of $\nu_3 + \nu_1$ modes as a function of pressure.

Fortunately, in this case, the ν_3 mode on the IR spectra of CO₂ loaded NH₂-MIL-53(Al) is unsaturated and analyzable (Figure 3.12). For the first time, the CO₂-MOF interactions under extremely high pressures were studied using CO₂ fundamental modes along with CO₂ combination modes. We also noticed that, in Figure 3.12 (A), when pressures > 2.14 GPa, the CO₂ combination mode $\nu_3 + \nu_1$ shows as a single peak at ~3700 cm⁻¹ (at lower pressures, $\nu_3 + \nu_1$ must be buried in the broadened ν_{OH}). To verify which component this single peak represents, the frequency plots of $\nu_3 + \nu_1$ modes as a function of pressure depicted in Figure 3.13. In CO₂-loaded MIL-53(Al) system, all the higher-frequency component of $\nu_3 + \nu_1$ assigned to solid CO₂ outside the framework overlap with that of pure CO₂ in the pressure region of 2 - 10 GPa. Whereas in CO₂-loaded NH₂-MIL-53(Al) system, the $\nu_3 + \nu_1$ appears as a single peak at lower frequency, indicating that all CO₂ molecules absorb inside the channels. Under this circumstance, it is less complicated to study the high-pressure CO₂ adsorption of NH₂-MIL-53(Al) using CO₂ fundamental mode ν_3 .

According to the previous study, at ambient conditions, ν_3 of adsorbed CO_2 in $\text{NH}_2\text{-MIL-53(Al)}$ is at 2336.9 cm^{-1} . Also, ν_{OH} red shifts by -28 cm^{-1} to 3672 cm^{-1} compared with ν_{OH} of activated $\text{NH}_2\text{-MIL-53(Al)}$, because of the formation of the hydrogen bonds between the adsorbed CO_2 and OH groups.¹⁶ In Figure 3.12 (A), ν_3 is an asymmetric peak at 2337 cm^{-1} and ν_{OH} is a broad peak at 3672 cm^{-1} , which match with the literature, indicating the formation of hydrogen bonds between the adsorbed CO_2 and OH groups. Also, the ν_{OH} red shifts and broadens greatly with increasing pressure, suggesting the pressure-enhanced interactions between adsorbed CO_2 molecules and bridging OH groups.

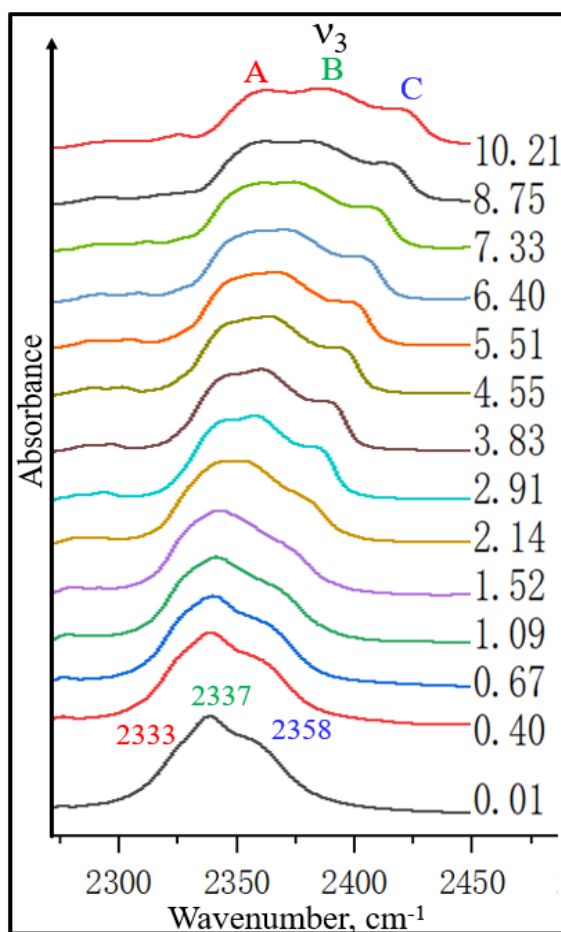


Figure 3.14 Enlarged ν_3 of CO_2 in $\text{NH}_2\text{-MIL-53(Al)}$.

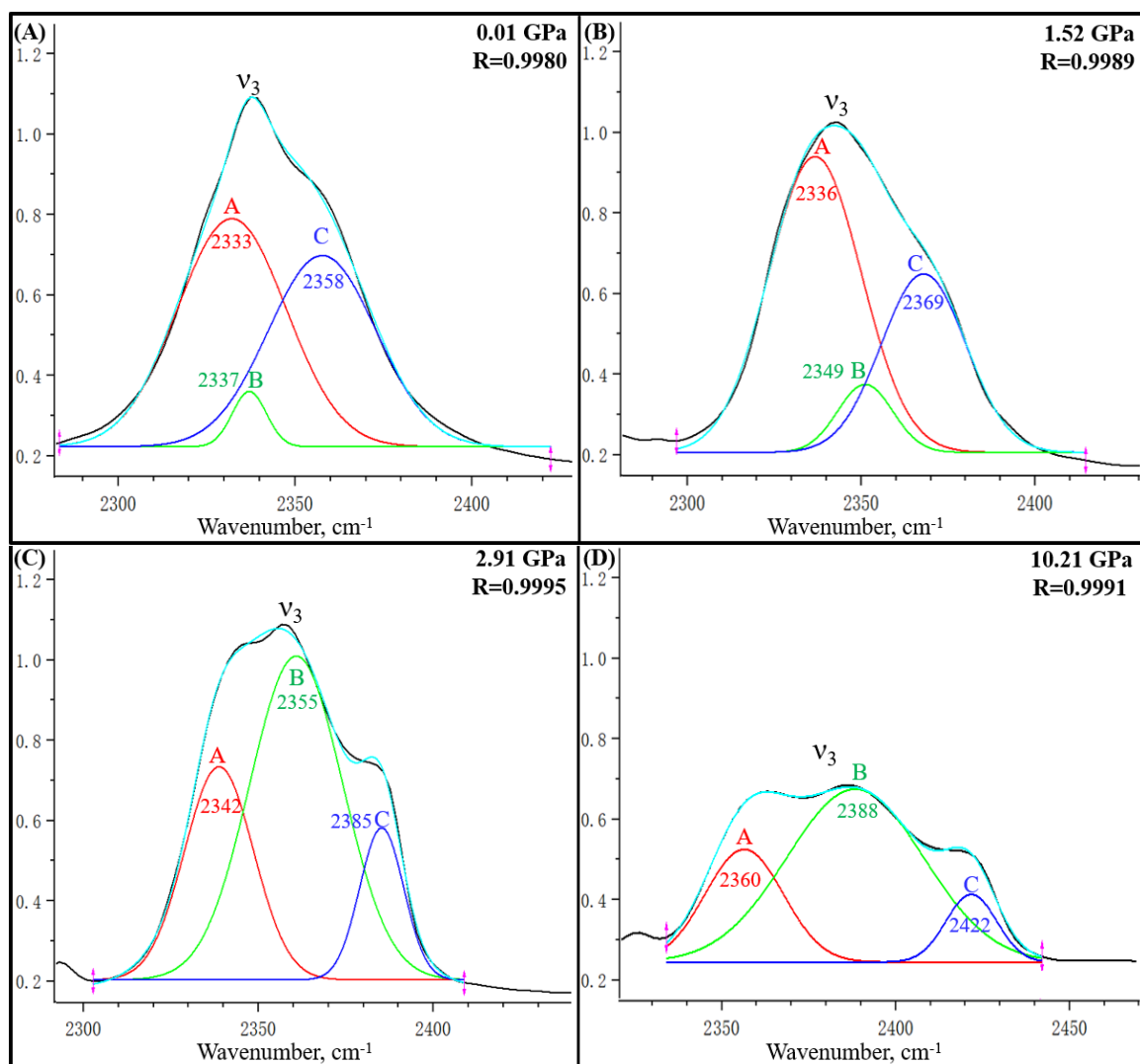


Figure 3.15 Deconvoluted v_3 at 0.01 GPa (A), 1.52 GPa (B), 2.91 GPa (C), and 10.21 GPa (D).

Table 3.3 Normalized peak area of CO_2 v_3 mode at various pressures in $\text{NH}_2\text{-MIL-53(AI)}$.

Pressure \ Mode	0.01 GPa	1.52 GPa	2.91 GPa	10.21 GPa
A	0.52	0.57	0.29	0.25
B	0.04	0.08	0.58	0.67
C	0.43	0.35	0.13	0.09

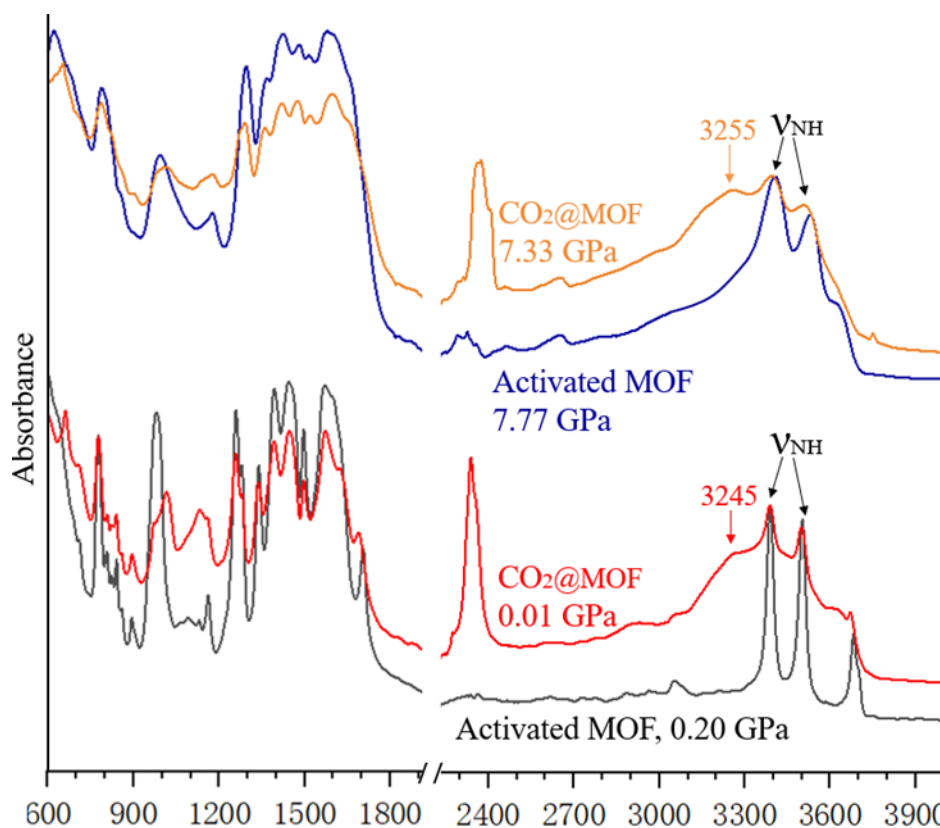


Figure 3.16 Comparisons of spectra of activated NH₂-MIL-53(Al) and CO₂ loaded NH₂-MIL-53(Al) under different pressures.

To assist with the analysis, Figure 3.14 presents the enlarged view of ν_3 of CO₂ loaded NH₂-MIL-53(Al), along with deconvoluted ν_3 at selected pressures (Figure 3.15). With increasing pressure, the asymmetric ν_3 at 0.01 GPa gradually splits into three peaks (labelled as A, B, C). According to previous studies, the LP adsorption is characterized by ν_3 of CO₂ at 2337 - 2338 cm⁻¹.⁶ Also, the dimeric CO₂ adsorption can be characterized by ν_3 at 2333 - 2335 cm⁻¹.¹⁵ At 0.01 GPa, ν_3 was deconvoluted as three peaks registered at 2333, 2337 and 2358 cm⁻¹ (Figure 3.15 (A)). Therefore, peak A represents CO₂ dimeric adsorption while peak B is due to CO₂ adsorbed in LP site (0 - 2 GPa). The reason why we assigned peak B as NP adsorption component in the pressure region of 3 - 10 GPa is that above-mentioned *lp* to *np* transition of NH₂-MIL-53(Al) occurs at ~2 GPa¹³ and the contribution of this transition is too little to influence the wavenumber of ν_3 .⁶ As for peak C, it appears at much higher wavenumber (2358 cm⁻¹) even at lowest pressure 0.01 GPa. Given that ν_3 is often observed < 2340 cm⁻¹ when CO₂ interacts with OH groups of

MOFs,¹⁶ peak C of CO₂ might be not associated with OH groups. With this information in mind, we also noticed that the symmetric and asymmetric ν_{NH} modes change dramatically upon CO₂ adsorption, as presented in Figure 3.16. According to previous studies under near ambient pressures, background IR spectra of NH₂-MIL-53(Al) are barely affected by CO₂ adsorption.^{6,16} In strong contrast, there is a broad peak at 3245 cm⁻¹ appearing along with greatly decreased intensities of ν_{NH} modes compared with activated NH₂-MIL-53(Al). Similar phenomenon was observed in previous studies regarding amino-functionalized materials other than MOFs.^{17,18} Specifically, when CO₂ absorbed on tetrabutylphosphonium amino acid [P(C₄)₄][AA], the doublet ν_{NH} mode disappears. Instead, a broad peak assigned to the perturbed N-H stretching appears at 3234 cm⁻¹ and a tiny peak attributed to CO₂⁻ species registers at 1662 cm⁻¹, which are believed as evidences for interactions between CO₂ molecules and -NH₂ groups.¹⁷ Unfortunately, they did not uncover whether there are some shifts occurring to ν_3 of adsorbed CO₂. Therefore, in our case, the rising of peak C in Figure 3.15 as well as the broad peak at ~3245 cm⁻¹ in Figure 3.16 can be rationalized by the assumption that direct interactions between CO₂ and -NH₂ groups of NH₂-MIL-53(Al) (amino adsorption) are observed under high pressures.

With these assignments proposed, when $P < 2.91$ GPa, there are three different CO₂ adsorption sites co-existing in NH₂-MIL-53(Al): dimeric adsorption (peak A), LP adsorption (peak B), and amino adsorption (peak C) sites (Figure 3.15 (A) and (B)). Table 3.4 lists the adsorption quantity of each CO₂ species under selected pressures, which is determined by peak area integration. At 0.01 GPa (Figure 3.15 (A)), dimeric adsorption and amino adsorption are dominant, accounting for 52% and 43% of the total adsorbed CO₂, respectively. Upon compression to 1.52 GPa, the quantities of adsorbed CO₂ in dimeric site and LP site increase slightly, while amino adsorption site is less favored (35%). Given the *lp* to *np* transition of the framework at ~2 GPa,¹³ when $P \geq 2.91$ GPa (Figure 3.15 (C) and (D)), there are no *lp* phase anymore. Thus, instead of LP adsorption, there are three different CO₂ adsorption sites co-existing in NH₂-MIL-53(Al): dimeric adsorption (peak A), NP adsorption (peak B), and amino adsorption (peak C) sites. At 2.91 GPa, dimeric species is halved while NP adsorption is highly favored (58%), which could be interpreted as that high pressures drive dimeric species apart and

then force each of them to interact with two OH groups. As a result, more CO₂ molecules are adsorbed in NP site (Figure 3.15 (C)). We thus conclude that the reduced pore volume of the *np* phase makes the dimeric adsorption less favorable. With pressure increased to 10.21 GPa (Figure 3.15 (D)), the quantities of CO₂ adsorbed in dimeric site (25%) and amino site (9%) continuously reduce, whereas NP adsorption site (67%) is further favored. Overall, upon compression, the interactions between CO₂ and amino groups are gradually weakened (from 43% to 9%), and the quantity of CO₂ dimeric species undergoes a slight increase ($P < 2.91$ GPa) and then decreases significantly from 57% to 25% ($P \geq 2.91$ GPa). In contrast, CO₂ adsorbed in NP site becomes a pronounced component at 2.91 GPa (58%). With further compression to 10.21 GPa, NP adsorption is even more favorable (67%).

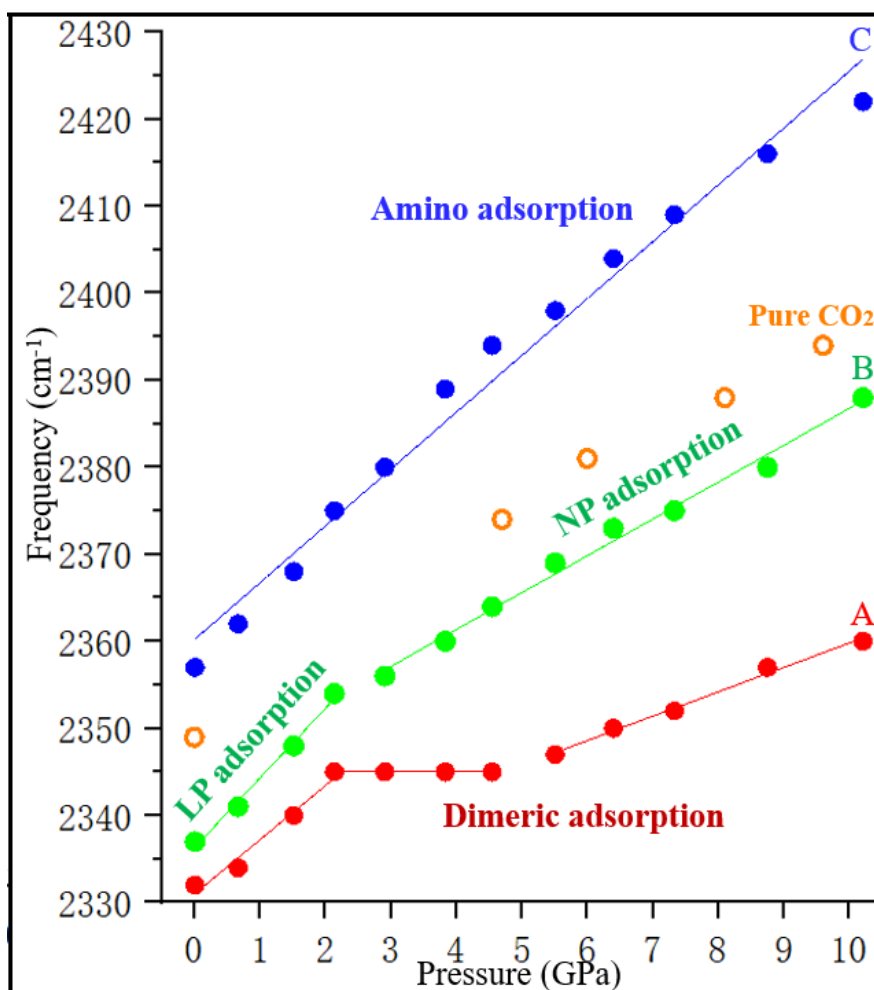


Figure 3.17 Frequency plots of ν_3 as a function of pressure.

Table 3.4 Pressure dependence (dv/dP , $\text{cm}^{-1}/\text{GPa}$) of ν_3 of CO_2 in $\text{NH}_2\text{-MIL-53(Al)}$.

Mode	Frequency (cm^{-1})	Pressure dependence ($\text{cm}^{-1}/\text{GPa}$)		
		0 - 2.5 GPa	2.5 - 10 GPa	
A	2333	6.2	2.5 - 4 GPa 0	5 - 10 GPa 2.3
B	2337	8.0	4.2	
C	2358	8.3	5.2	

To understand how the flexibility of the framework influences its CO_2 adsorption performance, frequency plots of deconvoluted ν_3 as a function of pressure are presented in Figure 3.17 with their pressure dependences (dv/dP , $\text{cm}^{-1}/\text{GPa}$) listed in Table 3.4.

Given the lp to np transition of the framework at ~ 2 GPa,¹³ it is expected that drastic changes are observed with increasing pressure from 1.52 GPa to 2.91 GPa. Specifically, from 0.01 to 2.14 GPa, peak A and B show significant blue shifts (pressure dependences 6 - 8 $\text{cm}^{-1}/\text{GPa}$). In contrast, when $P > 2.14$ GPa, pressure dependence of peak B is halved. That is because the np framework tends to exhibit less flexibility and compressibility than lp MOF. We also noticed that when pressures increased from 2.14 to 4.55 GPa, peak A (dimeric adsorption) does not exhibit any pressure-induced blue shift, suggesting that CO_2 dimeric species makes the np phase framework barely compressible in this pressure region. Overall, all three peaks exhibit pressure-induced blue shift upon compression, suggesting that the CO_2 bonds become stiffened.

At the highest pressure 10.21 GPa, all the bands significantly broaden (Figure 3.12 (A)), attributed to the pressure-induced amorphization. However, upon decompression (Figure 3.12 (B)), all bands are gradually recovered, suggesting its excellent framework stability. When all the applied pressures released, it is found that the pressure-regulated CO_2 adsorption behaviors of $\text{NH}_2\text{-MIL-53(Al)}$ are fully reversible in the entire pressure region (0 - 10 GPa). More importantly, although some of CO_2

molecules migrate out of the framework without applied pressures, evidenced by the suddenly dropped intensity of ν_3 in Figure 3.12 (B), there are quite a few CO₂ molecules remain inside the framework, since ν_3 remains at 2337 cm⁻¹ in the recovered spectrum.

3.4 Conclusion

In this chapter, we studied the high-pressure behaviors of activated and CO₂ loaded NH₂-MIL-53(Al) using *in situ* IR spectroscopy. Pressure-induced intra-framework hydrogen bonds between OH groups and octahedral [AlO₆] were formed in activated NH₂-MIL-53(Al). The pressure-induced modifications of activated NH₂-MIL-53(Al) were fully recovered upon complete decompression. We also demonstrated that the hydrogen bonding interaction between amino groups and octahedral [AlO₆] existing under ambient pressure was enhanced upon compression. As for CO₂ loaded NH₂-MIL-53(Al), at 0 - 2 GPa, there were three different adsorption sites co-existing: dimeric adsorption, LP adsorption, and amino adsorption, among which dimeric adsorption was dominated. At 2 - 10 GPa, there were three different CO₂ adsorption sites co-existing in NH₂-MIL-53(Al): dimeric adsorption, NP adsorption, and amino adsorption. CO₂ adsorbed in NP sites became a pronounced component at 2.91 GPa. We thus concluded that high pressures make the NP adsorption site highly favored over the other three. Moreover, when all the applied pressures released, pressure-regulated CO₂ adsorption behaviors of NH₂-MIL-53(Al) were found to be reversible in the entire pressure region (0 - 10 GPa). Even though there were CO₂ molecules migrating out of the framework upon complete decompression, quite a few CO₂ molecules remain inside the framework within LP adsorption site.

3.5 References

1. Furukawa, H.; Cordova, K. E.; O'Keeffe, M.; Yaghi, O. M. *Science* **2013**, *341*, 1230444.
2. Sumida, K.; Rogow, D. L.; Mason, J. A.; McDonald, T. M.; Bloch, E. D.; Herm, Z. R.; Bae, T. H.; Long, J. R. *Chem. Rev.* **2012**, *112*, 724-781.
3. Torrisi, A.; Bell, R. G.; Mellot-Draznieks, C. *Cryst. Growth Des.* **2010**, *10*, 2839-2841.

4. Arstad, B.; Fjellvåg, H.; Kongshaug, K. O.; Swang, O.; Blom, R. *Adsorpt. Sci. Technol.* **2008**, *14*, 755-762.
5. Couck, S. *J. Am. Chem. Soc.* **2009**, *131*, 6326–6327.
6. Stavitski, E.; Pidko, E. A.; Couck, S.; Remy, T.; Hensen, E. J.; Weckhuysen, B. M.; Denayer, J.; Gascon, J.; Kapteijn, F. *Langmuir* **2011**, *27*, 3970-3976.
7. Loiseau, T.; Serre, C.; Huguenard, C.; Fink, G.; Taulelle, F.; Henry, M.; Bataille, T.; Ferey, G. *Chem. Eur. J.* **2004**, *10*, 1373-1382.
8. Hu, Y.; Lin, B.; He, P.; Li, Y.; Huang, Y.; Song, Y. *Chem. Eur. J.* **2015**, *21*, 18739-18748.
9. Hu, Y.; Kazemian, H.; Rohani, S.; Huang, Y.; Song, Y. *Chem. Commun.* **2011**, *47*, 12694-12696.
10. Hu, Y.; Liu, Z.; Xu, J.; Huang, Y.; Song, Y. *J. Am. Chem. Soc.* **2013**, *135*, 9287-9290.
11. Jiang, S.; Hu, Y.; Chen, S.; Huang, Y.; Song, Y. *Chem. Eur. J.* **2018**, *24*, 19280-19288.
12. Mao, H.; Xu, J.; Hu, Y.; Huang, Y.; Song, Y. *J. Mater. Chem. A* **2015**, *3*, 11976-11984.
13. Serra-Crespo, P.; Dikhtiarenko, A.; Stavitski, E.; Juan-Alcaniz, J.; Kapteijn, F.; Coudert, F. X.; Gascon, J. *R. Soc. Chem.* **2015**, *17*, 276-280.
14. Mihaylov, M.; Andonova, S.; Chakarova, K.; Vimont, A.; Ivanova, E.; Drenchev, N.; Hadjiivanov, K. *Phys. Chem. Chem. Phys.* **2015**, *17*, 24304-24314.
15. Mihaylov, M.; Chakarova, K.; Andonova, S.; Drenchev, N.; Ivanova, E.; Pidko, E. A.; Sabetghadam, A.; Seoane, B.; Gascon, J.; Kapteijn, F.; Hadjiivanov, K. *Chem. Commun.* **2016**, *52*, 1494-1497.
16. Mihaylov, M.; Chakarova, K.; Andonova, S.; Drenchev, N.; Ivanova, E.; Sabetghadam, A.; Seoane, B.; Gascon, J.; Kapteijn, F.; Hadjiivanov, K. *J. Phys. Chem. C* **2016**, *120*, 23584-23595.
17. Zhang, J.; Zhang, S.; Dong, K.; Zhang, Y.; Shen, Y.; Lv, X. *Chem. Eur. J.* **2006**, *12*, 4021-4026.
18. Rocchia, M.; Garrone, E.; Geobaldo, F.; Boarino, L.; Sailor, M. J. *Phys. Status Solidi A* **2003**, *197*, 365-369.

Chapter 4

4 Summary and Future Work

4.1 Summary

Owing to their porous structures and outstanding tunability, MOFs have been widely investigated as one of the most promising CO₂ absorbents. In this thesis, we used high-pressure *in situ* IR spectroscopy to study the structural stabilities as well as the CO₂ adsorption behaviors of two well-known and flexible MOF systems: MIL-53(Al) and NH₂-MIL-53(Al). Because of their flexible wine-rack structures, both MOFs showed remarkable stability under high pressures up to 10 GPa. In activated MIL-53(Al) and activated NH₂-MIL-53(Al), pressure-induced intra-framework hydrogen bonding interactions were observed. Pressure-enhanced CO₂ adsorption was demonstrated in CO₂-loaded MIL-53(Al). Additional CO₂ adsorption sites were observed in CO₂-loaded NH₂-MIL-53(Al). Overall, pressure exerted a crucial influence on the intra-framework as well as CO₂-framework interactions.

In *Chapter 2*, the high-pressure studies of as-made, activated and CO₂-loaded MIL-53(Al) were carried out. For as-made MIL-53(Al), pressures-induced inter-framework hydrogen bonds between the OH groups of the framework and free H₂BDC molecules were observed. Activated MIL-53(Al) exhibited extraordinary stability compared to as-made and CO₂-loaded MIL-53(Al), attributed to its empty wine-rack channels. Also, pressure-induced intra-framework interactions via hydrogen bonding between OH groups and octahedral [AlO₆] were enhanced upon compression. In addition, structural modifications of both as-made and activated MIL-53(Al) were irreversible upon complete decompression, because the OH groups remained involved in hydrogen bonding. Finally, for CO₂-loaded MIL-53(Al), pressure-enhanced CO₂ adsorption was observed. When the pressure recovering to ambient condition, although some of the CO₂ molecules were released to the air, there were considerable CO₂ molecules remaining in the framework.

In *Chapter 3*, we studied the high-pressure behaviors of activated and CO₂ loaded NH₂-MIL-53(Al) comparatively. The excellent high-pressure stabilities of activated NH₂-MIL-53(Al) was verified, since its framework was fully recovered from pressure-induced structural modifications in the entire pressure region of 0 - 10 GPa. We also demonstrated that, apart from the known intra-framework hydrogen bonding interactions between NH₂ groups and octahedral [AlO₆], there was pressure-induced intra-framework hydrogen bonds between OH groups and octahedral [AlO₆]. For CO₂ loaded NH₂-MIL-53(Al), CO₂ fundamental vibration mode (ν_3) and CO₂ combination mode ($\nu_3 + \nu_1$) were used to investigate the CO₂-framework interactions and CO₂ adsorption sites under high pressures. Upon compression, pressure-induced dimeric CO₂ species was formed and direct interaction between CO₂ and amino group was observed. Specifically, there were four different high-pressure CO₂-framework interactions: between one dimeric CO₂ species and two bridging OH groups (dimeric adsorption); between one CO₂ molecule and one bridging OH group (LP adsorption); between one CO₂ molecule and two bridging OH groups (NP adsorption); between CO₂ molecule and -NH₂ group (amino adsorption). At 0 - 2 GPa, dimeric adsorption was the primary site. While at 2 - 10 GPa, because of the *lp* to *np* transition, CO₂ adsorbed in NP sites became a pronounced component. Therefore, high pressures made the NP adsorption site highly favored over the other three. Finally, upon complete decompression, pressure-regulated CO₂ adsorption behaviors of NH₂-MIL-53(Al) were found to be fully reversible. There were CO₂ molecules migrating out of the framework without applied pressures. However, quite a few CO₂ remained inside the framework within LP adsorption site.

As for the comparison between MIL-53(Al) and NH₂-MIL-53(Al), previous studies have demonstrated that they feature the same wine-rack structure and CO₂ adsorption sites under ambient conditions. Upon compression, we noticed that the flexible structures of both activated systems facilitated the formations of the intra-framework interactions between OH groups and octahedral [AlO₆]. While pressures enhanced the CO₂-framework interactions in both CO₂-loaded systems, additional CO₂ adsorption site around the amino group was observed upon compression only in CO₂ loaded NH₂-MIL-53(Al).

We hope that this thesis could provide more insight into how the high pressures influence the structural stabilities and CO₂ adsorption capacities of MIL-53 family. With this knowledge, MOFs could also be developed into desirable CO₂ adsorbents with larger CO₂ storage capacity.

4.2 Future work suggestions

With this understanding of pressure effects on MIL-53 family in mind, further experiments should help answer some unresolved questions in this thesis.

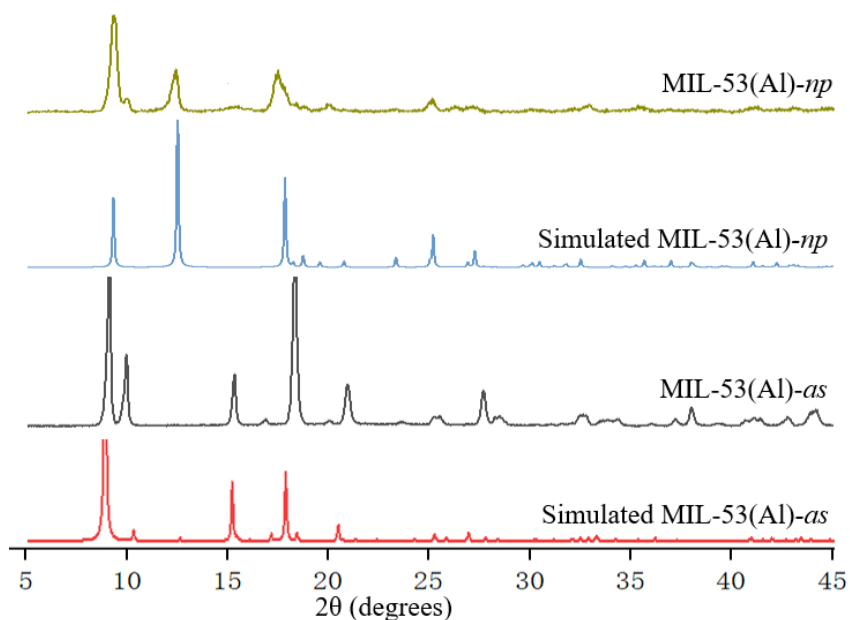
First of all, *in situ* high-pressure XRD via synchrotron radiation (SR) would be a supplemental measurement to study the changes of bonds length of the activated frameworks upon compression, so as to shed more light on the pressure-induced intra-framework hydrogen bonds between OH groups and [AlO₆].

Secondly, computational simulations would be useful to study the high-pressure CO₂ adsorption sites in NH₂-MIL-53(Al), so as to compare with the experimental work presented in *Chapter 3*.

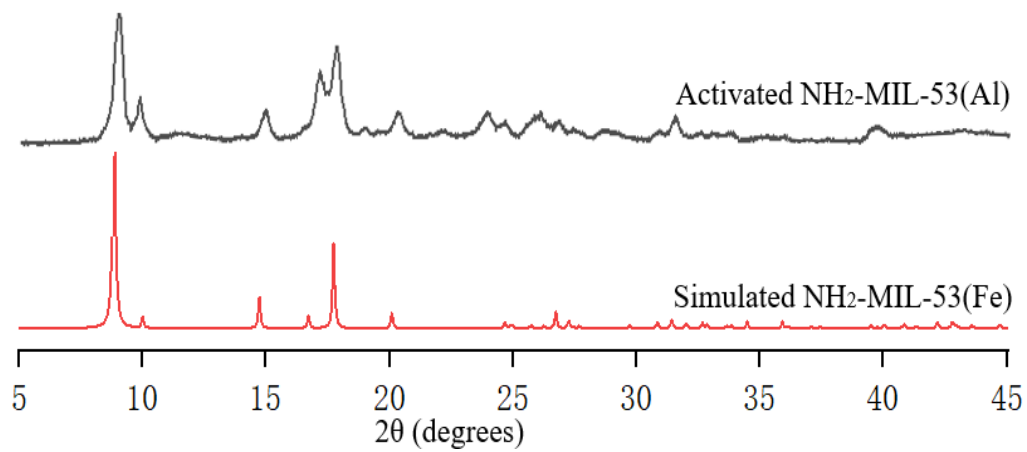
Thirdly, given that MIL-53 family undergoes a reversible *lp* - *np* transition under high temperatures, *in situ* high-pressure study of activated MIL-53 systems can be carried out under high temperatures to compare the sensitivity of the activated and CO₂-loaded frameworks towards high-temperature and high-pressure. If the high temperature opens the narrow pore even under high pressures (> 2 GPa), then CO₂-loaded frameworks could exhibit a higher CO₂ adsorption capacity under high pressure and high temperature.

Appendices

Powder X-ray diffraction (PXRD) experiments were carried out to verify the MOF structure and phase purity. In our local lab, an Inel CPS powder diffractometer operating with Cu K α radiation ($\lambda = 1.5406 \text{ \AA}$) was used to record the PXRD patterns. Reflections were collected at 2θ values ranging from 5 to 120° with a total acquisition time of approximately five minutes for each sample. The PXRD patterns are presented below. Our samples are in good agreement compared with literatures.^{1,2}



Appendix A: The PXRD patterns of MIL-53(Al)-as, MIL-53(Al)-np, as well as simulated MIL-53(Al)-as and MIL-53(Al)-np.



Appendix B: The PXRD patterns of activated NH₂-MIL-53(Al) and simulated NH₂-MIL-53(Fe).

Curriculum Vitae

Name: Boqing Li

Post-secondary Education and Degrees: Hubei University
Wuhan, Hubei, China
2013 - 2017 B.E

The University of Western Ontario
London, Ontario, Canada
2018 - 2020 M.S. candidate

Honors and Awards: International Graduate Tuition Scholarship
2018 - 2020
Outstanding Student Scholarship
2013 - 2017

Related Work Experience

Teaching Assistant
The University of Western Ontario
2018 - 2020

Research Assistant
The University of Western Ontario
2018 - 2020